MASTER OF SCIENCE THESIS

Low Reynolds number Performance of contra-rotating Coaxial Rotors
Evaluated for use by Unmanned Aerial Vehicles

M. H. Hogeweg B.Sc.

June 13, 2017

Faculty of Aerospace Engineering · Delft University of Technology

ŤU**Delft**
Delft
University of
Technology

Challenge the future

Low Reynolds number Performance of contra-rotating Coaxial Rotors
Evaluated for use by Unmanned Aerial Vehicles

MASTER OF SCIENCE THESIS

For obtaining the degree of Master of Science in Aerospace Engineering at Delft University of Technology

M. H. Hogeweg B.Sc.

June 13, 2017

Faculty of Aerospace Engineering · Delft University of Technology

TUDelft Delft
University of
Technology

The undersigned hereby certify that they have read and recommend to the Faculty of Aerospace Engineering for acceptance a thesis entitled **"Low Reynolds number Performance of contra-rotating Coaxial Rotors"** by **M. H. Hogeweg B.Sc.** with number **137#17#MT#FPP** in partial fulfillment of the requirements for the degree of **Master of Science**.

Dated: <u>June 13, 2017</u>

Chairman:

Ir. J. A. Melkert

Supervisor:

Dr. ir. M. Voskuijl

Reader:

Dr. ir. G. N. Saunders-Smits

Acknowledgements

This report forms the completion of my MSc study at the faculty Aerospace Engineering of Delft University of Technology. The report presented here is an investigation into the design of a small coaxial rotorcraft. A numerical simulation model has been developed in order to assess this.

At the start of this report I would like to thank some people who helped and supported me in completing this work. First of all I would like to express my gratitude to the exam committee. Special thanks goes to John Stoop for providing an always listing ear and never doubting the successful conclusion of this project. I also would like to thank Marilena Bos-Pavel who always made time to support me and for the reference model to check the results with.

I would like to thank my friends for support in my graduation period. Always ready to listen to my endless asking to listen to my ideas to solve the problems that were present. Finally, I would like to thank my parents, especially my mother, who supported me during my whole study. Whenever I needed positive energy in order to continue and finish my study, I could come to her to find positive encouragement.

Delft, The Netherlands
June 13, 2017

M. H. Hogeweg B.Sc.

Summary

The coaxial rotor configuration is not used much as an Unmanned Air Vehicle (UAV). This is even more the case when looking at the use in combination with variable pitch rotors. Even though the design is robust and at a larger scale also applied in helicopter designs. The main reason for this is the complexity of the design.

A generic model to design and analyse a coaxial rotorcraft was searched for in literature. With the fact of not having found such a model this search ended. The models that were found were made for specific rotorcraft, using custom data to make the model. This is why a generic coaxial model should be developed to look at the behaviour of small coaxial rotorcraft. A generic model gives the ability to integrate different methods to evaluate the aerodynamics into the model. In this way the effects of for example the Reynolds number can be incorporated.

For this purpose the choice was made to develop a modular numerical Blade Element Model (BEM). The main features are the use of numerical integration methods to calculate the forces and the use of a look-up table for the aerodynamic assessment of lift and drag. To be able to use the model for the UAV the look-up tables need to use data applicable for low Reynolds number flows. The model is evaluated using reference data provided by an analytical model. For the full-scale rotorcraft this reference is the Kamov 32A and for the small scale the references are the Guardian Angel unmanned aerial vehicle and the Walkera Lama 400. The final goal is to have a Blade Element Momentum Theory model, which is faster than a Computational Fluid Dynamics or Finite Volume Method code, while also being more accurate with more details than an analytical model. In this way the flight performance of a small Unmanned Aerial Vehicle can be assessed with the right level of fidelity.

The new model required a number of parts of the coaxial rotorcraft to be modelled using 'new' methods. The first is to implement a numerical integration method to solve for the rotor forces. This is combined with the use of a look-up table for the quasi-steady 2D aerodynamics of the rotorblades. Also, the wake influence of the upper rotor on the lower rotor is changed. The new methods are the analytical wake contraction ratio as described by Landgrebe. This is combined with a numerical implementation of the wake influence as described by Castles attenuation method. The remaining parts are taken from the reference model, which is an analytical Blade Element Method model made by Campfens (2008). These parts are the description of the flapping motion of the rotorblades, the description of the body forces as well as the modelling of the equations of motion. All these parts are linked together to form a generic modular model.

To get to the performance calculations the trim situation for the rotorcraft has to be calculated. For this purpose the Newton Iteration method was used to obtain the trim situation for the model using the input data for a full-scale Kamov-32. The results indicate the successful implementation of the modular model. Also, the new model, using numerical methods for the rotor and wake influence calculations, shows the same trend in the required control inputs as the reference model. The actual values are, however,

different. For example, the collective control input for the lower rotor is higher than for the upper rotor. In the reference model it is the other way around. This reversal is caused by the requirement to have torque equilibrium on both rotors. The generated torque at the lower rotor is lower than at the upper rotor for the same generated lift. This means that the lower rotor requires more collective input to balance the torque of the upper rotor.

A number of observations can be made from the trim curve calculations for the Kamov-32. The conclusion is that the new model behaves as expected. The collective and cyclic control inputs to maintain a trimmed flight condition are of the same magnitude as those in the reference model. Also, the shape of the trend with increasing forward velocity is the same for both models. Additional the new model provides an insight in the local flow conditions and force distributions at the rotorblades.

The trim solution for the Guardian Angel and the Walkera Lama 400 could not be found using the Newton Iteration method. To find a suitable solution and get some insight in the reason for the Newton Iteration method to fail, a 'sweep' calculation was performed. This sweep calculation consists of variating the control inputs and logging the corresponding forces in a coherent way such that it spans the control space (between minimum and maximum). For example, the collective control angles of the upper and lower rotors are changed from the minimum angle to the maximum angle such that all combinations are calculated. Then, comparing the resultant vertical force, difference between thrust and weight, to the control inputs a curve can be found linking the controls to an equilibrium state. This process is then repeated for the resultant torque. The equilibrium solution is then the location where both the resultant force as the torque are zero. This process can then be repeated for the cyclic control angle, the induced velocity and the body orientation angles. The result from the Sweep calculations was that the trim failure was caused by lacking a solution for the cyclic control angles. The resultant pitch and roll moments didn't show a logical trend with respect to the control inputs. A number of methods were found, such that a trimmed flight solution can be found. The first method is to apply a limit for the mass properties of the rotorblades. Especially when the moment of inertia is too small the trim situation cannot be found. The main problem with this solution is that the Guardian Angel is too small to be calculated using this limit. This was verified by testing the Walkera Lama, which is larger. The second method to solve this problem is to use a finer calculation grid for the rotor disk. In other words, use more steps in radial and rotational direction. The main disadvantage from this solution is the increase in calculation time. Both of these solutions are indicative for numerical limitations in the application of the model.

The result for the Guardian Angel is a rather flat collective control change with forward velocity. This is most likely caused by the high rotational velocity. In this way reducing the effects of the forward speed on the generated lift. The trim curve for the Walkera Lama 400 shows the familiar bucket shape as seen for the Ka-32. It is also easier to obtain than for the Guardian Angel. Unfortunately the time required to obtain the trim results for the MAVs is still larger than the intended goal. This can be attributed to the required discritization to get to these results. Using the sweep calculation method approximately 400 calculations per iteration are required. This takes about four to five minutes to calculate. For a complete trim curve with on average ten steps the required calculation time adds up to about five hours, while the intended goal was in the order of

15 minutes.

The final result is that the new model, works as expected when taking the numerical limits into account. These limits require using either a fine discritization grid for the rotordisk or to limit the value of the mass moment of inertia of the rotorblades. This means that either the size of the coaxial rotorcraft that can be simulated is limited or it takes more time to calculate the results. An additional problem was finding the correct and complete input data for the model. This was especially the case for the aerodynamic lift and drag data, which was difficult to find for the low Reynolds number flow conditions. The initial goal was to make a model of a generic coaxial rotorcraft. Which should be able to calculate the trimmed flight situation fast and accurate. This model should also be able to provide performance data to evaluate a design. One of the conclusions that can be drawn is that the developed model requires more time than was expected to find a usable solution. This means for the Newton iteration method a calculation time of minimal three hours. Using the sweep calculation is not much faster. The extra calculation time is due to the number of iterations required to find a steady state trim solution. Most of this calculation time is spent on calculating the numerical model's aerodynamics and interference effects. Due to the absence of reference material, the trimmed flight results are difficult to validate. The results show, however, a reasonable behaviour compared to the reference model. All typical characteristics of the coaxial rotorcraft, like no cross-coupling between lateral and longitudinal motion, can be observed. Additional insights are provided by the numerical method. These are among others, how the load and power are distributed between the two rotors.

Comparing the final state of the developed model to the set goal. It has to be concluded that a fast and accurate method to evaluate a design is not feasible. The main problem is the required calculation time to obtain the level of accuracy. It is proposed to use either Computational Fluid Dynamics or analytical calculation methods which are more accurate or faster. At a small scale, however, Computational Fluid Dynamics results are unproven. This leaves conducting windtunnel tests to obtain the same results at this small scale. Also, here it is uncertain the results can be obtained. A benefit of windtunnel tests is the generation of additional data. This data could then be used to verify these numerical models.

Contents

List of Figures

List of Tables

Nomenclature

Latin Symbols

A	disk area to be used for momentum calculation	$[m^2]$
A	wake constant	$[-]$
a	speed of sound	$[m/s]$
a_0	Coning angle	$[rad]$
a_1	Longitudinal tilt of the rotor disc plane w.r.t. the control plane	$[rad]$
B	number of rotor blades	$[-]$
b_1	Lateral tilt of the rotor disc plane w.r.t. the control plane	$[rad]$
C	Climb velocity	$[m/s]$
C	Sutherland's constant	$[K]$
c	chord length	$[m]$
C_t	Thrust coefficient	$[-]$
C_{att}	influence factor	$[-]$
$C_{d,f}$	friction drag coefficient	$-]$
$C_{d,profile}$	the profile drag coefficient	$[-]$
C_{Dp}	pressure drag coefficient	$[-]$
$C_D S$	estimated drag area	$[m^2]$
C_d	look-up table drag coefficient 2d	$[-]$
C_{l0}	lift coefficient at zero angle of attack	$[-]$
$C_{l\alpha_{fin}}$	Lift curve slope of the vertical tail	$[rad^{-1}]$
$C_{l\alpha_{hs}}$	Lift curve slope of the horizontal tail	$[rad^{-1}]$
$C_{l\alpha}$	lift-curve slope 2-dimensional	$[rad^{-1}]$

c_{la}	lift-curve slope	$[rad^{-1}]$
C_l	look-up table lift coefficient 2d	$[-]$
C_m	2D moment coefficient	$[-]$
D	Total drag	$[N]$
D_{fus}	Fuselage drag	$[N]$
dd_p	section drag	$[N]$
dKa	Aerodynamic force on blade element	$[N]$
dl	section lift	$[N]$
dm	mass of a blade element	$[kg]$
e	hinge offset	$[m]$
EI	Bending stiffness	$[N/m]$
F	Prantl tip-loss correction factor	$[-]$
f	correction factor exponent	$[-]$
f	objective function	$[-]$
g	Gravitational acceleration	$[m/s^2]$
h	altitude (height)	$[m]$
H_{first}	vertical distance at which the first function ends	$[m]$
h_{nd}	vertical distance between the rotors	$[m]$
I_b	Moment of inertia about the flapping hinge	$[kg \cdot m^2]$
I_β	Moment of inertia about the flapping hinge	$[kg \cdot m^2]$
inc	increment for finding trim solution	$[-]$
j	inverse wake contraction ratio	$[-]$
k	induce power correction factor	$[-]$
K_p	Controller gain for the roll rate	$[-]$
K_q	Controller gain for the pitch rate	$-]$
k_β	spring stiffness rotor hub	$[\frac{N}{m}]$
K_ϕ	Controller gain for the fuselage roll angle	$[-]$
$K_{\theta F}$	Controller gain for the fuselage pitch angle	$[-]$
k_{fus}	Fuselage shape factor	$[-]$
L_{fin}	Yaw moment of the vertical tail	$[N \cdot m]$
M	Mach number	$[-]$
M_a	aerodynamic moment	$[N \cdot m]$
M_{hs}	Pitch moment of the horizontal tail	$[N \cdot m]$
N_b	number of rotor blades	$[-]$
N_{fin}	Roll moment of the vertical tail	$[N \cdot m]$
p	pressure	$[Pa]$
p	roll rate	$[rad/s]$
P_{dp}	Drag power (rotor)	$[W]$

P_d	partial pressure dry air	$[Pa]$
P_i	Induced power (Rotor)	$[W]$
P_{sat}	saturation pressure	$[Pa]$
P_v	partial pressure fluid(water)	$[Pa]$
Q	source strength ground effect calculation	$[-]$
q	pitch rate	$[rad/s]$
R	Rotor radius	$[m]$
R	Specific gas constant	$[\frac{J}{kg \cdot K}]$
r	local blade radius	$[m]$
R_d	specific gas constant air	$[\frac{J}{kg \cdot K}]$
R_v	specific gas constant water	$[\frac{J}{kg \cdot K}]$
Re	Reynolds number	$[-]$
S_{fin}	Vertical tail surface area	$[m^2]$
S_{hs}	Horizontal tail surface area	$[m^2]$
T	Temperature	$[K]$
T_{inf}	thrust without ground effect	$[N]$
T_{gl}	Thrust calculated using the Glauert momentum method	$[N]$
T_g	Thrust in ground effect	$[N]$
$trimvar$	trim-variables vector	[-]
u	velocity in x-direction	$[m/s]$
U_P	Velocity Perpendicular to the blade element	$[m/s]$
U_T	Velocity Tangential to the blade element	$[m/s]$
V	total velocity	$[m/s]$
v	velocity in y-direction	$[m/s]$
V_b	Total velocity as seen by the blade element	$[m/s]$
v_i	Induced velocity	$[m/s]$
V_{fin}	Velocity at the vertical tail	$[m/s]$
V_{hs}	Velocity at the horizontal tail	$[m/s]$
$v_{i\,\text{inf}}$	induced velocity without ground effect	$[m/s]$
v_{ig}	Induced velocity in ground effect	$[m/s]$
Vol_{fus}	Fuselage volume	$[m^3]$
vpa	vertical flightpath angle	$[rad]$
W	Weight	$[N]$
w	velocity in z-direction	$[m/s]$
wc	wake contraction ratio	$[-]$
x	Coordinate along the X-axis in the body axis	$[m]$
x_{fin}	X-position of the vertical tail	$[m]$
X_{fus}	Fuselage X-force	$[N]$

x_{hs}	X-position of the horizontal tail	$[m]$
y	Coordinate along the Y-axis	$[m]$
Y_{fin}	Side force on the vertical tail	$[N]$
y_{tip}	radial coordinates of the tip vortices	$[-]$
z	Coordinate along the Z-axis	$[m]$
z_{fin}	Z-position of the vertical tail	$[m]$
Z_{fus}	Fuselage Z-force	$[N]$
Z_{hs}	Horizontal Z-force	$[N]$
z_{tip}	axial coordinates of the tip vortices	$[-]$

Greek Symbols

α	Southwell coefficient	$[-]$
α	angle of attack	$[rad]$
α_{0hs}	Initial angle of attack of the horizontal tail	$[rad]$
α_c	Angle of attack of the control plane	$[rad]$
α_d	angle of attack of the disk plane	$[rad]$
α_{fus}	Angle of attack of the fuselage	$[rad]$
α_{hs}	Angle of attack of the horizontal tail	$[rad]$
β	Flapping angle	$[rad]$
$\beta_{0_{fin}}$	Initial side slip angle of the vertical tail	$[rad]$
β_{fin}	Side slip angle of the vertical tail	$[rad]$
χ	blow back angle (skew angle)	$[rad]$
δ	azimuth angle of a wake vortex element	$[-]$
δ	finite change length	$[[m]]$
γ	lock number	$[-]$
Λ	wake coefficient based on the thrust coefficient	$[-]$
Λ_i	Non-dimensional induced velocity with attenuation correction	$[-]$
λ_i	non-dimensional induced velocity	$[-]$
Λ_0	Non-dimensional induced velocity	$[-]$
Λ_{i_u}	Non-dimensional induced velocity of the upper rotor	$[-]$
μ	tip speed ratio (also called advance ratio)	$[-]$
μ	viscosity	$[Pa \cdot s]$
μ_x	normalized velocity in x-direction	$[-]$
μ_y	normalized velocity in y-direction	$[-]$
μ_z	normalized velocity in z-direction	$[-]$
μ_0	reference viscosity	$[Pa \cdot s]$
ν	dynamic viscosity	$[-]$

Ω	rotation rate	$[\frac{rad}{s}]$
ω_b	non-rotating blade flapping natural frequency	$[s^{-1}]$
ω_{nr}	non-rotating natural frequency	$[s^{-1}]$
Φ	Relative humidity	$[-]$
ϕ	Inflow angle	$[rad]$
ψ	Azimuth angle of the rotor blade	$[rad]$
Ψ_w	wake age sing the first calculation function	$[rad]$
Ψ_{wn}	wake age using second calculation method	$[rad]$
ρ	air density	$[\frac{kg}{m^3}]$
ρ_{ha}	density humid air	$[\frac{kg}{m^3}]$
ρ_v	density fluid (water)	$[\frac{kg}{m^3}]$
τ_λ	time constant for the quasi-dynamic inflow	$[-]$
θ	Pitch angle	$[rad]$
θ_0	Collective pitch angle	$[rad]$
θ_{1c}	Lateral cyclic pitch angle	$[rad]$
θ_{1s}	longitudinal cyclic pitch angle	$[rad]$
θ_{tw}	Twist pitch angle	$[rad]$
υ_b	non-dimensional rotating flapping frequency	$[-]$

Subscripts

cp	of the control plane
i	matrix(vector) index
l	lower rotor
new	new value
old	previous value
tip	at the tip location of the rotor blade
u	Upper rotor

Abbreviations

2D	2-dimensional
BEM	Blade Element Method
CFD	Computational Fluid Dynamics
FVM	Finite Volume Method
GA	Guardian Angel
Ka	Kamov

MAV   Micro Aerial Vehicle
ODE   Ordinary Differential Equation
UAV   Unmanned Aerial Vehicle

<div align="right">

Chapter 1

</div>

<div align="right">

Introduction

</div>

With the current extensive usage of Unmanned Aerial Vehicles (UAV) also research and development on these UAVs is increasing. There are, however, a lot of different configurations and applications that can be distinguished.
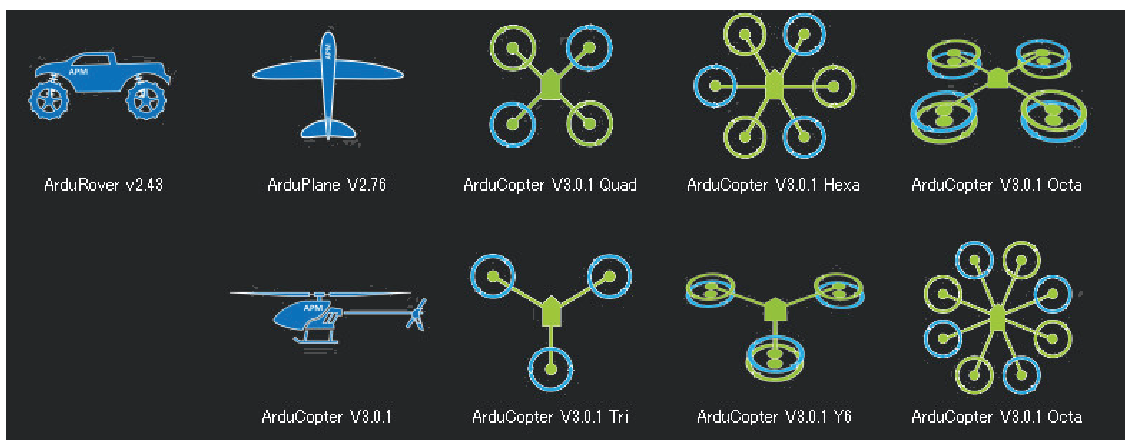
Figure 1.1: UAV Rotor configurations Robotics (2015)

Taking a look at a selection of the most used configurations used for UAVs as shown in figure 1.1, the coaxial configuration is not used much. Despite the advantages of inherent stability, quick control response and small size. All of which are positive traits for a small UAV. There are, however, also downsides to this design. These are, to name a few: a limited forward velocity and a high sensitivity to wind. Both are caused by the increased drag due to the increased size of the rotor head.

This last sensitivity is mainly due to the use of fixed pitch rotors and can be compensated using variable pitch rotors. This solution will make the model more complex, which is another downside. The mechanical complexity is due to the large number of moving parts required to have a working control system as well as a drive system to power the counter rotating rotors. The coaxial configuration is also used in multi-rotor UAVs, mainly to increase the load carrying capacity. Again, most of these applications use fixed pitch rotors. The general helicopter hazards like retreating blade stall and anti-torque failure are also reduced or negated for the coaxial configuration. This makes the design even more interesting due to its inherent safety. The safety is proven by the successful use of the design in full-size naval helicopters by the Russians PETROSYAN (2017), Foundation (2017).

Due to the advantages of the design and the lack of usage at small scale, an interest was taken in the subject. Why there are so little coaxial applications at this scale? and why

all control systems ignore the rotors pitch control as a means to control the rotorcraft? are just a few questions that can be asked.

1.1 Background

Gaining knowledge on the responses of a small coaxial rotorcraft and the knowledge on how to stabilize such a vehicle using simple control inputs is a key requirement for the applicability. This knowledge can also be used to design the craft itself or to design the control system. The coaxial MAVs have as their main usefulness that they are small and are able to carry a relative large payload. This means that they are able to operate indoor in difficult circumstances, like a burning building. Additional flying through doors and windows is made easier due to the compactness of the coaxial design. The coaxial rotor MAVs can thus be used to observe and report the situation of a fire using a thermal imaging camera while the operator is out of harm's way. One example of this is giving the fire department a view on the fire in a room of a large building. This is without the risk of losing a firefighter to an explosion. An example of such a coaxial MAV is a UAV design made for the fire department as part of a undergraduate work DSE (2011). The rotorcraft was designed to be used in observation missions indoors in burning buildings. The resulting UAV is 22.4 *cm* height and has a rotor diameter of 22.8 *cm*. It has a total weight of 574 grams and is shown in figure 1.2. Some of the problems that were encountered were:

1. the complexity of the control system of a coaxial rotorcraft

2. The small size meant the viscous effects, boundary layer thickness, stall behaviour cannot be neglected.

3. the external influences like incoming wind are relatively large for a small UAV.

To get a reference of the scale of the Guardian Angel MAV the Reynolds number and Mach number are compared to other aerial vehicles. It can be observed that birds are flying in the same conditions as can be seen in figure 1.3. With this research the hope is to lay down some basic rules and boundaries, so future preliminary designs can be made faster and more accurate.

The design specifications for a UAV from the fire department showed the need to be able to quickly assess a design made for a coaxial configuration. For this, a model is needed, which is able to evaluate different aspects of the design with respect to the design variables and flight conditions. The most important aspects are the aerodynamic performance of rotorblades, like figure of merit, thrust coefficient and power requirement. And the general performance of the rotorcraft. This means performance indicators like maximum velocity and best rate of climb.

1.2 Objective and Aims

This thesis will further investigate the performance characteristics of the coaxial rotorcraft with specific attention for how the Blade Element Method (BEM) holds up at the scale

Figure 1.2: Guardian Angel Coaxial Rotorcraft DSE (2011)
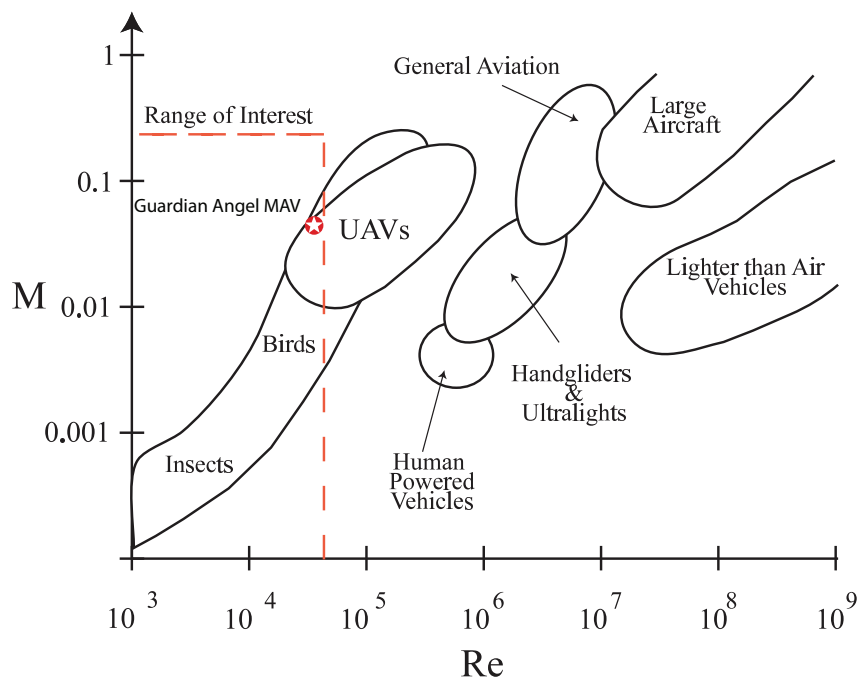
Figure 1.3: Reynolds- and Mach number range of Interest. Figure from Bohorquez (2007)

of the Guardian Angel MAV. For this purpose the Reynolds number and viscous effects are introduced and incorporated in a new to develop rotor calculation.

The BEM is a mathematical process to determine the behaviour of rotors. It involves breaking a blade down into several small parts. Then, determine the forces on each of these small blade elements. These forces are then integrated over the blade and over one

rotor revolution to obtain the forces and moments produced by the rotor. The modelling of the induced velocity on the rotor disk is a key aspect. It either has to be assumed or calculated. The viscous effects are caused by the medium's viscosity. The Reynolds number expresses the ratio between the inertial forces and the viscous forces, so when the rotorcraft operating point moves to a smaller Reynolds number the viscous forces become more important.

The main viscous effects that are incorporated in the rotorcraft model can be summed up as.

1. The increase of the boundary layer thickness.

2. Unsteady flow phenomenon like (partial) separated flow.

3. Different behaviour for laminar and turbulent flows.

To be able to attain the performance results, an accurate model of a generic coaxial rotorcraft should be made. The generic model was chosen to make it easy to switch between test cases. The specific test cases to test the resulting model are explained in section 1.5.

Thesis Goals
The main goal is to implement a numerical integrating method for the rotor blades into a Modular Coaxial Rotorcraft Model. The goal is to find the effect of physical scaling with respect to the rotorcraft performance. The modular model set up was chosen because of the ease to change and test parts of the model. A modular structure consists of modules and links. Each module focuses on a single concept, like the calculation of body forces. A module is also self-contained,which means that it can be used independently. The different modules are connected by links. Each link describes the relation between two modules. In this way the complex coaxial model can be functional partitioned into discrete and reusable parts. Making the modelling and testing of the model easier. Another objective will be to adapt this model to use a BEM with the aerodynamic coefficients being provided by a look-up table. In this way the viscous effects can be incorporated.

The new model can be verified by comparing the generated results with those obtained by the reference model as seen in Campfens (2008). This model was made to simulate a coaxial rotorcraft, the Ka-32A with missing data supplemented by the Eurocopter SA-330. The reason for this was that the available data for the Ka-32A was not sufficient as explained in Campfens (2008). The helicopter has a rotor size of 15.8 meters in diameter with 3 blades per rotor. The fuselage has a length of 11.3 meters and a height of 5.5 meters and weights 11000 kilograms at maximum take-off weight. It is powered by two 1660 kW turbo-shaft engines. The complete list of specifications can be found in appendix A.1. Also, a commercial coaxial MAV was tested. The data for a Walkera Lama was used. The rotor diameter is 25 cm with two blades with a weight of 800 gram. A complete data set can be found in appendix A.2. The ultimate goal is to obtain a generic model, which is able to assess the performance of a coaxial MAV quickly. A design tool could then use the provided data to provide feedback for the coaxial design analysed. As a test case the Guardian Angels UAV designed for the fire department of Haaglanden was used. It has a rotor diameter of 22.8 cm, and 2 blades per rotor. The body is 12.4x12.4 cm and has a

height of 13.4 *cm*. It weights 574 gram, while having a 63 Watt electric motor as power supply. Again, more information can be found in appendix A.3. The research questions that can be asked are now.

- Which design parameters for the rotor have the most influence on performance?

    - Which parts have the highest contribution to the total power requirement?
    - Quantify the effect of the rotor interference on the power requirement? Especially at hover and low speed.

- List the uncertainties in modelling assumptions, which have influence on the application limits of the model.

- How well does the chosen rotor interference models perform with respect to the reference functions as published?

- What is the performance of the aerodynamic modelling using a database?

In the wake modelling the interference is the influence of the upper rotor on the lower rotor. This influence can be described both in magnitude and area of effect. The research objective that comes out of these questions is to investigate the operational envelope of a UAV with a coaxial rotor by making a comparison of all design variables for the flight performance parameters. The operational envelope refers to the capabilities of a design in terms of airspeed and load factor or altitude. It is closely related to more modern terms known as specific excess power and a doghouse plot, both different methods to describe the flight envelope. To be able to reach these objectives a list can be made with parts required to reach the results.

- Implement the aerodynamic look-up tables for the rotors.

- Include an interference model for the upper and lower rotors.

- Verify the model for performance and control using literature references

- Adapt the model to be used at small scale.

The research goal can then be formulated as to obtain a flight mechanics model with the goal of obtaining performance data like thrust, torque and required power. The model should be able to handle the normal changes in flow conditions at the rotorblades. The Reynolds number effect should be incorporated to be able to model the small scale effects. Also the number of steps and methods used to model the interference effects should be changeable this includes the rotor wake and ground effect modelling. The rotor wake is the flow field that is the result of the working of a rotor. The wake effect is mainly seen below the operating rotor due to the induced velocity created. As with the interference it has an area of effect and a magnitude. The ground effect is the increased lift and decrease of aerodynamic drag that is generated when the lifting surface is close to a fixed surface. When the rotorcraft flies at a level approximately at or below the rotor diameter there occurs a ground effect. It is caused by the ground interrupting the vortexes and

down-wash below the blade. Due to the inability of the vortexes to form effectively due to obstruction of the ground, the induced drag is reduced. To model this, the ground surface location and effect needs to be taken into account. The two methods found to achieve this effect are the method of images and the method of surface singularity. The method of images works by mirroring the lifting surface in the ground surface. The mirror image generates exactly the same forces as the original. In this way the flow through the ground surface is reduced to exactly zero. The method of surface singularity works by adding a singularity (source) directly below the lifting surface. The singularity strength is then tuned to obtain the same zero induced velocity at the ground surface. In both cases the required induced velocity is reduced by the presence of the ground. Thus, reducing the power requirement. This concludes the objectives and questions that are set out to be solved.

Challenges

The main challenges are the correct integration of the rotor forces. Also, the implementation of the interference modelling for the lower rotor will pose a challenge. The obtained model will be used to obtain trim calculations and power data. The goal is to get a fast and usable model for a design study. One of the challenges is to keep the calculation time within reasonable measure. The required calculation time should be less than,which is required for the Finite Volume Method (FVM) and/or Computational Fluid Dynamics (CFD) for the same problem. To make sure the method is cost effective.

1.3   State of the art / Literature review

Describing the flight performance of a coaxial rotorcraft can be divided into a number of parts. The most important parts to be described are the rotor itself, the rotor wake and the effect of the fuselage. The modelling of the rotor can be separated into a two parts. A well-understood part is the mechanic /kinematic modelling. It is also relatively easy to model. The second part is the aerodynamic modelling, which is more difficult to model. Here, a lot of variation in methods can be used for the modelling. Part of the aerodynamic modelling is the wake modelling. This means that the same modelling problems are encountered here. A number of methods are used to model these specific wake effects. With the term wake effects, the effect describing the wake on bodies inside it is meant. One of the methods to describe the magnitude of the effect is the induced velocity. In addition, complex behaviour is found in test results.

The body motion on the other hand is well known and simple to model. Deducing from the required parts the most difficult part to model is the rotor aerodynamics. This is including the wake and attenuation modelling. One of the methods to provide the induced velocity effect from a rotor in its wake is to use an attenuation coefficient. The attenuation coefficient shows how strong the effect from the rotor wake is at a specific point. In general, the effects are less at larger distances. An example of using attenuation coefficient is a method developed by Castles. It uses an array of attenuation coefficients for specified radial and azimuth locations at a certain distance from the rotor. The coefficient can be calculated from the geometry and the thrust coefficient from the rotor. These coefficients multiplied with the induced velocity of the rotor will reduce the induced velocity accordingly. Doing this for all points will define the flow field below the rotor.

From this the main area of interest of the literature study was determined to be the aerodynamic modelling of a coaxial rotorcraft and Micro Aerial Vehicles. At the start of this literature review a general overview of the modelling of coaxial rotorcraft MAV and related topics is made. With the goal to gain insight in the characteristics of "Coaxial Rotorcraft" and low Reynolds number aerodynamics and to find the state-of-art in coaxial MAVs.

1.3.1 Aerodynamic Modelling of Coaxial Rotorcraft

Large differences were found in the methods used in literature to model the aerodynamics of a rotorcraft. These range from solving the full Navier-Stokes equations to using the Rankine-Froude momentum theory, as seen in Bohorquez (2007). The momentum theory also known as disk actuator theory is a mathematical model of an ideal actuator disk. The rotor is modelled as an infinity thin disc. This disk induces a constant velocity perpendicular to the disk. Thus, the disk creates a flow around the rotor. Then, with a number of assumptions the power, torque and induced velocity can be calculated. According to Prior (2010) the main methods used are:

1. Simple momentum theory

2. Free vortex theory

3. Vortex transport

In Xu and Ye (2010) it is claimed that the flow physics of coaxial rotorcraft are less studied than those of a regular helicopter. A list of methods to study them is proposed. These are:

1. Slip stream method

2. Prescribed wake vortex

3. Free wake vortex

4. Vortex transport model

All these models are simplifications of the Navier-Stokes equations. Coleman (1997) performed a literature review for aerodynamic modelling of coaxial rotorcraft. A few interesting models were found and these will now be listed. In Germany Zimmer (1985) the rotor was modelled by 2D aerofoils which were curve fitted together to form a blade. The results were then combined with a propagating shed tip vortex, which was modelled for a short distance. The wake contraction in radial direction was specified for both rotors. Due to the acceleration of the flow the wake of a rotor will contract. One of the methods to take this into account is to define the wake at a specific point as a fraction of the rotor it came from. This term is the wake contraction ratio. Most of the methods to calculate this ratio are based on empirical data. The final induced velocity can then be found using Biot-Savart's law. The specified down wash can then be corrected with the use of continuity and momentum calculations at the blade positions.

The method slightly overestimates performance at high thrust settings. Also, the wake geometry shows a relative conversion between the upper and lower rotors tip vortexes. In Japan, a disc and a free-wake analysis was used to model the coaxial rotors. The free-wake analysis is a method using the potential flow theory to describe the flow field. This includes the flow at the blades and in the wake. A vortex sheet or a lifting line representation are used to describe the blades. The induced velocities in the wake can be calculated for all spatial directions leading to the local axial, tangential and radial velocities.

This model with the free-wake analysis includes a contraction ratio for the rotor wake. The swirl in the flow is also modelled. The swirl is the rotational velocity that is present after the flow has passed through the rotor. It causes a loss since the rotational velocity doesn't contribute to the thrust generated. The swirl also changes the behaviour of a rotor operating in the wake of another rotor. For this calculation the rotor was divided into a number of annuli across which pressure and swirl velocity are discontinuous. An annulus is a region bounded by two concentric circles. It is essentially a ring-shaped area. The pressure and swirl velocity above the rotor is not the same as below the rotor. This is caused by the produced thrust. The magnitude of the difference in swirl and pressure changes with the radial position on the rotor.

A more complex model was also made, here the rotor blades are represented as lifting lines with uniform circulation, the wake consisted of a finite number of discrete vortexes. The tip vortex trajectory was in good agreement with the theory of Landgrebe. Landgrebe's model is a parametric method to describe the tip vortex trajectories of a rotor blade. It uses the wake age, which is the angle since the blade has pasted. The wake is assumed to be undistorted in the x-y plane and the trajectories follow an epicycloidal form. The inner wake descends faster near the tip than at the root. Also, the tip vortex has a contraction that can be fitted with an exponential curve fit. The rotor with the highest collective pitch generally dominates the flow field. Striking is that the collective settings are almost equal for the upper and lower rotor for optimum performance. It was found that influence of the lower rotor on the upper using charted data as seen in T. . Nagashima and Nakanishi (1981) yields an extra induced velocity for the upper rotor. Also, the annular vortexes used in this model causes an up-wash at these positions.

The Russians with the most practical application of the coaxial rotorcraft. Use the coaxial configuration mainly for naval application, while all western counterparts are conventional helicopters. The modelling of the coaxial rotorcraft is done using an equivalent rotor solidity model without the use of compressibility- or tip effects. The equivalent blade solidity is a correction on the blade solidity for a coaxial rotorcraft. For a conventional helicopter the rotor solidity is defined as the ratio of the total blade area over the total disk area. This same ratio is used for the coaxial helicopter. Since the strict definition is not true for the coaxial configuration, it is called the equivalent rotor solidity. To model the coaxial rotorcraft the flow was assumed to be in-compressible. This means that the density is constant in both space and time. The general flight speed of a helicopter is below a Mach number of 0.3, which indicates a subsonic flow with only small compressibility effects. The compressible flow effect are, however, encountered when the relative motion of the rotor blades is added to the helicopter motion. In this case, the compressibility needs to be taken into account for a part of the rotor blades aerodynamic calculations.

The compressibility correction can be done by using the equations for the in-compressible flow an adjusting them to approximate the compressible flow. A number of these corrections were encountered. The most important were the Prantl-Glauert correction, Karman-Tsien rule and Laitone's rule. The rotors' performance were said to be independent of separation distance. This statement is checked using a blade vortex theory, which confirms this independence. The next model that is explained is modelling the rotor by a lifting disc with a circulation distribution. This is combined by a prescribed trajectory for the wake vortexes to account rotor on rotor interference. The basis of this model is a 2D rotor blade analysis using a tip loss factor. Both were obtained by looking at the interference effect on the induced velocity of single rotor. Making corrections for this interference is done by trial and error using windtunnel data as a reference. A tip vortex structure similar to a single rotor with a non uniform inflow for both discs including a spill overflow was found in this way. The most difficult was the correct implementation of the aerodynamics of the airframe in the coaxial configuration model. Kamov uses an empirical method named ULYSS-6 to model this effect.

Coleman (1997) found the use of Blade Element Momentum Theory (BEMT) in the UK. The BEMT is a theory that combines both blade element method (BEM) and the momentum theory. The blade element method is combined with the momentum theory to solve the difficulties of calculating the induced velocity at the rotor. This model was combined with a vortex representation of the tip vortexes to model the wake. The method fails to take into account the pressure jump at the rotordisk. The upper rotors wake also does not contract. This paper has as outcome that the vertical rotor spacing lessens the vortex induced up/down wash. Calculus of variation and BEMT was used successfully by Lopez-Garcia, Cuerva, and Esteban (2012) to shape rotor blades for minimum required power. The required power was worked out as a function of the rotor blades shape using the Blade Element Method. Then, by variation of the different parameters describing the rotorblade an optimiser can find the shape for which the rotor blades use the least power for a given generated lift. The BEMT was used for this optimisation, despite its limit. This was because of weighing the importance of the accuracy of results against the calculation time required to obtain them. According to Prior (2010) no conclusions can be made about the positive or negative influence of the separation distance of the rotors. The key influences on the performance are the swirl recovery and the rotor diameter. The presence of a fuselage leads to higher average values and larger fluctuations of rotor thrust, this is one conclusion of Xu and Ye (2010). This is due to the up wash of the vortex flow on top of fuselage of coaxial rotorcraft. It turned out to be less than for a conventional rotorcraft.

According to Coleman (1997) test were made in Japan to visualize the tip vortex trajectory and compare it to Landgrebe's theory. The results show that the tip vortex has a higher axial velocities and the lower rotor has a lower radial velocity. The rotor with the highest collective pitch dominates the flow. Usually the upper rotor has more influence on the flow.The coaxial configuration in forward flight was also modelled in different ways according to Coleman (1997). In the UK forward flight was modelled using a classical skewed wake at high advance ratios and a free wake at low advance ratios. In general, the rotor wake will react to a forward flight velocity. One of the easy methods to take this into account is to define the wake as concentric tip vortexes at a skew angle. An example of such a skewed wake can be seen in figure 1.4. In Japan the modelling of the contraction

ratio in forward flight was tried. It turned out to be difficult to achieve correct results
with respect to test results.
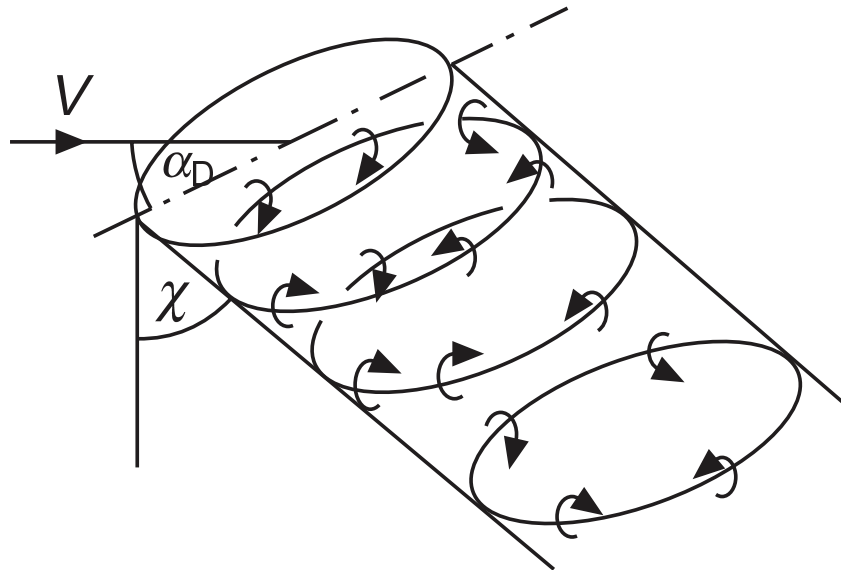
Figure 1.4: A schematic figure showing a skewed wake

1.3.2   Low Reynolds number Aerodynamics

The difference from the MAV aerodynamics with those of the conventional coaxial ro-
torcraft aerodynamics are the effects that occur when the rotor blades are scaled down
and the Reynolds number decreases. This means that for example the boundary layer
thickness is playing an increasing important role in the aerodynamics performance of the
coaxial rotorcraft. The boundary layer thickness is one of the parameters to describe
the boundary layer properties. At the surface of the aerofoil the fluid satisfies a no-slip
boundary condition and has zero velocity. Moving away from the surface the velocity
of the flow asymptotically approaches the free stream velocity. Even though there is no
sharp point at which the boundary layer becomes free stream, it has a well-defined thick-
ness. There are a number of methods to describe this thickness as well as the shape of
the boundary layer. These methods are:

99 % Boundary layer thickness The thickness is when the BL velocity is $0.99 \cdot u_0$.

displacement thickness δ The distance by which the surface would have to be moved
    from the reference plane in a inviced flow u_0 to give the same flow rate as the real
    flow.

Momentum thickness θ The distance by which the surface would have to be moved
    toward the reference plane in a inviced flow u_0 to give the same total momentum
    as the real flow.

Most of the applications found are using the displacement thickness method. Due to the
important role the boundary layer plays special attention was paid to the modelling of
flows at low Reynolds numbers.

In Bohorquez (2007) an analysis for hover at low Reynolds numbers was made using BEMT. At these low Reynolds number the viscous effects dominates the flow. The boundary layer is thick and needs to be taken into account. The upper rotor was affected by the rotor spacing and the aerodynamic influence is less when the distance is larger. To capture the low Reynolds number aerodynamics an aerofoil database was made using CFD and this was integrated into the BEMT. Such an aerodynamic database can be made by:

1. Experimental results of airfoil studies

2. Classical airfoil theory

3. Computational study, like CFD codes

The in-compressible Navier Stokes equation solver INS2D gives good results compared to windtunnel results. Acceptable results for the same conditions were obtained using the panel code Xfoil. The BEMT is difficult to extend for viscous losses from the aerofoil. This has mainly to do with the in-viscid base of the BEMT and extension lead to viscid CFD calculations. Standard practise for the BEMT is to use average lift and drag coefficients, but tabulated aerofoil data may also be used. The source for this data can also include low Reynolds number data. This method can be transformed to use non-uniform inflow as well as tip loss functions. The tip-loss functions were developed to investigate the optimal propellers. In this way the effect of the discrete number of blades can be dealt with. A second tip loss term can be used to take the reduced blade forces at the tip into account. The main tip-loss theories found are Betz, Prandtl, Goldstein and Theodorsen. Other methods like 3-D CFD require more calculation time and the vortex methods still require the 2-D aerofoil characteristic.

According to Motazed and Vos (1998) the aerodynamic modelling for performance has some technical challenges. The first is the effect of low Reynolds numbers, which is acknowledged by Liu, Chen, and Xiao (2002) and Sunada, Ohkura, Matsue, and Kawachi (2004). Also, the low aerodynamic efficiency of the rotorblades is observed by Leishman, Ananthan, and Gordon (2006) and a change in power density. These calculations were done with lifting line representation of the rotor blades and 2D profile drag to model the viscous effect. Also, Liu et al. (2002) uses 2D profile in combination with momentum theory and blade element approach to analyse micro rotor aerodynamics. The main advantages that are observed are fast computation time and simple inputs. These are ideal for design/analysis and based on classic propeller theory. The classic propeller theory also known as the actuator disk theory is a method to relate the performance to simple design parameters. In this theory the flow through the propeller is modelled as a gradual flow speed increase, with a jump in the stagnation pressure at the propeller disk. The rotation effect on the flow is neglected. Also, the flow behaves as an in-compressible fluid and is steady. Using these assumptions the thrust and power can be calculated. Also, the flow conditions can be calculated using the Bernoulli principle. Motazed and Vos (1998) and Leishman et al. (2006) used the simple momentum theory for coaxial rotors with a good optimisation and design results. Also, the BEMT is compared and found to give better results than the momentum theory. The results from both methods were checked with a free-vortex wake analysis as reference.

Syal and Leishman (2012) uses free-vortex wake analysis to do a parameter study for aerodynamic interference effect of inter-rotor spacing, blade twist angle and different blade

planforms. The rotor blades geometry was optimised for a minimum of the rotor induced losses. To keep the calculation time down a BEMT was implemented. The BEMT is also used by Liu et al. (2002) to set-up a simulation for hover. Again, the time required to find a solution was the reason for choosing the BEMT. Sunada et al. (2004) uses an annular momentum theory with BEM and compared this method to test results. The results show that the calculation method is capable of qualitative estimation of performance for blades with an aspect ratio of more than 10 at low Reynolds numbers. The most elaborate model found is used by Koehl, Rafaralahy, Boutayeb, and Martinez (2012). It is a detailed non-linear mathematical model for hover and near-hover conditions.

Following Sunada et al. (2004) the ratio between the thrust coefficient and the rotor solidity will increase with an increase of angle of attack. The error between analysis and measured flight test results even decreases with an increasing blade aspect ratio. Small collective settings and larger aspect ratios leads to a smaller error in the thrust and torque with respect to measured values. Large collective angles are not able to be analysed with the method used. A new Figure of Merit (FM) expression for coaxial rotors is proposed by Leishman et al. (2006). It is based on the thrust at torque balance, and leads to an optimum for maximum FM at uniform loading. For the operation of a coaxial rotorcraft it is required to have no resultant yawing moment or torque. This yawing moment is mainly generated by the two rotors. The most simple solution is to have both rotors generate the same amount of torque, due to the rotation direction of the rotors the torque will cancel out. This operating point is called torque balanced. This optimum leads to a uniform inflow for the upper rotor. While the optimum for the lower rotor leads to a double hyperbolic twist angle distribution with a breakpoint at the impingement point of the wake of the upper rotor. Also, the optimum planform differs as with torque balance there is an unequal rotor load. These interdependent loads require a multi-step optimisation according to Syal and Leishman (2012). The optimisation is done with method of feasibility and has as goal to find the blade geometry with the highest efficiency. The inherent aerodynamic difference results in different blade shapes for upper and lower rotor blades.

A low Reynolds number turbulence model in combination with an explicit 4-stage Runge-Kutta solver for the Navier-Stokes equations is used by Choi and Yoo (2000) to calculate the unsteady blade flow. The unsteady blade row flow is an unsteady flow due to a change of the object in-front of the blade. This unsteady aerodynamic phenomena can be described as fluctuations in the flow that are experienced by the rotor. If the fluctuations have a high frequency, the flow cannot be considered a series of steady flow patterns, which means it cannot be treated as a quasi-steady flow. The computational results are found in good agreement with the experimental data. Choi and Yoo (2000) found that based on k-ω model effects of the stator wake on boundary layer transition on rotor blade surface could be explained by a high turbulence level. This would induce early transition. The results were compared with an algebraic turbulence model. The effects of the kinetic energy loss and skin friction are found to be not significant. Further the results depend on the extent of the region of separated flow involved. The laminar-turbulent transition is the process of a laminar flow becoming turbulent. It is an extraordinarily complicated process that is not fully understood. It is known that the process proceeds through a series of stages. A boundary layer can transition to a turbulence through a number of paths. Which path is taken physically depends on the initial conditions such as disturbance

amplitude and surface roughness. The main process is shown in figure 1.5
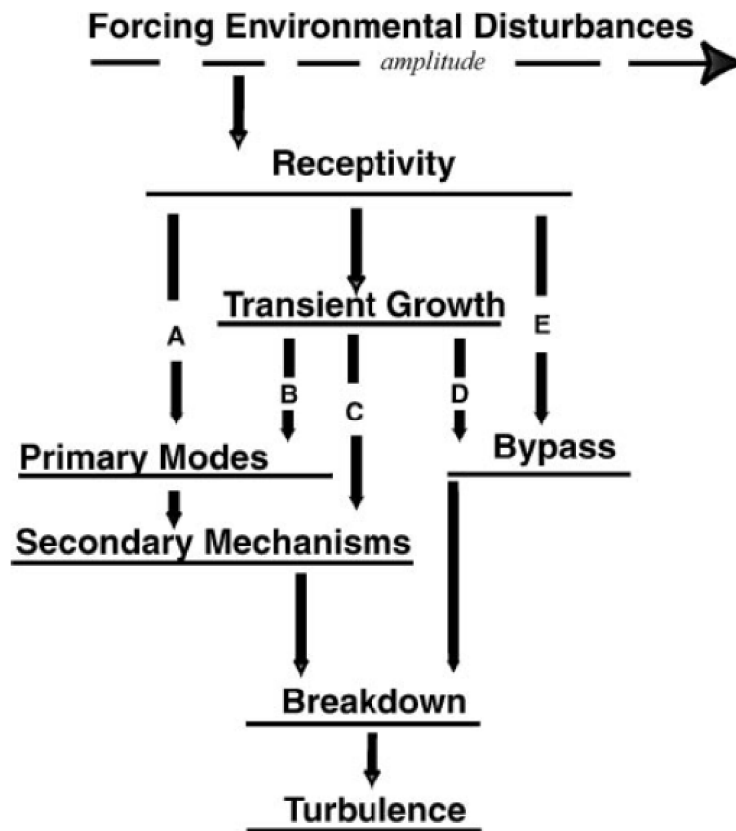
Figure 1.5: The different path for transition to a turbulent flow according to Morkovin MV (1994)

The k-ω turbulence model is used in computational fluid dynamics and is a turbulence model that is used as a closure for the Reynolds-averaged Navier-Stokes equations (RANS). The model attempts to predict turbulence by two partial differential equations. One for the turbulence kinetic energy and the second for the specific rate of dissipation of the turbulence kinetic energy. The RANS equations are time-averaged equations to describe the motions of a fluid flow. It uses the Reynolds decomposition to simplify the Navier Stokes equations by substituting the sum of the steady component and the perturbation of the velocity profile with the mean values. The result is equations that contain a non-linear terms known as the Reynolds stresses which give rise to turbulence. The idea behind these equations is that the instantaneous quantity is decomposed in its time-averaged and fluctuating quantities. These equations can be used with approximations of the properties of flow turbulence to give approximate time averaged solutions to the Navier-Stokes equations. Also, Butler, Byerley, VanTreuren, and Baughn (2001) found aerodynamic separation on the turbine blade suction surface. This leads to unpredictable losses at low Reynolds numbers. His goal was to gain insight in boundary layer transition and separation for a turbine blade at low Reynolds number conditions. Butler et al. (2001) found that increasing the turbulence level will move the transition point on

the suction side upstream. In all low turbulence cases, separation was observed while in turbulent cases transition took place. He notes that turbulence length scale and intensity are important for turbine blade aerodynamics. These findings might be important for use in design or CFD calculations.

J.Schroeder (2005) did a computational study to investigate the low Reynolds number flow physics and find fundamental flow properties. The validation was done by experimental data at a Reynolds number of 60,000. Special attention was paid to predict the laminar separation bubble on the upper side of the aerofoil. The laminar separation bubble may occur at low Reynolds number flows. A laminar separation bubble is caused by a strong adverse pressure gradient, which makes the laminar boundary layer separate from the aerofoil surface. The separated laminar flow is highly sensitive to disturbances. This will cause it to transition to the turbulent state. The region where the turbulent flow touches the surface again is the reattachment point. The volume enclosed by these flows is the laminar separation bubble. Good agreement between the computational results and the test results was found for the lift, drag and moment in static cases. There was less agreement in the 3D hover case. The thrust and figure of merit were over-predicted for all collective angles. To improve results it is suggested including a better vortex resolution and wake capture to ensure that the flow physics are solved better. According to J.Schroeder (2005) the development of rotary winged MAVs is hindered by poor aerodynamic efficiency and the onboard power requirements. For this reason, the aerofoil modelling is important for a better simulation model. It is, therefore, suggested for future work to incorporate the blade aspect ratio and Reynolds number into the BEMT to model the aerodynamic degradation. To have a good model it is essential to take the less than ideal situations of the rotor operation into account. This is called rotor degradation in the literature. The main degradation effect found are the viscous effects and the compressibility effects.

Kim and Koratkar (2005) did an investigation into the aerodynamic performance of micro rotors. The numerical model features unsteady blade motion and is compared to experimental results. The idea was to use dynamic blade pitch to delay onset of stall, thus enhance lift and increase the operating envelope. Controlling the blade pitch resulted in a significant improvement of thrust in the post-stall regime. For the effects on the thrust and power of a micro-rotor the experimental results agree well with the numerical predictions. Inspired by natural flyers (insects, birds) Truppel and Rossi (2011) explored rotational power consumption of rigid flapping wings at a Reynolds number of 4,500. The search for wing kinematics effects to reduce power consumption. Passive deformations due to aerodynamics of the wing was modelled by Truppel and Rossi (2011). The code couples a viscous in-compressible flow solver and an immersed-boundary method with a non-linear finite-elements solver for thin walled structures. The effects of wing stiffness, mass ratio and phase angle of active pitching as well as Reynolds number were investigated. Also, the symmetric wing kinematics was calculated to be used as reference. To keep a similar angular velocity the wing kinematics was checked every time. The result is a reduction of 10 % in power consumption, while the produced lift is reduced by 9 % with respect to the symmetric wing kinematics. A second test with more relaxed limits showed a new wing kinematics profile. The new profile shows a 60 % reduction in non-ideal power consumption, while the maximum lift coefficient is only reduced by 1.7 %. This might be interesting for the increase of the MAV endurance. Dai, Luo, and Doyle (2012) looked

into the dynamic pitch moment of wings. For this purpose an elastic rectangular wing was modelled computational using 3D fluid structure interactions at low aspect ratio in hover. The flapping motion dominates the non-uniform deformation according to Dai et al. (2012).

The flapping motion is the description of the motion of the rotor blades when operating. This is normally done by describing the flapping angle $\beta(t)$. One of the well-known methods is to describe the motion with an in-homogeneous linear differential equation with periodic coefficients. For this the Fourier coefficients of this motion can be calculated. Aerodynamics can significantly modify the angle and rate of passive pitch. Dynamic pitch depends on kinematics of wing root, wing stiffness, wing inertia and aerodynamics forces and also on wing deformation. Wing stiffness effect was analysed using the flapping frequency ω and the natural frequency ω_n. When the ratio was below 0.3 the deformations could enhance lift and lift generation efficiency, despite a camber disadvantage. This efficiency is specially improved when the inertial pitch torque is assisted by the aerodynamic torque of comparable magnitude.

1.3.3 Flight mechanics and performance

Felipe Bohorquez and Perel (2003) did a design and performance analysis for hover of a coaxial rotorcraft MAV. Also, test were performed with a COTS MAV to check the results. The main reason for the research was the known issues associated with the feasibility of achievement of hover for an MAV. A BEMT model was implemented with aerofoil characteristics estimated from flight tests. The result was the best measured figure of merit of 0.42 for a single rotor configuration. In comparison to a full-scale helicopter the BEMT model shows an increase of profile drag for an MAV. Usually the definition of the profile drag is the sum of the form drag and the skin friction. However, it is often used to describe only the form drag. The form drag or pressure drag is caused due to the shape of the object. The size and shape of the body are the most important factors for the magnitude of the drag. In general, larger cross-sections will have more drag than thinner more streamlined bodies. The rotor drag increases from 30 % of the total drag at a full-scale helicopter to 45 % for a small MAV. It was also observed that the power loading and efficiency of the rotor increases with increasing number of rotor blades. The results of this initial feasibility study of Felipe Bohorquez and Perel (2003) are that it is possible to develop a controlled small coaxial rotorcraft.

A full compressible Reynolds-average Navier-Stokes solver was used by Lakshminarayan and Baeder (2010) to evaluate the predictive capabilities of this computational approach. Also, the characteristics of the unsteadiness in the aerodynamic flow-field of a micro-scale coaxial system was of interest. According to Lakshminarayan and Baeder (2010) the performance was well predicted for a range of rpm. and rotor-spacings. As the rotor spacing increases, the thrust of top rotor increases while lower rotor thrust decreases proportional, thus leaving the total thrust fairly constant. At very large rotor separation distances this thrust fraction approaches a constant value. It is also noted that the top rotor contribution goes from 55 % to 59 % for increasing rotor spacing. The observed unsteadiness is mainly caused by the blade loading and the wake effect. The blade loading is the rotor's thrust divided by the total area of the rotor blades. It can, however, also be defined as the ratio of total weight of a helicopter to the total area of a rotor. This

is also called disc loading. An additional high-frequency unsteadiness was also observed. This was caused by the shedding of the vortexes near the rotorblades trailing edge. The vortex shedding is an oscillating flow that takes place when a flow passes a bluff body at a certain velocity. In this specific case the vortex shedding is the vortex generated by the blade to produce lift/thrust. When this vortex reaches the end of the blade it cannot disappear so it is shed from the blade and will dissipate in the wake. The wake of the top rotor contracts faster compared to the wake of the bottom rotor. The main cause for this effect was found in the vortex on vortex interaction. Also, the top-rotor wake convects down at a faster rate than the bottom-rotor due to an increased inflow seen at the top-rotor.

A dual rotor interference and ground effect study was done by Daniel A. Griffiths (2002). A free vortex wake model was developed with rotor-on-rotor interference and rotor in ground effect as goal. Due to constraints it is not possible to let the wake develop into infinity. It was, therefore, chosen to cut the wake development after a number of blade passes. Most of the wake calculations use the previous level to calculate the next level of the wake. This process could go on to infinity and take a long time to complete. For this reason, a choice has to be made when to stop. In other words, when is the wake truncation? It was observed that this truncation of the wake has an effect on the development of the solution. The rotor performance of a dual rotor system with a combination of vertical and horizontal separation (gap & stagger) was evaluated and compared to experimental results. A new momentum theory was introduced for over lapping rotors with a gap. This momentum method was used as a reference for the rest of the results. The free vortex wake models results show a beneficial aerodynamic interference effect for closely spaced staggered rotors. This is not the case for overlapping rotors.

The ground effect was modelled using two methods. The first is the method of images and the second is the method of the surface singularity. Mirroring the rotorcrafts down flow in the ground surface is called the method of images. In this way the ground surface is modelled as a surface with no resulting flow. The surface singularity achieves the same goal with a variable strength singularities at the ground surface. Just like panel codes it ensures that there is no flow through the ground surface. The result from the ground effect models were compared to the measured results and generally a good agreement was observed between the results.

H. W. Kim (2009) investigated the interactions between various components of the coaxial rotor configuration. The aerodynamics and acoustics of a generic coaxial helicopter with a stiff main rotor system with a tail mounted propulsor was assembled using Brown's Vorticity Transport model. The Brown's vorticity transport model is a specific model to describe the vorticity transport. It was developed to address the problem of dissipation. The full-configurations aerodynamics was then compared with that of specific parts or combination(s) of parts. The interference behaviour with respect to the system could be isolated in this way. Many interactions follow simple relations of cause and effect. There are, however, a number of inter-dependencies that have a more obscure relation. Traditional interactions are analysed using a network of possible interactions, all interactions have their own effect. This system obscures the close-loop nature of some aerodynamic interactions. It is suggested using modern numerical simulation techniques to replace the simple cause and effect interactions. This is with the goal to prevent unforeseen interaction-induced dynamic problems in helicopter design.

A sidestep was made by Benedict, Ramasamy, and Chopra (2010) by performing flow field measurements and assessing the performance of a small-scale cyclorotor for application in an MAV. The Cyclorotor is a fluid propulsion device that converts shaft power into the acceleration of a fluid using a rotating axis perpendicular to the direction of the fluid motion. It uses several blades with a span-wise axis perpendicular to the direction of fluid motion. These blades are cyclically pitched twice per revolution to produce forces in any direction normal to the axis of rotation. An example of the operation principle can be seen in figure 1.6.
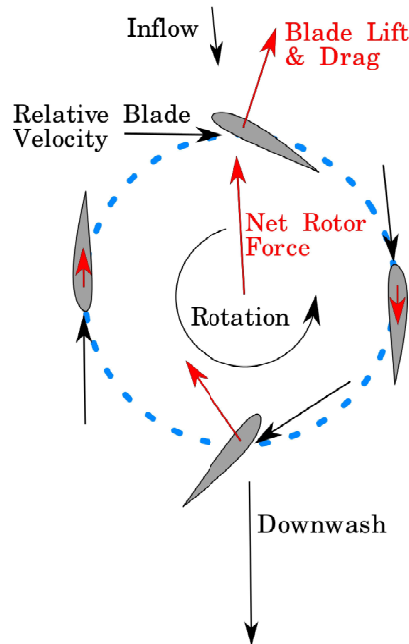
Figure 1.6: The operating principle of a Cyclorotor

The effect of a number of variables including number of blades and rotational speed was analysed by doing a parametric study on the results. The results show that the power loading and rotor efficiency increased when using more blades. This observation was made over a wide range of blade pitch amplitudes. Also, the profile drag coefficient of blade sections was calculated. This was done using a momentum deficit approach. The results correlate well with typical values at low Reynolds numbers according to Benedict et al. (2010). A number of particle image velocimetry measurements were made. The velocimetry shows there are rotational flows present. This fact combined with the influence of the upper wake on the lower half of the rotor explains the relative low efficiency of the cyclorotor. This principle may also be applicable to coaxial MAVs.

To perform system identification of a coaxial micro helicopter Schafroth, Bermes, Bouabdallah, and Siegwart (2010) developed a model. The goal was a design process for a heave controller for a coaxial micro helicopter. For this purpose a non-linear dynamic model was developed. It should reflect all important elements of a helicopter. Then, the system parameters are identified using measurement data collected from tests and flights. A form of non-linear identification was used together with an adaptation of an evolution strategy to form a covariance matrix for the model. The identified and verified model was then used to design a controller for attitude and Heave control. All the functions were

successfully tested in flight on a real system.

1.3.4   Conclusion

While performing this literature study, a lot of numerical methods were found to solve performance and flow calculations for coaxial rotorcraft. These range from solving the full Navier-Stokes equations as in Bohorquez (2007) to making use of a simple momentum theory in Prior (2010). Also, a number of extensions were found to make simple codes more accurate while maintaining the solution speed. Examples of this practice are the attenuation model in Campfens (2008) and the vortex tip representation as shown in Coleman (1997). The effect of the rotor spacing on the performance of the coaxial rotorcraft is inconclusive. The reviewed papers show claims of both positive and negative effects. According to Motazed and Vos (1998) viscous flow effects dominate the flow at low Reynolds numbers.

Another problem, which is observed is the need for numerical methods to weigh the solution speed and the accuracy of the results. An example can be observed in Liu et al. (2002). For the coaxial rotor configuration the optimum for upper rotor is different from the lower as is observed by Leishman et al. (2006). The main reason for this difference is the unequal load sharing because of the required torque balance as shown in Syal and Leishman (2012). With load sharing the distribution of the generated thrust in a coaxial rotor configuration is meant. The load is shared between the two rotors in various degrees. Depending on the flight conditions and collective input the upper rotor will generate more or less of the thrust.

The main problems observed with low Reynolds number aerodynamics are the turbulence and an unsteady flow causing unpredictable aerodynamic losses. Another phenomenon to take into account at this scale are the Laminar Separation Bubble and elastic blade deformation. Because of this aerofoil modelling is important for any numerical simulation. The modelling could be improved by a good wake capture and to incorporate blade aspect ratio as well as Reynolds number effects on the aerodynamic lift and drag. The main goal here is to model the rotor degradation. According to H. W. Kim (2009) another performance issue is the aerodynamic interference of the rotors on each other and on the fuselage. Also, profile drag is important for scaling down. It increases from 30 % to 45 % when scaling the rotors down as shown in Felipe Bohorquez and Perel (2003). Despite this all. The performance can be well predicted if the rotors influence on each other is modelled correctly as Lakshminarayan and Baeder (2010) published.

In table 1.1 the reviewed papers are listed with the relevant subjects treated by the paper marked.

Having looked at the state of art of small coaxial rotorcraft research. One of the things that was not found is a complete performance model of a coaxial MAV, for quick analysis and design. The model made by Lakshminarayan and Baeder (2010) contains a performance model for a coaxial MAV, but it uses CFD calculations to perform the calculations. This is deemed to complex and time-consuming for the applications in mind. The model used by Schafroth et al. (2010) also checks all the requirements in table reftab:littable but has the emphasis mainly in the controller design of an MAV and not on the performance calculations. While blade and rotor optimisation as well as rotor development is done

Reference	Flight Mechanics	Interference	Low Reynolds numbers	Experiments	Numerical Simulation
(Bohorquez, 2007)	✗	✓	✓	✓	✓
(Prior, 2010)	✓	✗	✓	✗	✓
(Coleman, 1997)	✓	✓	✗	✓	✓
(Zimmer, 1985)	✗	✓	✗	✗	✓
(T. . Nagashima & Nakanishi, 1981)	✗	✓	✗	✓	✗
(Lopez-Garcia et al., 2012)	✓	✗	✓	✗	✓
(Xu & Ye, 2010)	✓	✓	✗	✗	✓
(Motazed & Vos, 1998)	✓	✓	✓	✗	✓
(Liu et al., 2002)	✓	✗	✓	✗	✓
(Sunada et al., 2004)	✓	✗	✓	✓	✓
(Leishman et al., 2006)	✓	✓	✗	✓	✓
(Syal & Leishman, 2012)	✓	✓	✗	✗	✓
(Koehl et al., 2012)	✗	✓	✓	✓	✓
(Choi & Yoo, 2000)	✗	✓	✓	✓	✓
(Butler et al., 2001)	✗	✓	✓	✓	✗
(J.Schroeder, 2005)	✗	✓	✗	✓	✓
(Kim & Koratkar, 2005)	✓	✗	✓	✓	✓
(Truppel & Rossi, 2011)	✓	✗	✓	✗	✓
(Dai et al., 2012)	✗	✗	✓	✗	✓
(Felipe Bohorquez & Perel, 2003)	✓	✗	✓	✓	✓
(Lakshminarayan & Baeder, 2010)	✓	✓	✓	✓	✓
(Daniel A. Griffiths, 2002)	✗	✓	✗	✓	✓
(H. W. Kim, 2009)	✗	✓	✗	✗	✓
(Benedict et al., 2010)	✗	✓	✓	✓	✗
(Schafroth et al., 2010)	✓	✓	✓	✓	✓
(Campfens, 2008)	✓	✓	✗	✓	✓

Table 1.1: Literature overview of Coaxial Micro Aerial Vehicles

often. There was only one paper that looks at the effects of the fuselage on the rotor H. W. Kim (2009). Rotor-Rotor interference is done more often for example by Daniel A. Griffiths (2002) and Campfens (2008). Pure mathematical models for performance assessment of MAVs were not found. Most model found use test data for the aerodynamic modelling like Felipe Bohorquez and Perel (2003) or only try to improve performance using the same computational model.

Agreement can be found on the fact that speed and accuracy are not achievable at same time as stated by Liu et al. (2002) and Leishman et al. (2006). These authors also agree that BEMT is the method, which is easiest to modify to obtain a reasonable accuracy while still having a quick solution. The rotor spacing's influence is unclear, but still there are references for comparison of the results for coaxial rotorcraft. The principles of the flow behaviour at low Reynolds numbers is well understood. This means that effects like increased boundary layer thickness and the forming of a separation bubble are known. Modelling these is more difficult. Most papers reviewed use experimental data or empirical models to analyse the flow. The implementation of these flows is then coupled to an aerofoil profile. Using the local flow conditions to find lift and drag on the aerofoil. This can be achieved by a look-up in experimental data or by using calculation methods. The results can then be used in a general rotor code like the Blade Element Method. The conclusion is that no combination of a general rotor code and an aerofoil code with the goal to obtain the performance was found in the literature review.

1.4 Reference Model

In the literature review the conclusion was that there was no 'general' flight performance model. From this conclusion the choice was made to develop such a model. As the model made by Campfens (2008) already provides a lot of the required functions, it was selected to serve as a reference model. The model is explained in section 1.4.1. Because of the set goal a modular model as explained in section 1.2, this approach seems the best choice to change parts and modelling methods. For this a modular reference model was made from a chosen Reference model. The required changes and chosen structure of this model are explained in section 1.4.2. Finally, the Mmodular reference model is compared with the Reference model to verify the model. This section will also highlight the limits of these Models.

1.4.1 Coaxial Helicopter Model

The model made by John Campfens provides two functions. It is able to be used to find a trimmed flight condition. Also, the control quickness was assessed. This second part is less interesting for the current work as the performance will be assessed from the trimmed flight conditions. The control quickness is a model to see if the model response correct and fast enough to the control inputs.

The model consists of a single model file in which all the aspects of the model are described. The model file consist of a description of:

- the upper rotor flapping and force calculation

- the lower rotor flapping and force calculation

- the forces generated by the fuselage and tail surfaces

- the equations of motion

The functions used to calculate the flapping motion as well as the rotor forces are a closed-form analytical expression. The expression for the flapping motion was developed by Pavel (2001). Elaborations of the rotor forces are provided by Campfens (2008). Using a constant lift curve slope and an average drag coefficient the blade element method can be used as a base. The result is then integrated to a single expression for the forces that are present on the rotor. An example for the thrust coefficient can be seen in 1.1.

$$C_{TBEM} = \frac{1}{4}c_{l\alpha}\sigma[\frac{2}{3}\theta_0(1 + \frac{3}{2}\mu^2) - (\lambda_c + \lambda_i)] \tag{1.1}$$

In this model the assumption is made that the upper rotor only influences the lower rotor. This is because the effect of the upper rotor is larger. The upper rotor inflow will be treated as a uniform inflow. The upper rotor accelerates the flow the wake will contract. This has to be taken into account. The generalized wake model by Landgrebe (1972) was used in combination with the axial spacing of the rotors. The contraction ratio divides the lower rotor into two different regions. This means that there are two different induced velocities on the lower rotor surface. One outside the wake with only the induced velocity created by the lower rotor and one inside the wake. Here, the induced velocity effect is the combination of the induced velocity created by the upper and lower rotor. The induced velocity of the upper rotor has travelled and the effect has weakened. This is taken into account by a multiplication factor called the attenuation coefficient C_{att}. The induced velocity for the different areas of the lower rotor can now be calculated and just like the upper rotor be integrated into functions to calculate the forces on the lower rotor. The model file itself consist of a number of analytical expressions to calculate the forces from the flight condition. Then, using these forces to calculate the accelerations and powers requirements for the flight performance model.

This model is an analytical model made for a full-size coaxial helicopter with as specific test case the Kamov 'Ka-32A'. The Kamov Ka-32A is shown in figure 1.7. The corresponding trim curve as calculated by this model is shown in figure 1.8.
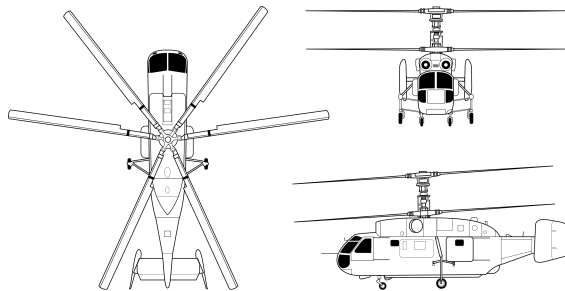
Figure 1.7: Kamov 32a used as reference calculation case

The analytical model will serve as a reference to check the results from the numerical model(s). The comparison will be made for the Ka-32A using the same input data for both the analytical and numerical model.
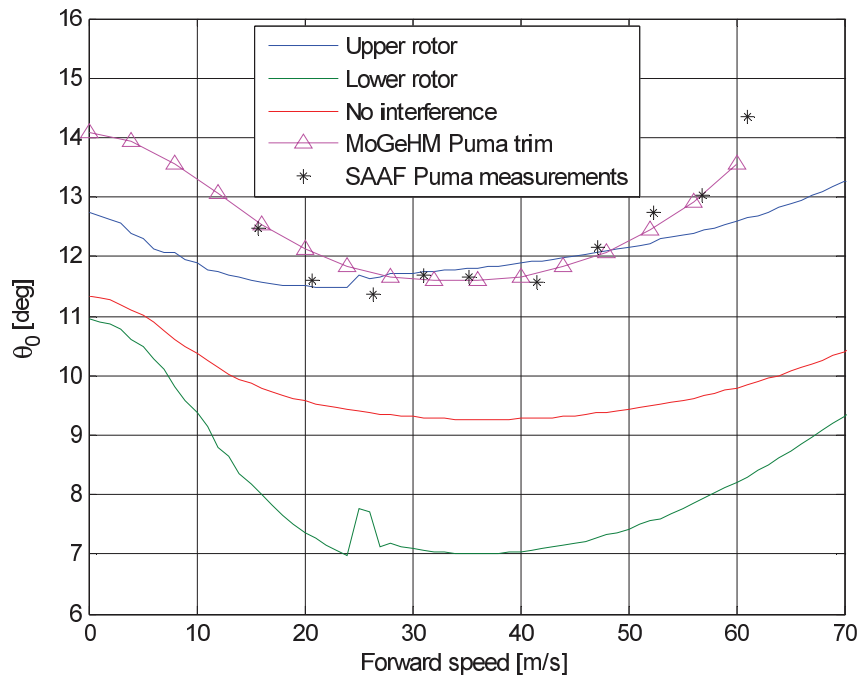
Figure 1.8: Longitudinal trim curve as taken from Campfens (2008)

1.4.2   Modular Model

The modular reference model is in essence the same as the reference model. The only change is the use of functions to calculate the behaviour of the upper- and lower rotor as well as the body forces and equations of motion. This means that in the new model the required data as well as the results have to be stored and passed through different from when all the data were used in the same part. The transformation is shown in figure 1.9. A single block in (a) shows the reference model. The inputs are the states and controls and the output are the rate changes of these states. In section 1.4.1 the calculation of the results from this model are explained. On the right the modular reference model is shown. The same states and controls as the reference model are used as input. Again, the output are the rate changes of the states.

The different modules can be seen inside the modular reference model in figure (b). These are Start-up which provides the base data read in for further use. The next module is the upper rotor calculation which calculates the flapping motion and forces on the upper rotor. This is without interference effect. The following module is the lower rotor here also the flapping motion is calculated as well as the forces that are present. This is all with the interference effects of the upper rotor as was implemented in the reference model. The third module is the calculation of the Helicopter forces. This is done using the same empirical functions used in the reference model. The last module is the Equation of Motion. Here, the forces and moments are summed to find the resultant forces and moments is all directions. Using these resultants the angular and translational accelerations can be calculated using the mass and moments of inertia. The outcome of this last module can then be used to calculate the trim condition for the given flight condition. The modular base is a requirement to be able and substitute parts to incorporate new methods. The

(a) Reference Model

(b) Modular reference Model
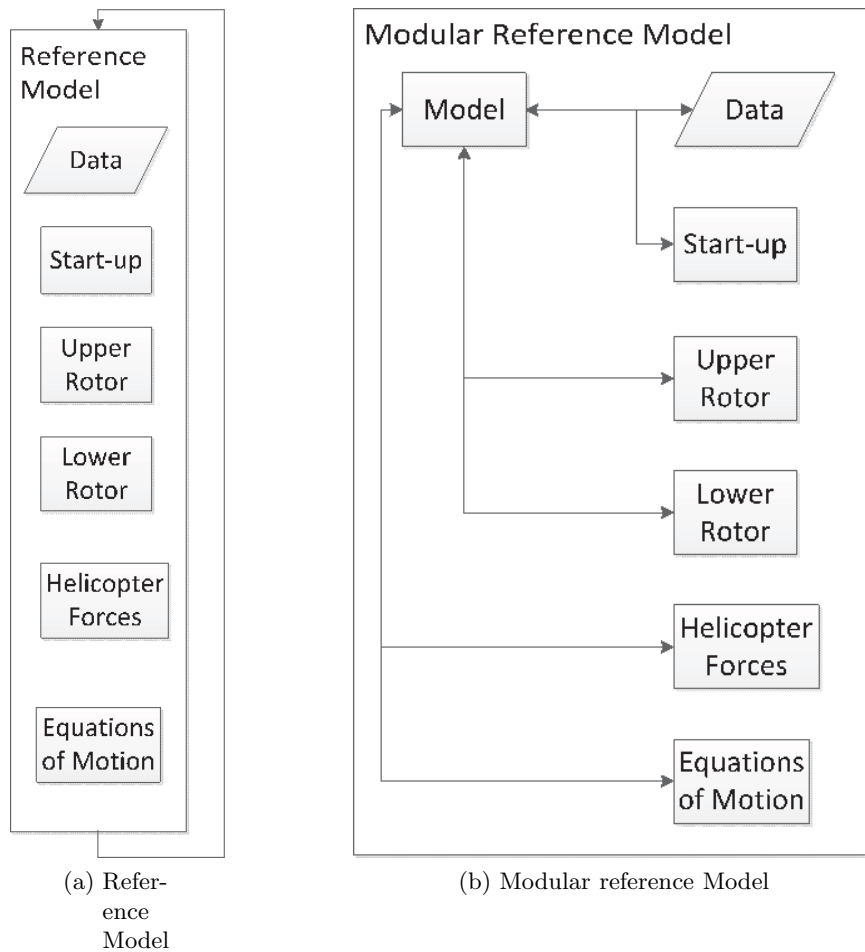
Figure 1.9: Reference models

test case to be calculated is the same Ka-32A as used in the reference case.

1.4.3 Verification

The modular model will be using the same analytical functions to calculate results. The choice was made to verify the results from the modular model by comparing the results with those generated by the reference model as developed by Campfens (2008).

The control inputs for a trimmed flight are shown in figure 1.10. The results from the modular reference model are shown in the solid lines, while the reference models results are plotted by the crosses. It can be seen that the results are almost the same. Even the switch points that are used to translate the wake to the back coincide.

The switch point for the wake attenuation calculation are used in the analytical model from Campfens (2008). It is making use of numerical attenuation method in the analytical force calculations. Knowing the contraction ratio, based on the thrust coefficient, and the forward velocity. The skew angle can be calculated for the positions where the wake
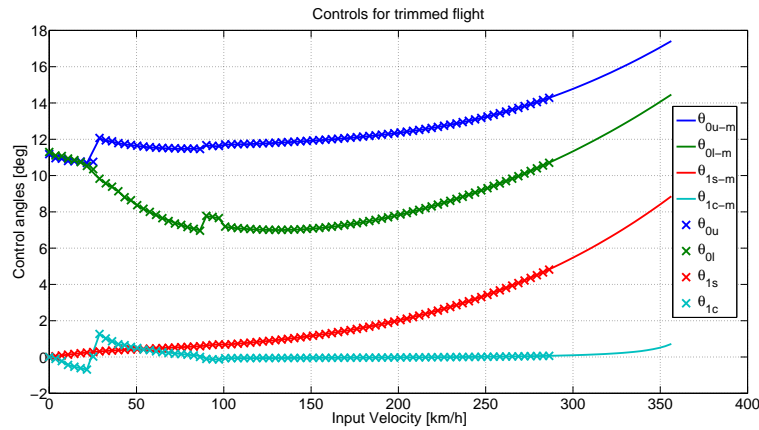
Figure 1.10: Comparison of the control inputs

(a) 38.44   (b) 77.46   (c) 84.17
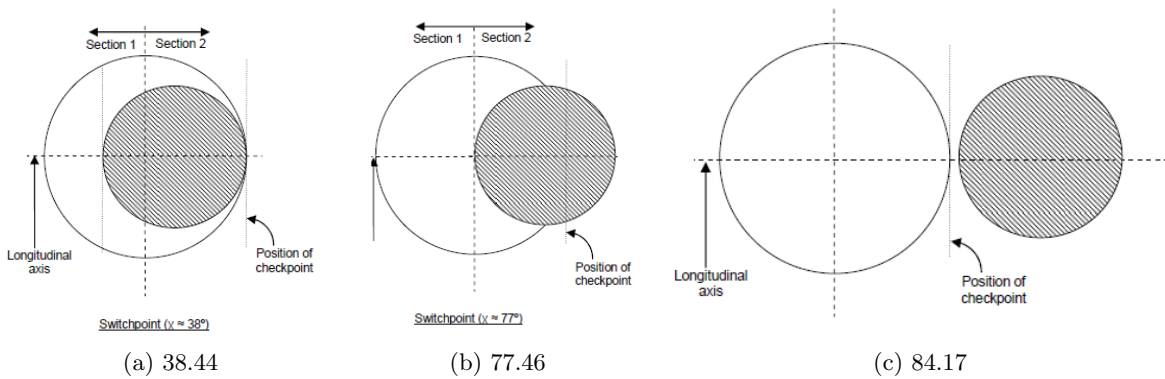
Figure 1.11: The transitions of the upper rotor wake on the lower rotor Campfens (2008)

boundary coincides with the rotor boundaries/positions. The transition of the wake from the upper rotor over the lower rotor was divided into four sections. For each of these sections the numerical methods were averaged so they can be used to calculate the rotor forces. The switch point are the points where the model switches from using one equation to another. In figure 1.11 these transitions are shown. The first transition is when the back of the rotor wake coincides with the back of the rotor at 38.44° as is shown in figure 1.11a. At 77.46° the next transition occurs. This is when the front of the rotor wake passes the centre of the lower rotor as is shown in figure 1.11b. The last transition is when the rotor wake leaves the back of the lower rotor. This happens at 84.17° and is shown in figure 1.11c. These transitions can be observed at 25.2 km/h , 90 km/h and 190.8 km/h in figure 1.10.

To check the implementation of the modular reference model not only the results from the rotor were compared. The fuselage orientation was also verified, the results can be seen in figure 1.12. Also, here the Reference model and the modular Reference model are almost exactly the same. Thus proving that the modular implementation is worked out correctly.
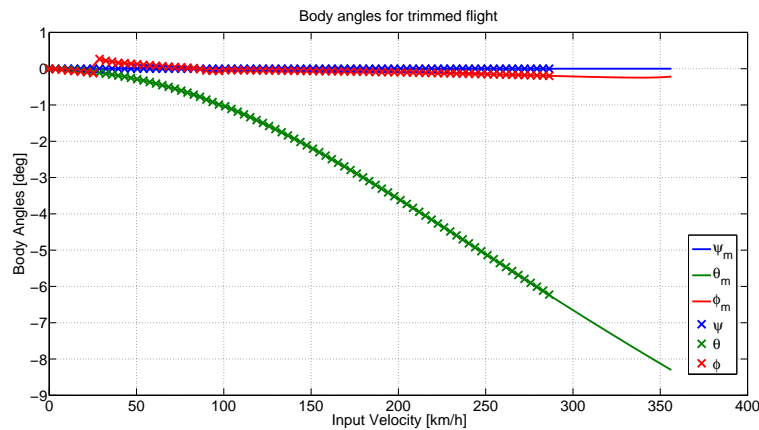
Figure 1.12: Comparison of the body orientation

1.5   Cases

Deducing from the set goal and the solution types found in literature. The new coaxial model should be able to handle Low Reynolds numbers and have a wake model incorporated. It is preferable to use existing methods to evaluate the coaxial rotorcraft, with the goal to quickly analyse the design specified.

The new parts to be modelled are:

1. Model the aerofoil

2. Model the rotor blade

3. Model the rotorhead to be combined with the rest of the rotorcraft model

The result should be a complete coaxial rotorcraft model, able to assess the performance of the rotorblades and rotorcraft. The use of look-up tables for the aerodynamic lift and drag coefficient is preferable. This data should link the flow conditions seen on the aerofoil to the forces generated by them.

The model described in section 1.4.1 was chosen to serve as the reference for the updated Modular model because it was a coaxial model solving for a trim condition. The updated model was developed in steps to be able to trace back problems that might occur.

The first case is the reference model as developed by John Campfens Campfens (2008). This model is explained in section 1.4.1.

The next case is a modular version of the reference model. This model is explained in section 1.4.2, and was verified to give the same results as the reference model in 1.4.1. Due to the requirement to change parts of the reference model the modular set up became a necessity. The result is the modular reference model.

Now for this modular reference model new modules for the aerodynamics and wake can be written. The aerodynamics is updated to use a look-up table instead of the lift curve slope and drag coefficients. Also, the rotor calculations are made independent of the
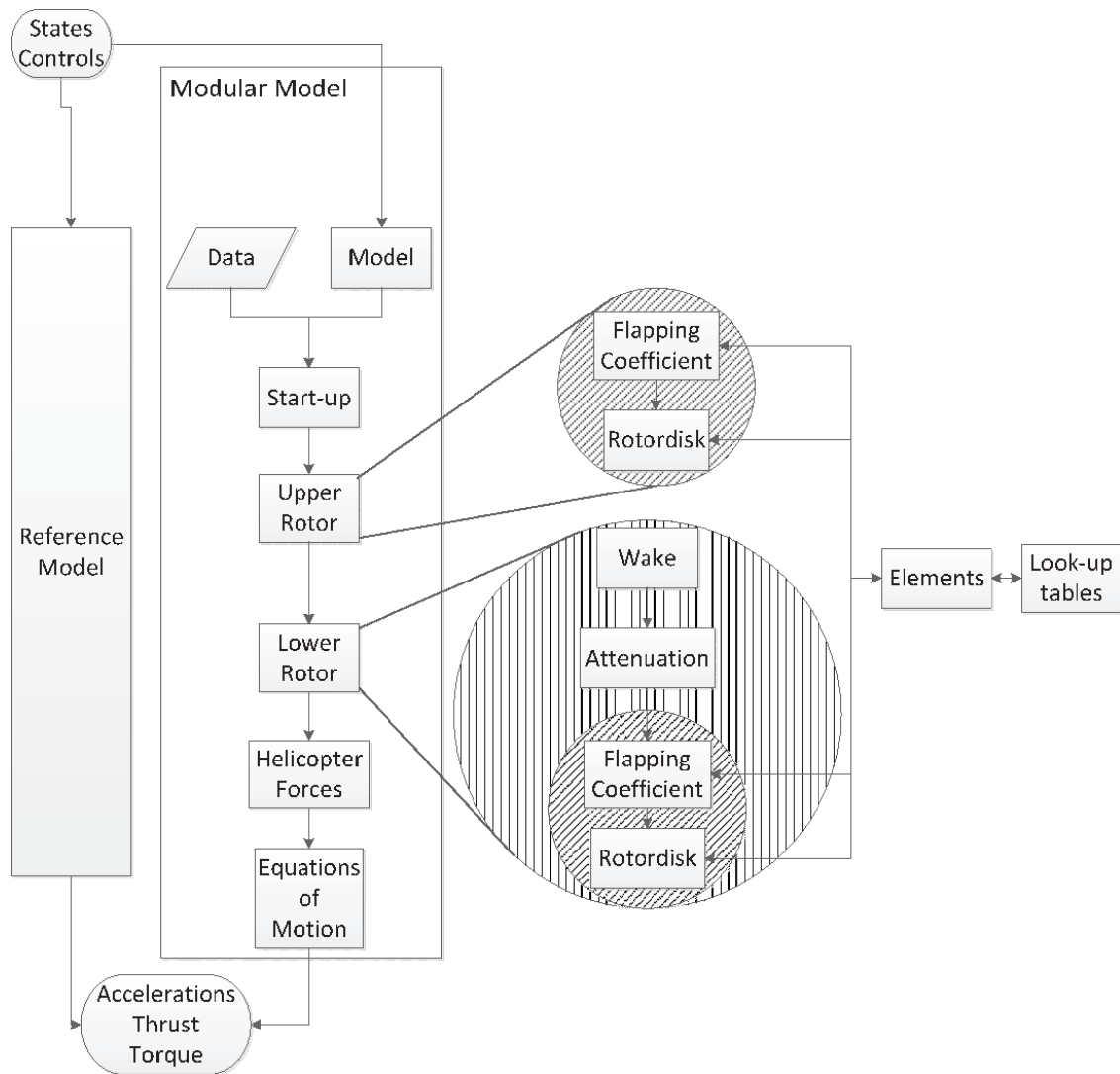
Figure 1.13: Models System Approach

position, either upper or lower, as is shown in figure 1.13. The upper rotor module is substituted by one module for the flapping motion and on for the rotor forces. Using the forces and moment resulting in the blades flapping motion the motion of the blades can be calculated and incorporated in the model. For this reason the lift curve slope $C_{l\alpha}$, used for the analytical calculation, was derived from the aerodynamic data because it was not present in the look-up table. For the lower rotor the same modules are used. In addition to a module for the wake and one for the attenuation of the wake as can be seen in figure reffig:ThesisSystemApproach in the lift outs (bubbles). This meant that also the wake and attenuation calculations have to be implemented.

Both the modules for the flapping motion and rotor forces use the look-up table. To be able to implement these 2D aerodynamics data it has to be translated for the rest of the model. The looked-up lift and drag is used to construct the forces on a blade element. This in turn is used in the flapping motion and rotor forces. The wake calculations

are extended using Castles and Leeuw (1953a) and Landgrebe (1972). In the Modular
Reference model the same methods are used, but the influence is averaged to obtain four
coefficients to describe the wake influence. These calculations are based on the thrust
coefficient C_T of the upper rotor.

The inflow conditions for the lower rotor are calculated by these modules forming an
inflow matrix. This matrix consists of the attenuation coefficient at a specific position
on the rotor. When this is done for all the positions on the rotor the result is a matrix
describing the effect of the upper rotor. A more detailed description can be found in
section 2.3.2. The result is a Modular updated model. To test this model the same test
case as in the previous two cases is used, with the base data of the Ka-32A.

The last case is the scaled modular model, which is essentially the same as the modular
updated model, but now the data for the Guardian Angles UAV is the input for the
calculation case. The GA UAV is shown in figure 1.14. It is a coaxial rotorcraft with
rotors of 22.8 cm diameter. The body is 12.4 cm x 12.4 cm and weights 574 gram.

Figure 1.14: Small scale UAV final goal to calculate

The changes are an update to the model to incorporate the use of down-scaled data at low
Reynolds numbers. This all to achieve the ability to calculate the trim and performance
at this small scale.

The main differences between the reference model and the new model are:

1. Model of the blade element

    (a) Aerodynamical
    (b) Mechanical

2. Integrate a number of elements into a blade

3. Integrate a number of blades over one rotation and average. Steady state

4. The same procedure applies for the bottom rotor with the addition that the input is different

5. Rotor wake

   (a) Contraction ratio
   (b) Skew angle
   (c) Attenuation matrix

6. Extra effect to be incorporated

   (a) Tip loss model

In table 1.2 a short overview is given of the test cases with there respective requirements and changes.

Test case	Changes
Reference model	No changes same model as in Campfens (2008)
Modular reference model	Modular version of the reference model.
Modular updated model	Update the aerodynamic calculation to use the look-up table.
Scaled modular updated model	Change the aerodynamic look-up table to use low Reynolds number table as well as the use of data input for the MAV.

Table 1.2: Table with the different test cases

1.6   Structure of the Report

The structure of this document is as follows. Chapter 2 is the description of the model. This consist of the theoretical background and mathematical work out of the modelling challenges. First the general layout and link between the different parts is described. The new to be modelled parts are explained in the next sections. The first section is the flapping motion. It first describes the general flapping motion followed by a description of the implementation of the differential method using the equation of motion for the blade as well as the description of the analytical method which was used to increase the calculation speed. This is followed by a section describing the theory and implementation of the aerodynamic modelling from the look-up table to the blade with its generated forces. Then, the section rotordisk will explain the way the environmental input is transformed to

be used for the look-up table as well as the transformations that have to be done to obtain the steady state forces and performance parameters. Next up is are the wake calculation. This section consists of the description of the wake contraction and the calculation of the attenuation coefficients. The last section is a description of the solvers used to solve the trim problem as well as the objective function(s) used to describe the trim condition.

Chapter 3 is the validation and verification of the model described in chapter 2. The verification is divided into two part consisting of two test cases. These are the numerical model to validate the use of the new numerical integration. And the small size model to verify the models working on small rotorcraft.

Then the conclusions that can be drawn from this process will be presented in chapter 4 as well as possible other applications of the work done. The recommendations will describe the possible extensions to the model and can be found in chapter 5. Also, tips for future work related to the model is discussed here.

Chapter 2

Numerical Model

2.1 Model Overview

As already stated, the model consists of a number of modules to calculate a specific part or process. The main improvements for this model consists of the implementation of a look-up table for the aerodynamic calculations. Also, the use of an attenuation matrix for the wake influence was implemented. The main input for the model are the definition of the rotorcrafts geometry and the aerofoil aerodynamic properties. These are defined in two input files. The geometry specification can be found in appendix A, while the aerofoil aerodynamics will be discussed in section 2.2.2.
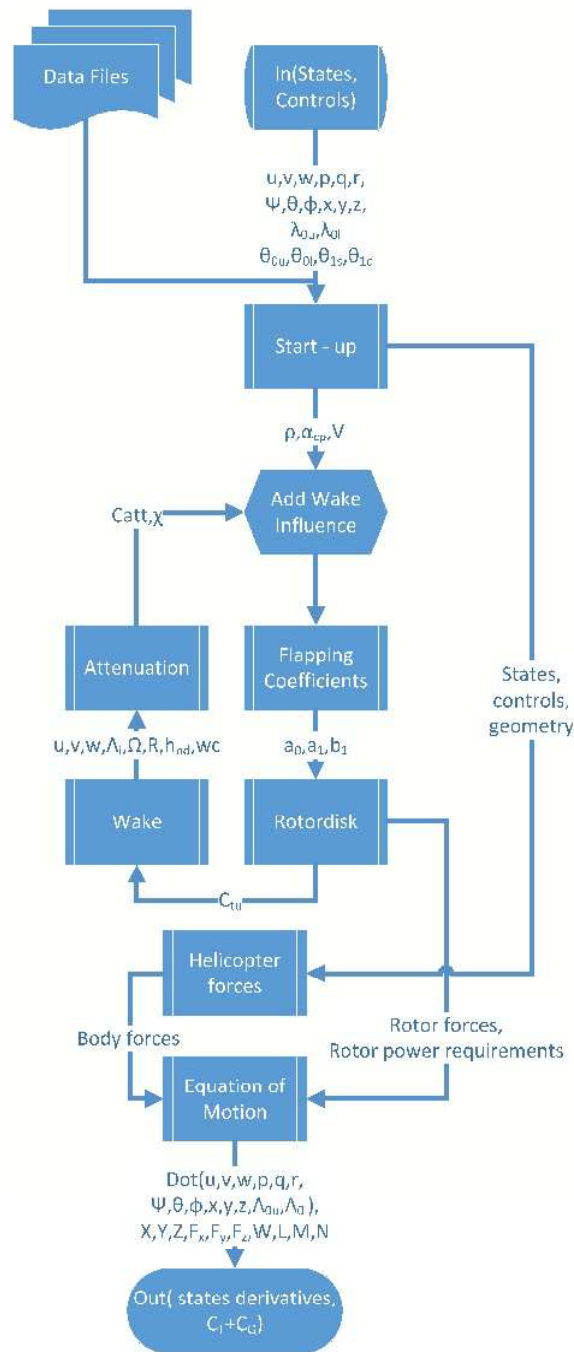
2.1.1 Workflow

The general workflow of the model is shown in figure 2.1 and described in the following section. The first step is to get the individual states from the state vector. Also, the control angles are assigned. The reference values for the normalisation are calculated as well. This includes the velocities in x, y and z direction, the lock number and the advance ratio μ.

Next is the calculation of the flapping coefficients. These can be determined by either solving an Ordinary Differential Equation (ODE) or by using empirical obtained functions from Pavel (2001). The ODE is derived from the equations of motion of the rotorblade. Both methods use aerodynamics and inertia data to perform the calculations.

The used functions and procedures can be found in section 2.2.1. For the calculation of the flapping coefficients especially for the ODE, the forces on the blade elements have to be calculated. To be able to *calculate* these forces, the aerodynamic modelling using a look-up table was implemented. The aerodynamic calculation is divided into three parts. It starts with the section for which the lift and drag are looked up. With two sections an element can be formed with the corresponding force distribution. Finally, these elements are combined to form a blade. A complete description of the implementation can be found in section 2.2.2. The Rotordisk will calculate the forces generated by the rotor blades, based on the corresponding flapping coefficients and the aerodynamics modules. Also, the first coordinate transformation will take place in this module, the transformation from rotorhead to helicopter body reference frame. An extensive explanation can be found in section 2.2.3The lower rotor is using the same functions as the upper rotor to calculate the flapping coefficients and forces.

The main difference is the input of the environment, which, is determined by the additional effects from the wake. This was also the main reason to model the flapping coefficients

Figure 2.1: Workflow diagram for the updated Model

and the rotor disk with many variables. Making it possible to use the same model for both functions with only the input and boundary conditions that change.

The wake calculations consists of two parts. These are:

1. the contraction ratio
2. the influence factor

These two parts are separated to be able to fine-tune the model's behaviour. It also gives the ability to update each part separately. Knowing the behaviour of the upper rotor the flow in the wake can be calculated. The wake contraction is calculated using Landgrebe's method as is described by Landgrebe (1971). The result is a relation for the tip vortex and the outer boundary of the wake. This part is set up in such a way that the wake can be modelled by other methods as long as the interface remains the same. The used model as well as the boundaries for possible extension are explained in section 2.3. Having defined the wake behaviour the attenuation matrix can be calculated using the method of Castles Castles and Leeuw (1953a). The method calculates a coefficient determining the effect of the upper rotors down wash in the wake at that specific position on the lower rotor. The induced velocity at the rotor's centre is the reference value at 1. A notable change is that the inflow for the lower rotor is no longer uniform as the influence is not uniform. The function description as well as the workout can be found in section 2.3.2. Other forces and moments that are present on the rotorcraft and how they are calculated can be found in appendix C. This is also the place where the used equations of motion are explained.

2.2   2 Dimensional Aerodynamics

2.2.1   Flapping Motion

This part will describe the methods and functions used to model the motion of the rotor-blades also called flapping motion. The first section will explain the usage of the flapping coefficients to describe the flapping motion. Also, the made choices are explained. Then there will be a description of the methods used to obtain these coefficients.

Flapping Coefficients

The flapping motion β is governed by the forces that act on the rotorblade. The most important are:

- Weight $g \cdot dm$

- Centrifugal $dm \cdot \Omega^2 r cos\beta$

- Aerodynamic dKa

- Pitch acceleration rotorcraft as a whole

- Roll acceleration rotorcraft as a whole

The flapping coefficients (a_0 a_1 b_1) are essentially the Fourier coefficients describing the motion of the blade. In this case, there are three coefficients. This is the shortest description of the series while still describing the flapping motion. They describe the flapping motion of the rotor blades and are, therefore, important for the calculation of the forces on these blades which in turn governs the motion. This is further explained in subsection

2.2.1. The forces are calculated using numerical integration. This means that the blades and rotor disk need to be discretized. The discretization is defined by two parameters. These are the radial distance on the blade and the rotational position of the blade in radians. The parameters are specified by a vector for the rotational position. It is defined by a start value, the step size and an end value. The same procedure is used to specify the radial vector. The result is shown in 2.2.

$$\psi = (0 : d\psi : 360) \cdot (\frac{\pi}{180}) \tag{2.1}$$

$$r = 0 : dR : R_{max} \tag{2.2}$$

The rotor blades are defined by a chord and a twist angle at the different radial position that were defined in 2.2. The aerofoil type is defined here as well. This is done by specifying where to find the database for this aerofoil. To be able to incorporate the attenuation matrix, it is necessary to detect this matrix as input. If not present, the user definition will be used. In this case, the definition of a non-dimensional inflow velocity Λ_0 is used. The induced velocity is made dimensional by multiplying with the rotors tip speed. This process is shown in equation 2.3.

$$v_i = \Lambda_0 \cdot (R \cdot \Omega) \tag{2.3}$$

If the attenuation matrix is present, the induced velocity is calculated using equation 2.5. The first step is to combine the inflow of the lower rotor Λ_0 and the upper rotor Λ_{i_u}. The inflow component from the upper rotor is determined by the attenuation matrix C_{att} which is explained in section 2.3.2.

$$\Lambda_i = \Lambda_0 + C_{att} \cdot \Lambda_{i_u} \tag{2.4}$$

$$v_i = \Lambda_i \cdot (R \cdot \Omega) \tag{2.5}$$

To be able to calculate the aerodynamic forces, the motion of the blades is a requirement. With an initial guess of the flapping coefficients the flapping angle can be solved as well as its first and second derivatives. This is done using the functions shown in equations 2.6 to 2.8.

$$\beta = a_0 - a_1 \cdot \cos(\psi) - b_1 \cdot \sin(\psi) \tag{2.6}$$

$$\dot{\beta} = a_1 \cdot \sin(\psi) - b_1 \cdot \cos(\psi) \tag{2.7}$$

$$\ddot{\beta} = a_1 \cdot \cos(\psi) + b_1 \cdot \sin(\psi) \tag{2.8}$$

Then the rotor hub behaviour can be set up. This is characterised by the non-rotation natural frequency of the rotorblade ω_{nr} and the Southwell coefficient α. The different types of rotorhead and the effects on the variables are shown in table 2.1.

Type	ω_{nr}	α
Central flapping hinges	0	1
Central flapping hinges with spring	$\frac{K_\beta}{I_\beta}$	1
Flapping hinges with offset	0	$1 + 3 \cdot e/2 \cdot (1 - e)$
Flapping hinges with offset and spring	$\frac{K_\beta}{I_\beta}$	$1 + 3 \cdot e/2 \cdot (1 - e)$
Flexible rotorblades	$12.37 \cdot (\frac{EI}{m \cdot R^4})$	1.188

Table 2.1: Rotor hub cases

To be able to use the aerodynamic look-up tables it is necessary to calculate the local conditions at the rotorblades. The general variables such as static (ambient) pressure, temperature and air density are assumed to be constant for the whole rotordisk. The angle of attack of the control plane can be calculated using the vertical and horizontal velocity components of the helicopter and the longitudinal control angle, leading to the function 2.9. At each position the control angle can be calculated using the combination of the collective and lateral- and longitudinal cyclic control inputs as is shown in equation 2.10. The inflow angle can be calculated using the velocity tangential and perpendicular to the blade as is shown in equation 2.11. The local angle of attack is now the difference between the control angle and the inflow angle and is calculated using equation 2.12. To be able to calculate these angles the local velocities have to be known.

$$\alpha_c = -\arctan(\frac{u}{w}) + \theta_{1s} \tag{2.9}$$

$$\theta = \theta_0 - \theta_{1c} \cdot \cos(\psi) - \theta_{1s} \cdot \sin(\psi) + \theta_{tw} \tag{2.10}$$

$$\phi = \arctan(\frac{U_T}{U_P}) \tag{2.11}$$

$$\alpha = \theta - \phi \tag{2.12}$$

These velocities are calculated by adding the different components responsible for relative motion at the blade element together. Equation 2.13 shows the calculation of the tangential velocity to the blade. It consists of *rotor rotation*, *forward translation*, *sideways translation* and the *yaw rate*. The velocity perpendicular tor the blade is calculated using equation 2.14. Here the components are *vertical translation*, *induced velocity and climb velocity*, *blade flap velocity*, *roll rate* and the *pitch rate*. The total velocity at the blade can then be calculated using Pythagoras as shown in equation 2.15.

$$U_T = (\Omega \cdot r) + (u \cdot \sin(\psi) + v \cdot \cos(\psi) + r \cdot r \tag{2.13}$$

$$U_P = -w + (v_i + C) + \dot{\beta} \cdot r - p \cdot r \cdot \sin(\psi) - q \cdot r \cdot \cos(\psi) \tag{2.14}$$

$$V_b = \sqrt{U_T^2 + U_P^2} \tag{2.15}$$

The control angle is dependent on the rotation direction. Taking this into account the equation shown in 2.10 becomes 2.16 for the counter clockwise rotation and 2.17 for the clockwise rotation. The twist angle of the blade is set-up as having a linear twist. To fit

the twist angle into the blade definition it is defined as a vector. The twist angle can be defined for each radial definition point of the rotor blade.

$$\theta(y, \Psi) = \theta_0 - \theta_{1c}\cos(\Psi) - \theta_{1s}\sin(\Psi) + \frac{\theta_{tw} \cdot y}{R} \tag{2.16}$$

$$\theta(y, \Psi) = \theta_0 + \theta_{1c}\cos(\Psi) - \theta_{1s}\sin(\Psi) + \theta_{tw}(i) \tag{2.17}$$

Two distinct methods of solving the flapping motion were explored. The first uses the lift curve slope $c_{l\alpha}$ to obtain the flapping coefficients as defined in Pavel (2001). The other is to use the equation of motion and an ODE solver to solve for the blade motion based on the equation of motion for a rotorblade as a function of time. These are presented in subsection 2.2.1 and 2.2.1 respectively.

Numerical approach

This method is the first that was implemented to solve the motion as is described by the flapping blades. It starts with the derivation of the forces on the rotorblade. Then by combining these forces already mention at the start of section 2.2.1 and using Newtons second law $\overrightarrow{F} = m \cdot \overrightarrow{a}$ the second order derivative can be formulated as 2.18.

$$F = m \cdot aM_a - \Omega^2 \cdot \beta = I \cdot \ddot{\beta} \tag{2.18}$$

Now assuming the rotorblade is made from a homogeneous material with the same properties. The function 2.18 can be integrated for a piece of the rotorblade Δr. Then it is rewritten to include the Southwell coefficient α as well as the eigen frequency ω_{nr}, used to describe the rotor hub behaviour thus obtaining equation 2.19.

$$\ddot{\beta} + (\omega_{nr}^2 + \alpha\Omega^2)) \cdot \beta = \frac{M_a(\dot{\beta})}{I} \tag{2.19}$$

Equation 2.19 is the base formula, it can be extended by adding body rotations pitch and roll to increase the accuracy. The result is equation 2.20.

$$\dot{\beta} + (\omega_{nr}^2 + a\Omega^2) \cdot \beta + 2q\Omega\sin(\Psi) - 2p\Omega\sin(\Psi) = \frac{M_a}{I} \tag{2.20}$$

To solve the differential equation as is shown in equation 2.20 and/or 2.21, it was chosen to perform a variable substitution to obtain two (a system of) ordinary differential equations. This variable substitution is shown in 2.22.

$$\ddot{\beta} = ((\omega_{nr}^2 + \alpha \cdot \Omega^2) \cdot \beta - 2q\sin(\Psi) + \frac{M_a}{I} \tag{2.21}$$

$$x_1 = \beta \mid x_2 = \dot{\beta} \mid x_3 = \ddot{\beta} \tag{2.22}$$

The variable substitution as shown in equation 2.22 can be used to rewrite the differential equation 2.19. The result is a system of equations as shown in 2.23 and 2.24.

$$\frac{dx_1}{dt} = x_2 \tag{2.23}$$

$$\frac{dx_2}{dt} = -((\omega_{nr}^2 + \alpha \cdot \Omega^2) \cdot x_1 - 2q\sin(\Psi) + \frac{M_a}{I} \tag{2.24}$$

Using initial values for β and $\dot{\beta}$ the derivative of these variables $\dot{\beta}$ and $\ddot{\beta}$ can be calculated. This is done using equations 2.23 and 2.24 respectively. Using a numerical integration method the value for the next time step can be calculated. These next value can then be used to calculate the next derivatives, thus making a simulation of the motion possible. The simulation is set up with the ODE45 solver from matlab. The motion is described by functions 2.23 and 2.24. Together with a starting point $\beta, \dot{\beta}$ and a *running time* here the rotation angle (ψ) the position of the rotorblade can then be determined. The resulting motion is fitted to a Fourier series with three coefficients a_0, a_1, b_1. This is done to reduce the amount of data to be passed through to describe the solution.

Analytical approach

For the analytical part, the same analysis is made as for the differential part in section 2.2.1. This will result in the same base equation to describe the motion as shown in example 2.19. If the motion can be described by the form 2.19 the solution can be described by a truncated Fourier series as is described in equation 2.6.

To be able to calculate the flapping coefficients using the functions derived in Pavel (2001), a number of variable needs to be calculated or derived. The link between the different variables and parameters required to calculate these flapping coefficients is shown in figure 2.2. The most prominent are the non-dimensional natural frequency ω_b, the non-dimensional rotating natural frequency ν_b and the Lock number γ. To calculate these natural frequencies, the natural frequency and Southwell coefficient of the rotor configuration are a requirement. These values can be obtained using table 2.1 which only depends on the geometry of the rotor hub. Also, the rotational velocity Ω is an input. This leads to equations 2.25 and 2.26 for the static- and rotational natural frequencies respectively. To calculate the lock number the only variable still unknown is the lift curve slope. The density, blade radius and blade moment of inertia are already defined in the geometry definition. The lift curve slope $c_{l\alpha}$ is calculated for the 'whole rotordisk'. The lift curve slope is provided by the look-up table for the local blade flow. The local lift curve slopes are then averaged for the blade and then again for one rotation. When all sections of a blade are calculated the 'mean' value of the vector with the lift curve slope is calculated. When one rotation is finished calculating the mean value of all rotation angle is calculated. Thus, obtaining the lift curve slope of the rotor. The Lock number can then be calculated using equation 2.27.
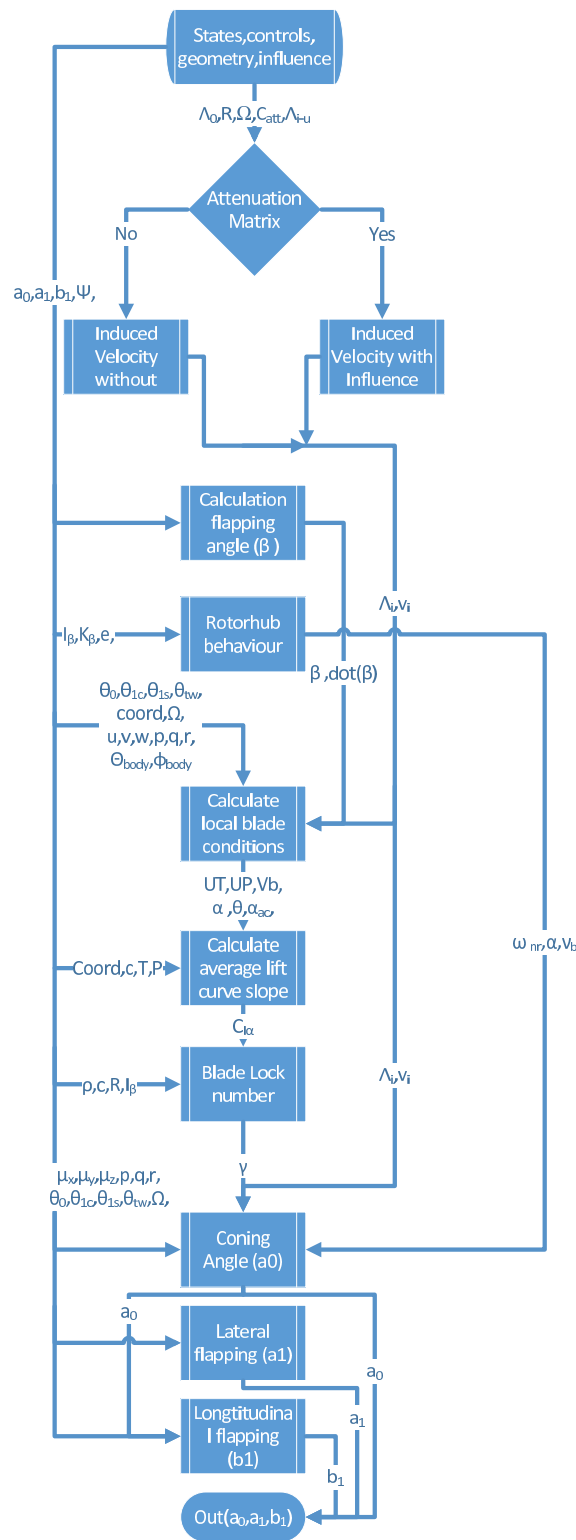
Figure 2.2: Workflow Diagram analytical flapping coefficients

$$\omega_b = \sqrt{\frac{\omega_{nr}}{\Omega}} \tag{2.25}$$

$$\nu_b = \sqrt{\alpha + \omega_b^2} \tag{2.26}$$

$$\gamma = \frac{\rho c_{la} \cdot c \cdot R^2}{I_b} \tag{2.27}$$

For the flapping angle β in 2.20, the truncated Fourier series is substituted. This is then used in combination with the non-dimensional natural frequency and the non-dimensional rotating natural frequency as is shown in 2.25 and 2.26. When this series is substituted the equations for the flapping coefficients $a0$, $a1$ and $b1$ can be obtained. These are shown in 2.28 to 2.30. The complete derivation can be found in Pavel (2001).

$$\begin{aligned}
a_0 = (&\frac{\gamma}{8}(1 + \mu_x^2 - 2 \cdot r/\Omega) \cdot \theta_0 - \frac{\gamma}{6}\mu_y \cdot \theta_{1c} - \frac{\gamma}{6}\mu_x \cdot \theta_{1s} + \\
&\frac{\gamma}{8}(4/5 - 8/5 \cdot r/\Omega + 2/3 \cdot \mu_x^2) \cdot \theta_{tw} - \frac{\gamma}{6} \cdot (-\mu_z + L_0) + \\
&\frac{\gamma}{12} \cdot \mu_x \cdot p/\Omega + \frac{\gamma}{12}\mu_y \cdot q/\Omega)/(\nu_b^2 - 2 \cdot r/\Omega)
\end{aligned} \tag{2.28}$$

$$\begin{aligned}
a_1 = (&\frac{\gamma}{6} \cdot \mu_y \cdot a_0 + \frac{\gamma}{3}\mu_x \cdot \theta_0 - \frac{\gamma}{8} \cdot \mu_x \cdot \mu_y \cdot \theta_{1c} - \\
&\frac{\gamma}{8} \cdot (1 - 2 \cdot r/\Omega + 3/2 \cdot \mu_x^2) \cdot \theta_{1s} + \frac{\gamma}{4} \cdot \mu_x \cdot \theta_{tw} - \\
&\frac{\gamma}{4}\mu_x \cdot (-\mu_z + L_0) + \frac{\gamma}{8} \cdot p/\Omega - 2 \cdot q/\Omega)/(1 - r/\Omega - \mu_x^2/2 + \mu_y^2/2)
\end{aligned} \tag{2.29}$$

$$\begin{aligned}
b_1 = (&-\frac{\gamma}{6}\mu_x \cdot a_0 + \frac{\gamma}{3}\mu_y \cdot \theta_0 - \frac{\gamma}{8} \cdot (1 - 2 \cdot r/\Omega + \mu_x^2/2) \cdot \theta_{1c} - \\
&\frac{\gamma}{8}\mu_x \cdot \mu_y \cdot \theta_{1s} + \frac{\gamma}{4} \cdot \mu_y \cdot \theta_{tw} - \frac{\gamma}{8} \cdot \mu_y \cdot (-\mu_z + L_0) + 2 \cdot p/\Omega + \\
&\frac{\gamma}{8} \cdot q/\Omega)/(-1 + r/\Omega - \mu_x^2/2 + \mu_y^2/2)
\end{aligned} \tag{2.30}$$

The new flapping coefficients calculated by equations 2.28 to 2.30 can then be used to calculate the forces on the rotorblades. The next section 2.2.2 will describe the process of the relating the local flow conditions to the acting forces and motion.

2.2.2 Aerodynamics

The aerodynamic modelling, is set up around the aerofoil. Thus, the aerofoil section is the base and its modelling is further explained in subsection 2.2.2. Then, using these sections the forces around a single blade element can be calculated. This is done using the conventional mechanics equations. These are further explained in subsection 2.2.2. Having calculated all elements of the blade, the forces and moments of the elements can be combined for a single blade. This process is explained in subsection 2.2.2.

Section

For a section, the aerodynamic forces are determined by looking up the lift, drag and
moment coefficients from a look-up table. The indices for the look-up table were chosen to
be the local Reynolds number, the Mach number and the angle of attack. This choice was
made because with this combination of parameters describes the situation of the aerofoil
section completely. The data that are provided by the model are the local velocities,
local angle of attack, the blade geometry and the static pressure and temperature. This
means that to be able to use the look-up table, the Reynolds- and Mach number have
to be calculated first. This is done by calculating the density of air using equation 2.31.
The dynamic viscosity also has to be calculated. The dynamic viscosity also needs to be
calculated. For this Sutherland's formula for an ideal gas as shown in equation 2.39 is
used.

$$\rho = \frac{p}{R \cdot T} \tag{2.31}$$

The density can also be calculated for air with moisture present. For this the partial gas
pressure is used, which is calculated from the relative humidity. The functions and values
used for the calculation are shown in equations 2.32 to 2.38.

$$\rho_{ha} = \frac{P_d}{R_d \cdot T} + \frac{P_v}{R_v \cdot T} \tag{2.32}$$

$$\rho_v = \Phi \cdot P_{sat} \tag{2.33}$$

$$P_d = P - P_v \tag{2.34}$$

$$R_d = 287.058 \tag{2.35}$$

$$R_v = 461.495 \tag{2.36}$$

$$\Phi = rel.hum.[\%] \tag{2.37}$$

$$P_{sat} = 6.1078 \cdot 10^{\frac{7.5T}{T+237.3}} \tag{2.38}$$

For the calculation of the dynamic viscosity, the reference viscosity is $\mu_0 = 18.27[\mu Pas]$ at
a reference temperature of $T_0 = 291.15[K]$. The Sutherland's constant $C = 120[K]$ for the
gaseous material is used. For the function to be valid the main variable, the temperature
T, has to be between $0 - 555[K]$ When the static pressure is below $3.45[MPa]$, the error
due to pressure remains below 10 %.

$$\mu = \mu_0 \cdot \left(\frac{(T_0 + C)}{(T + C)}\right) \cdot \left(\frac{T}{T_0}\right)^{3/2} \tag{2.39}$$

Now using the density in 2.31 and the dynamic viscosity in 2.39 the kinematic viscosity
can be calculated. The used function is shown in equation 2.40.

$$\nu = \frac{\mu}{\rho} \tag{2.40}$$

Then the Reynolds number can be calculated as is shown in equation 2.41. Here, the V is the local speed at each section respectively, the local chord c is also set up for each section. The kinematic viscosity is calculated for a uniform temperature and pressure, although the programming is prepared to be used with variations per section.

$$Re = \frac{V \cdot c}{\nu} \tag{2.41}$$

The next variable used for the look-up tables is the Mach number. For this the speed of sound is calculated as is shown in equation 2.42. As with the viscosity the speed of sound is assumed to be a single value for the whole rotor disc.

$$a = \sqrt{\gamma RT} \tag{2.42}$$

The velocity at each blade section can be divided into two parts. A velocity perpendicular to the blade and another tangential to the blade as are shown in figure 2.3.
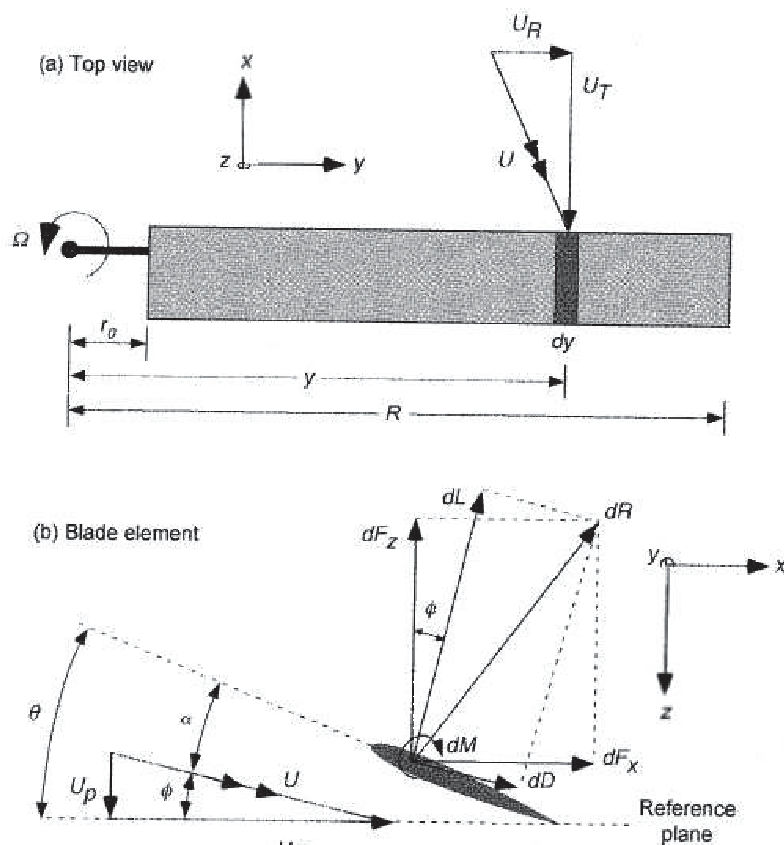

Figure 2.3: Velocity definition with respect to the Rotor Campfens (2008)

The velocity calculation is started with the analysis of the hovering flight. When the rotorcraft has no translational velocity the tangential velocity of the blade can be simply expressed as the rotational velocity of the blade as is shown in equation 2.44. The velocity

perpendicular to the blade is the sum of the induced velocity v_i and the flapping motion $\dot{\beta}$ times the local radius r and is shown in equation 2.43.

$$U_P = v_i + \dot{\beta}r \tag{2.43}$$
$$U_T = \Omega r \tag{2.44}$$

The blade velocities for hovering flight can then be extended for forward flight by transforming the translational velocity V from the body frame of reference to the blade reference frame as can be seen in figure 2.4.
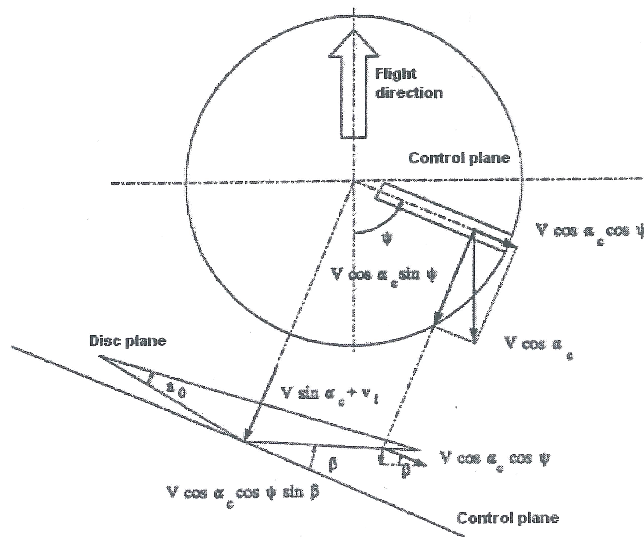
Figure 2.4: Velocity conversion from the body reference frame to the rotor reference frame (van Holten & Melkert, 2002)

The velocity seen by the blade depends on two angles the first is to the azimuth position ψ on the rotor disk the second is the angle of attack of the control plane itself α_c. The angle of attack for the control plane can be calculated using the forward velocity and the downward component as can be seen in equation 2.45.

$$\alpha_c = \arctan(\frac{u}{w}) + \theta_{1s} \tag{2.45}$$

The relation for the velocity is further extended by incorporating the body rotation rate q for the symmetric body movement. Adding all these effects to the basic relations in equations 2.43 and 2.44 leads to 2.46 and 2.47.

$$U_P = V\sin(\alpha_c) + v_i + \dot{\beta}r - qr\cos(\Psi) + V \cdot \sin(\beta) \cdot \cos(\alpha_c) \cdot \cos(\Psi) \tag{2.46}$$
$$U_T = \Omega r + V\cos(\alpha_c) \cdot \sin(\Psi) \tag{2.47}$$

The next step was to incorporate the asymmetric body movements v, roll and yaw rates. Because of simplicity the transformation of the velocity V to the components in the control

plane are already written as u,v or w in the equations. The tangential velocity can be extended with the effects as described above. In equation 2.48 the information provided by these extra variables is added. The size of the velocities perpendicular to the blade is influenced by the flapping angle. This influence is already seen in 2.46 for the forward velocity u, the same influence applies to the lateral velocity v. The geometry to calculate these relations can be seen in figures 2.4 and 2.9. Performing the same extension for the velocity perpendicular to the blade results in equation 2.49.

$$U_T = \Omega \cdot R + u\sin(\psi) + v \cdot \cos(\psi) + r \cdot R \tag{2.48}$$

$$U_P = -w + (v_i + C) + \dot{\beta} \cdot R - p \cdot R \cdot \sin(\psi) - q \cdot R \cdot \cos(\psi) + u\sin(\beta) \cdot \cos(\psi) + v \cdot \sin(\beta) \cdot \sin(\psi) \tag{2.49}$$

$$V_b = \sqrt{U_T^2 + U_P^2} \tag{2.50}$$

The last step is to calculate the total velocity seen by the aerofoil section on the element. This is calculated using Pythagoras and is shown in equation 2.50. The total velocity at the blade sections is then using the speed of sound transformed to the corresponding Mach number, as is shown in equation 2.51.

$$M = \frac{V}{a} \tag{2.51}$$
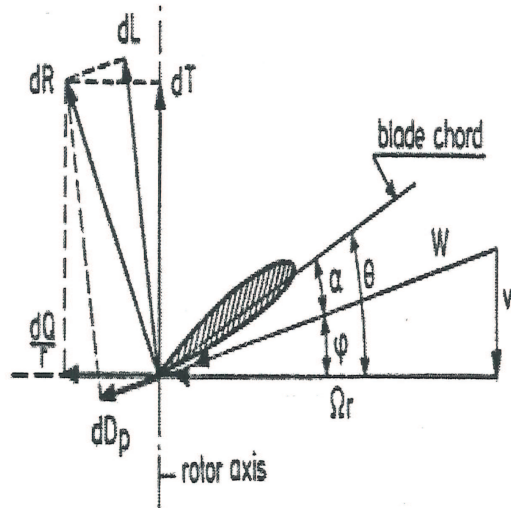
Figure 2.5: Angle of Attack as observed by the Bladevan Holten and Melkert (2002)

Now the last input for the look-up tables is the angle of attack which is an input value for the section calculations. The angle of attack for the blade locally is the difference between the control angle θ and the inflow angle ϕ as shown in figure 2.5.

$$\alpha = \theta - \phi \tag{2.52}$$

This lead to equation 2.52. The control angle can be specified as being the sum of all control contributions. Using the velocity tangential and perpendicular to the local section the inflow angle can be calculated. The base of the database is a 3-dimensional database with the Mach number, the Reynolds number and the angle of attack as index values. The lift curve slope is either looked up from the database or it can be calculated from the lift and angle of attack data. For the lift curve slope calculation there has to be an edge detection. This is because the calculation, which is shown in equation 2.53 can only be performed if the index of the angle of attack is not at an extreme. In case it is at the minimum all those indices are set to $i + 1$ and if the index is at its maximum the indices are set to $i - 1$.

$$C_{l\alpha} = \frac{C_L(\alpha_{i-1}) - C_L(\alpha_{i+1})}{\alpha(\alpha_{i-1}) - \alpha(\alpha_{i+1})} \quad (2.53)$$

Due to the difficulty of obtaining complete aerodynamic data, a detection was added to determine if the values presented for look-up are within a safe distance of the database points, if this is not the case a warning message will be displayed. The aerodynamic look-up table was constructed using different data origins for a two dimensional aerofoil. The methods used were converting windtunnel data and using data generated by calculation routines like '2D panel method' Drela (2015). This was done to obtain the required aero-dynamic data. The most important being the lift coefficient C_l and the drag coefficient C_d. The drag coefficients found were: pressure drag coefficient C_{Dp}, profile drag $C_{d,profile}$ and friction drag $C_{d,f}$. This aerofoil data was tried to be obtained from published wind-tunnel data for both the NACA 0012 and the NACA 23012 aerofoils. Most of the results found were either course, having large gaps in the data or were limited, describing only a small part of the angle of attack or Reynolds number range of interest. Despite these set backs eventually one data set was found Critzos, Heyson, and Boswinkle (1955). In figure 2.6 the lift and drag coefficients change with angle of attack are plotted for a number of Reynolds numbers.

Due to the difficulties finding a windtunnel database an implementation of a 2D panel method was implemented. This was found in the x-foil code, despite its limits, to construct a database to be able to test the model. Using this code it was observed that although easy to use on different aerofoils. The aerodynamic degradation is not accurately predicted. The method gives, however, the possibly to use the reverse functions to calculate aerofoil from desired pressure distributions.

Element

The elements are modelled by dividing the rotor blade in to pieces each piece will have two edges (sections) and here the aerodynamics is calculated/looked-up. This process is described in subsection 2.2.2 results in the lift, drag and moment coefficient at each section/edge of the elements. Now using the lift and drag coefficients specified by the look-up table the force per unit span (l, d) can be calculated using 2.54 for the lift and 2.55 for the drag.
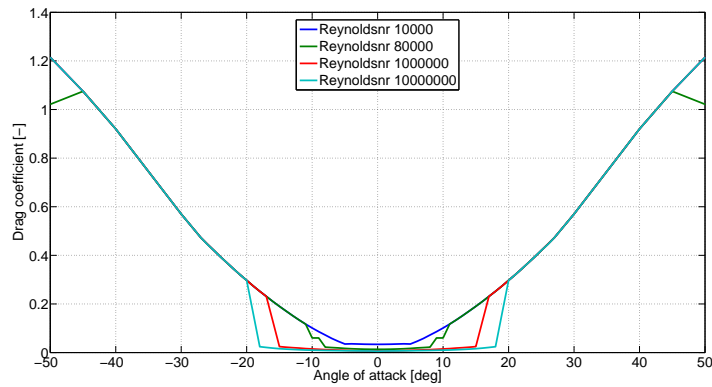
(a) Drag coefficients
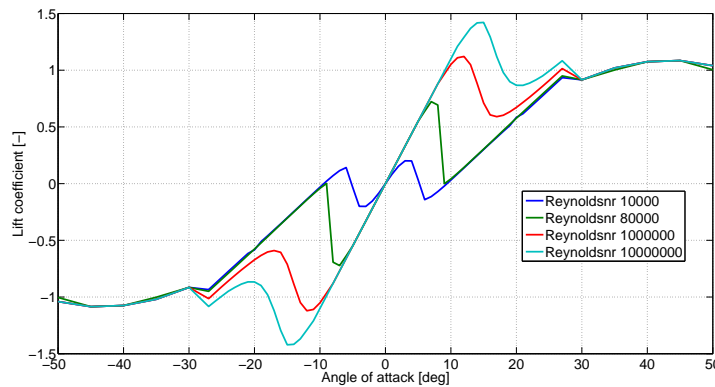
(b) Lift coefficients

Figure 2.6: Force coefficients for different Reynolds numbers vs. angel of attack

$$dl = \frac{1}{2}\rho V^2 C_l \cdot c \tag{2.54}$$

$$dd_p = \frac{1}{2}\rho V^2 C_{d_p} \cdot c \tag{2.55}$$

Due to the changing conditions for each element. The forces calculated in 2.54 and 2.55 differ. The forces for a section can be obtained by integration. Due to the discretization made for the rotorblade some form of approximation needs to be implemented. Three methods of approximation are implemented, the first is by rectangular blocks, the second is by trapezoidal and finally the Simpsons rule of integration is implemented to integrate the forces to an element. A detailed description of the implementation of these methods can be found in appendix C.

Blade

The forces as calculated for the elements, using the methods described in subsection 2.2.2 can be put together into a table and plotted to see how the rotor blades is loaded at that

specific time of which an example is shown in figure 2.7. The forces as shown are the
result of the rotor force calculations in the modular reference model. To check the input
values to the rotor force calculation as well as the looked-up lift and drag. The forces
shown are for a trimmed flight with a forward velocity of 108 km/h. The input values
are checked by plotting the absolute velocity as seen by the blade V_b and the local angle
of attack seen by the blade element α. In 2.7a it can be observed that the velocity profile
for forward 0° and rear 180° are the same as is expected in pure forward flight. Also,
the difference between the advancing blade and the retreating blade are clearly shown
difference between 90° and 270° respectively. With for the retreating blade an initial
decrease in velocity. The output of the aerodynamics, lift and drag, are also plotted to
see the working of the look-up tables. The most lift is generated by the advancing side
as is shown in 2.7c at 90°. This is to be expected as is the least lift generation on the
retreating side 270°. What was not expected was that the blade generates more lift at
180° of the helicopter and not the same as at 360°. The drag can be seen to have a large
root contribution by the retreating blade 270°. Also, most of the drag produced by the
advancing blade is at the tip.

(a) Blade Velocity

(b) Angle of attack

(c) Lift

(d) Drag
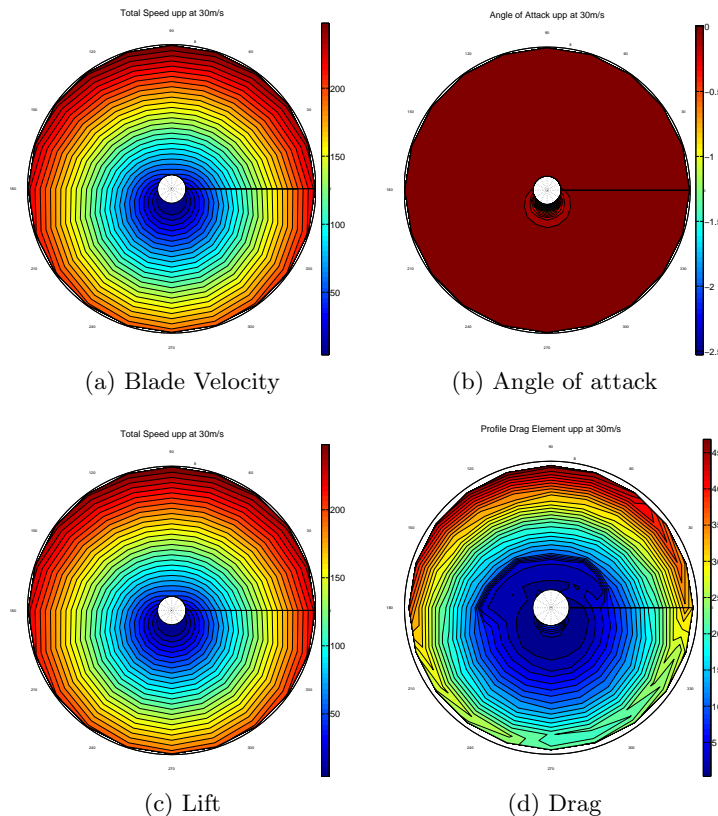
Figure 2.7: Blade Forces at different rotation stages

The process can be repeated for the next rotation angle with changed inflow conditions
and control angles as can be seen in figure 2.8. In this figure the results are shown are for
a forward velocity of 252 km/h in trimmed flight as calculated by the reference model,
for the lower rotor. The velocities at the different radial positions can be seen to variate
with the rotation angle. This is the case for all radial positions. Also, the 'reversed flow'

is indicated at the root and $1/4R$. The angle of attack confirms the behaviour shown by the velocity graph. The large angles at the root at 90° indicate the low tangential velocity with respect to the velocity perpendicular to the blade. The lift look-up with the input as shown yields an expected profile. This means the most lift being generated at the tip of the blade and by the advancing side. The drag contribution is largest at the root of the retreating side, this was also expected since the velocity is low and the angle of attack is high.

(a) Blade Velocity

(b) Angle of attack

(c) Lift

(d) Drag
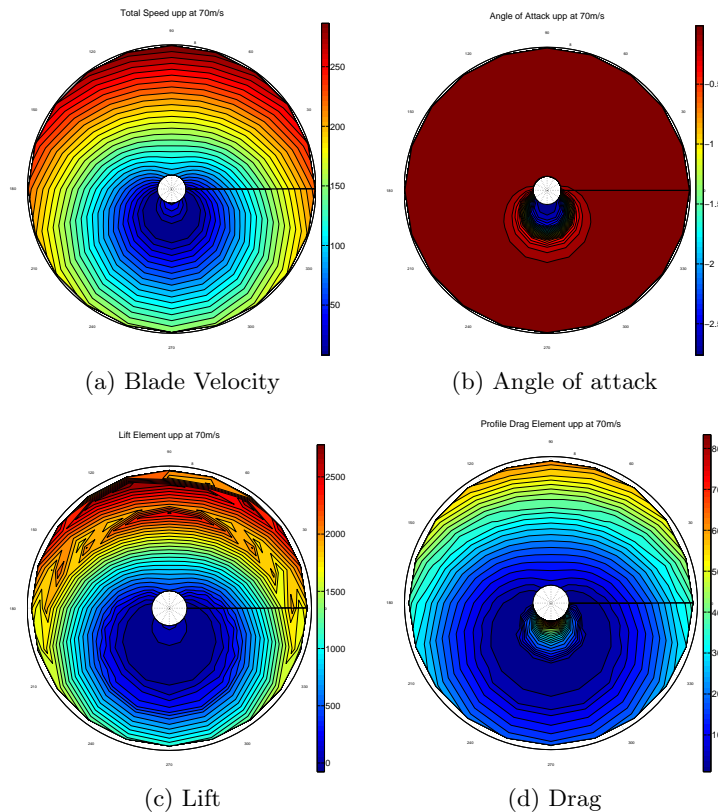
Figure 2.8: Condition change at blade tip

The calculations as shown here are valid for both the calculation of the flapping motion 2.2.1 as well as the rotor forces 2.2.3.

2.2.3 Rotordisk

The Rotordisk is the section where the forces and moments calculation are explained. The power calculations and coordinate transformations are also explained here. These calculations require an input describing the flapping motion of the blades as was described in section 2.2.1 as well as the lift and drag data as was described in section 2.2.2.

Forces

The lift and drag forces for each element needs to be transformed to: thrust, dH (longitudinal force), dS (lateral force) and torque. This transformation is performed using the

inflow angle (ϕ), the flapping angle (β) and the rotation angle (ψ).
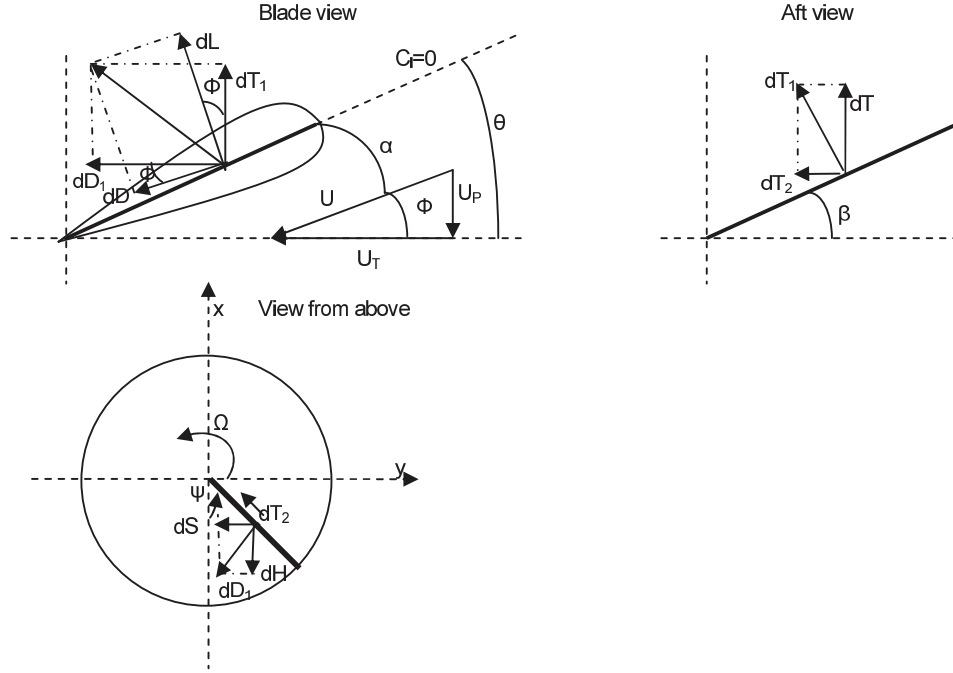
Figure 2.9: Forces on a blade element

The geometric foundation for the transformations can be seen in figure 2.9. Due to the inherent difference between the upper and lower rotor, the functions to calculate the transformations are different for both rotors. The relations for the upper rotor are explained first. The calculations start with transforming the forces from the lift dL and drag dD_p as are calculated in the aerodynamics section to the thrust dT_1 and drag dD_1. These relations are linked together by the inflow angle and lead to the relations 2.56 and 2.57.

$$dT_1 = d_L \cdot \cos(\phi) - dD_p \cdot \sin(\phi) \tag{2.56}$$
$$dD_1 = d_L \cdot \sin(\phi) + dD_p \cot \cos(\phi) \tag{2.57}$$

The forces thrust and drag are with respect to the blade orientation. This is then transformed to be with respect to the rotorhead using the local blade flapping angle β as shown in equations 2.58 and 2.59. The last one is also the thrust in the body reference system.

$$dT_2 = dT_1 \cdot \sin(\beta) \tag{2.58}$$
$$dT_u = dT_1 \cdot \cos(\beta) \tag{2.59}$$

The last part is to transform the drag and the drag part of thrust to the lateral and longitudinal forces on the rotor. The contribution of the drag and thrust to these forces

depends on the position of the blade, ψ the azimuth angle as is shown in figure 2.9. This angle is used to transform these forces. This leads to equation 2.60 for the longitudinal force and equation 2.61 for the lateral force. The last function 2.62 is to calculate the torque developed by the drag on the blades as is shown in equation 2.57.

$$dH_u = dD_1 \cdot \sin(\psi) - dT_2 \cdot \cos(\psi) \tag{2.60}$$
$$dS_u = dD_1 \cdot \cos(\psi) - dT_2 \cdot \sin(\psi) \tag{2.61}$$
$$dQ_u = R_L \cdot dD_1 \tag{2.62}$$

For the lower rotor the equations for the lateral and longitudinal forces are different due to the difference in rotation direction. The equations used for the lower rotor are shown in equation 2.63 and 2.64. Also, the torque calculation has to be changed because the drag direction changes to oppose the rotational direction, the result is shown in equation 2.65.

$$dH_l = dD_1 \cdot \sin(\psi) - dT_2 \cdot \cos(\psi) \tag{2.63}$$
$$dS_l = -dD_1 \cdot \cos(\psi) - dT_2 \cdot \sin(\psi) \tag{2.64}$$
$$dQ_l = -R_L \cdot dD_1 \tag{2.65}$$

Having transformed the forces from the rotorblades to the rotor head in equation 2.57 to 2.62. All the forces are in the same reference frame and can be integrated. Due to additional calculation requirement to keep track of the blade positions and the goal of evaluating the steady state performance. The choice was made to approximate the forces on the rotor by integrating the forces over one rotation (over the radius and azimuth angle). Then, taking the total force over one revolution divide it by the rotation angle ($2pi$) and multiply with the number of blades N_b. The results are shown in equations 2.66 to 2.68 for the forces up, forward and sideways which has a minus due to having to switch the right and left. The last function is the integration of the torque as shown in equation 2.69.

$$T = \frac{N_b}{2\pi} \int_0^{2\pi} \int_0^R dT \, dr \, d\psi \tag{2.66}$$

$$H = \frac{N_b}{2\pi} \int_0^{2\pi} \int_0^R dH \, dr \, d\psi \tag{2.67}$$

$$S = \frac{N_b}{2\pi} \int_0^{2\pi} \int_0^R -dS \, dr \, d\psi \tag{2.68}$$

$$Q = \frac{N_b}{2\pi} \int_0^{2\pi} \int_0^R dQ \, dr \, d\psi \tag{2.69}$$

These forces are then made dimensionless thus obtaining C_T, C_H, C_S and C_Q. The thrust coefficient obtained in this way is called the BEM thrust coefficient.Next is to calculate

the thrust coefficient using momentum theory, which is corrected using Glauert's method for forward flight. The angle of attack of the disk α_d has to be calculated for this thrust calculation. This done by subtracting the flapping angle a_1 from the angle of attack of the control plane α_c as can be seen in equation 2.70. For the base case the induced velocity specified in the input is a single value for the whole rotordisk. This will result in the fact that the induced velocity used in the calculation is also a single value. This is because the momentum is taken over the whole rotor area, if the induced velocity is not a single value the mean value for the corresponding area is taken. The thrust calculated using momentum and Glauert's method can then be formulated as is shown in equation 2.71. This thrust is then made non-dimensional in the same way as the thrust calculated using the BEM. This was shown in equation 2.72.

$$\alpha_d = \alpha_c - a_1 \tag{2.70}$$

$$T_{gl} = 2 \cdot \rho \cdot \pi \cdot R^2 \dot{v}_i \cdot \sqrt{(V \cdot \cos(\alpha_d))^2 + (V \cdot \sin(\alpha_d) + v_i)^2} \tag{2.71}$$

$$C_{Tgl} = \frac{T_{gl}}{dimless} \tag{2.72}$$

The momentum calculation can be extended to annular areas and even further into blade sections. To calculate the momentum per annulus the area of such a section has to be determined. The area for the complete disk is shown in equation 2.73. This can be refined by radial begin and end position. The result is the area for an annulus as is shown in equation 2.74. Also, a refinement can be made per section. This is done for a fraction of rotation of the rotor as is shown in equation 2.75. The area for a rotational section and a radial section can also be combined to get the area as shown in equation 2.76.

$$A = 2\pi \cdot R^2 \tag{2.73}$$

$$A = 2\pi \cdot (r_2^2 - r_1^2) \tag{2.74}$$

$$A = \frac{n}{360} \cdot \pi R^2 \tag{2.75}$$

$$A = \frac{\alpha_1}{360} \cdot \pi \cdot (r_2^2 - r_1^2) \tag{2.76}$$

Each of these areas can be inserted in the equation 2.77 to calculate the thrust according to the momentum method. The number of points where the thrust is calculated should be the same number as the induced velocity and the incoming velocity.

$$dT = 2 \cdot v_i \cdot \sqrt{(V \cdot \cos(\alpha_d))^2 + (V \cdot \sin(\alpha_d) + v_i)^2} \cdot \rho \cdot A \tag{2.77}$$

To be able to use the rotor forces for the rotorcraft model. The forces are transformed from the control reference frame to the shaft reference frame as is shown in figure 2.10. For this transformation the disk tilt in longitudinal direction θ_{1s} and lateral direction θ_{1c} are used to transform the forces into the X 2.78, Y 2.79 and Z 2.80 direction. Note that the thrust T is negative in Z as the zed direction is positive down and T is positive up.
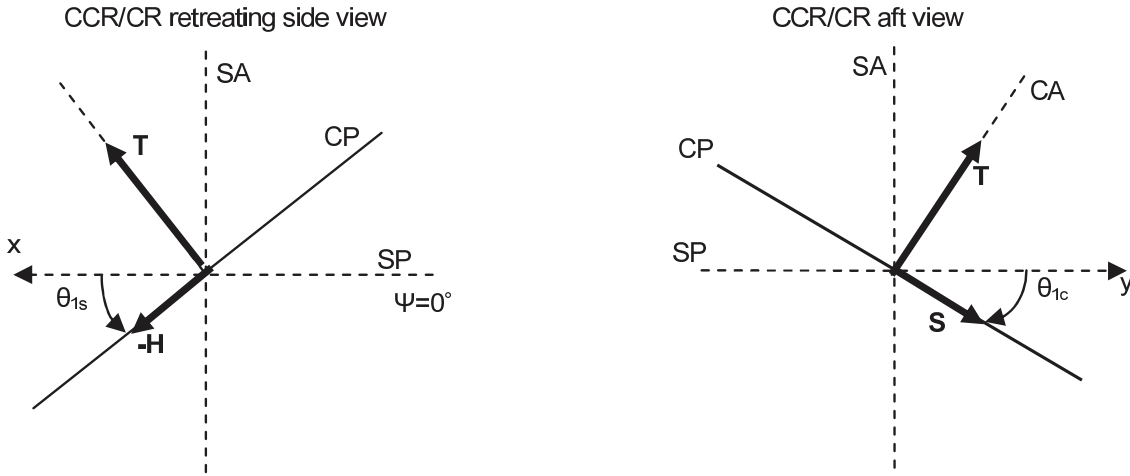
Figure 2.10: Relation between the Control Plane and the Shaft Plane

$$X = T \cdot \sin(\theta_{1s}) - H \cdot \cos(\theta_{1s}) \tag{2.78}$$

$$Y = T \cdot \sin(\theta_{1c}) - S \cdot \cos(\theta_{1c}) \tag{2.79}$$

$$Z = -T \cdot \cos(\theta_{1s}) \cdot \cos(\theta_{1c}) - H \cdot \sin(\theta_{1s}) + S \cdot \sin(\theta_{1c}) \tag{2.80}$$

The moments around the X 2.81, Y 2.82 and Z axes 2.83 are calculated using the forces and arms with respect to the base of the rotorhead. There is one exception this is N around the z-axis which requires no transformation and was calculated in equation 2.69.

$$L = Y \cdot z_h - Z \cdot y_h \tag{2.81}$$

$$M = -X \cdot z_h - Z \cdot x_h \tag{2.82}$$

$$N = Q \tag{2.83}$$

Power calculations

The total power requirement of the rotorcraft can be divided into a number of parts. The induced power is due to the tilt of the lift vector. Pressure and friction on the rotorblades both contribute to the drag power requirement. All parts in the flow that are not meant to produce a force contribute to the parasitic power requirement. The last part is the power requirement for the climbing flight. A summation of all these parts is shown in equation 2.84. For the rotordisk the main interest lies in the elaboration of the induced power and the drag power. Both are related to the working principle of the rotorblades. The parasitic power as well as the climb power can be approximated with the forces D_{par} and W multiplied with the velocity as is shown in equation 2.85.

$$P_t = P_i + P_p + P_d + P_{par} + P_c \tag{2.84}$$

$$P_t = kTv_i + P_p + H_0 V \cos(\alpha) + D_{par} V + WC \tag{2.85}$$

The power calculation for the rotor uses the same basic principle as for power calculation for the helicopter. The induced power requirement is based on the tilting of the lift or thrust vector. This tilt is caused by the velocity generated by the rotor. The thrust and the induced velocity for the rotordisk are known from the calculations performed by 2.66 and 2.3/2.5. The induced power can now be written as 2.86. Here the correction factor k is for non uniformity. Values normally lie between 1.1 and 1.2.

$$P_i = kTv_i \tag{2.86}$$

The drag power can be defined in multiple ways. The one shown in the combined equation 2.85 is using the H_0 force resisting the translational motion. In equation 2.87 the drag power requirement is also shown. It is based on the engine requirement to keep the rotor turning. Thus, the torque times the (rotational) velocity.

$$P_d = \Omega dQ = dL \sin(\phi) + dD_p \cos(\phi) \cdot \Omega r \tag{2.87}$$

The choice was made to use the drag power equations shown in 2.88 and the induced power equations shown in 2.89 to be implemented. The power requirement was calculated for each blade element separate. Comparing the power requirements of the single value calculation and the calculation per element turned out to have only a small difference.

$$dP_{dp} = dD_1 \cdot U_T \equiv dQ_u \cdot \Omega \tag{2.88}$$

$$dP_i = k \cdot dL \cdot v_i \equiv k \cdot dT_u \cdot v_i \tag{2.89}$$

The power requirement can be integrated over the rotorblades and azimuth angles just as was done with the forces. This results in equation 2.90 for the drag power and 3.5 for the induced power.

$$P_{dp} = \frac{N_b}{2\pi} \int_0^R \int_0^{2\pi} dD_{dp} d\psi dr \tag{2.90}$$

$$P_i = \frac{N_b}{2\pi} \int_0^R \int_0^{2\pi} dP_i d\psi dr \tag{2.91}$$

Tip- loss model

The tip-loss model implemented was developed by Prantl and Glauert in 1935. It is defined as a correction factor to the induced velocity field. The correction factor can be calculated using equation 2.92 as was found in Branlard (2011). The exponent f is calculated using equation 2.93.

$$F = \frac{2}{\pi} \cdot \arccos(e^{-f}) \tag{2.92}$$

$$f = \frac{B}{2} \cdot \frac{R - r}{r \cdot \sin(\phi)} \tag{2.93}$$

Requirements for this correction factor are the number of blades B, the total rotor radius as well as the local radius at the calculation station. Also, the local inflow angle ϕ is a requirement, leading finally to equation 2.93. The correction function is limited in use and has to adhere to the limit $C_T > 0.96 \cdot F$. For the rotor hub a similar set-up can be made as can be seen in 2.94. As limitation Branlard (2011) states that the tip loss corrections are less accurate when the number of blades is less than 3.

$$f = \frac{B}{2} \cdot \frac{r - R_{emb}}{r \cdot \sin(\phi)} \tag{2.94}$$

2.3   Rotor Interference

The wake modelling consists of two parts. The first is the determination of the contraction ratio as is shown in subsection 2.3.1. In subsection 2.3.2 the second part is shown. The calculation of the influence matrix is explained here.

2.3.1   Wake Contraction

The wake is modelled using a prescribed wake model. It describes the trajectory of the tip vortexes as proposed by Landgrebe (1971). The contraction ratio can be calculated from the position of the tip vortex. The process of these calculations is shown in figure 2.11.

It can be shown that both the axial z_{tip} and the radial y_{tip} coordinates as shown in figure 2.12 can be represented in an equation.

The radial coordinate can be represented by equation 2.95. For the axial coordinate two functions are required as there is a behaviour change after the next blade has passed. This effect can be observed by comparing the calculated results with test results. This is shown in figure 2.13.

$$\frac{y_{tip}}{R} = A + (1 - A)e^{-}(\Lambda \dot{\Psi}_w) \tag{2.95}$$
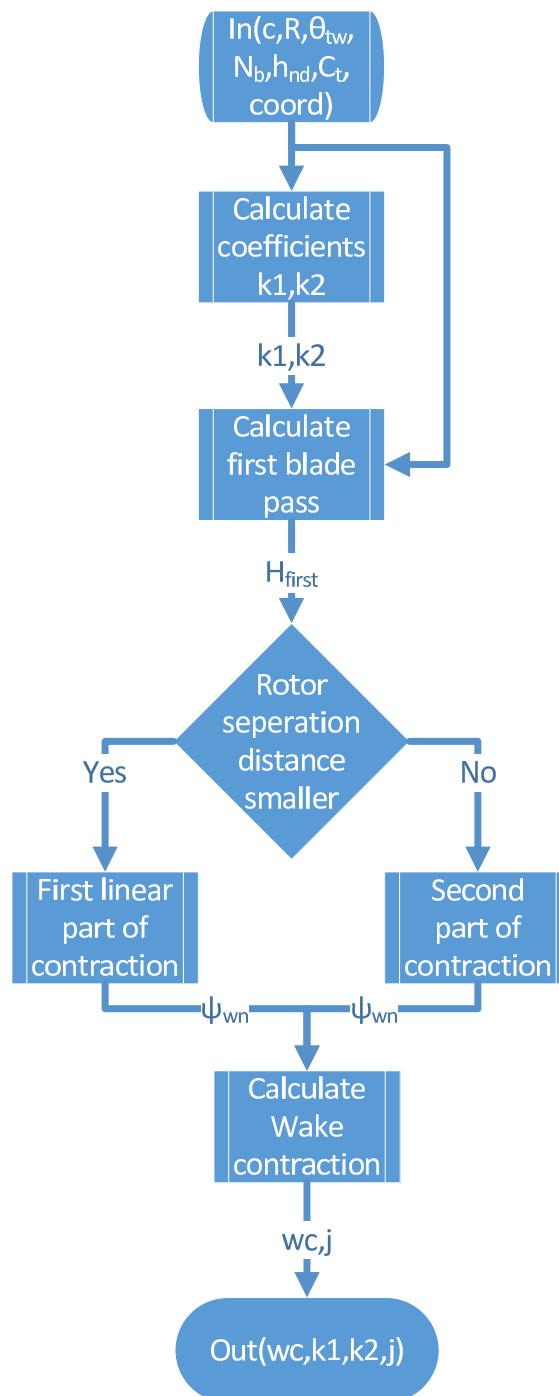
Figure 2.11: Flow diagram for the Wake contraction calculation

The axial distance can then be calculated using equation 2.96. When the next blade has passed equation 2.97 is used. The time of this blade passing is determined by the wake
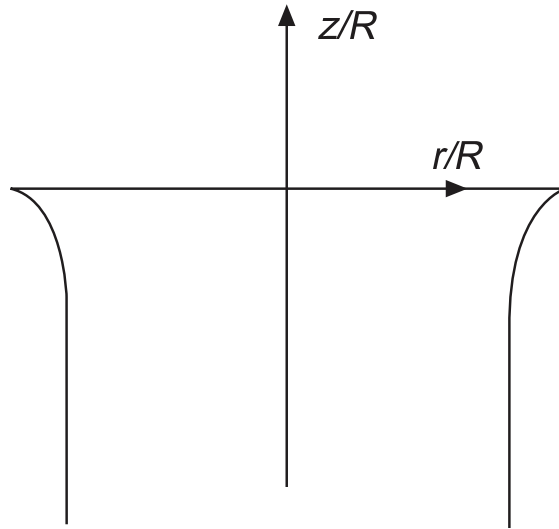
Figure 2.12: Wake Coordinates Bramwell (2001)
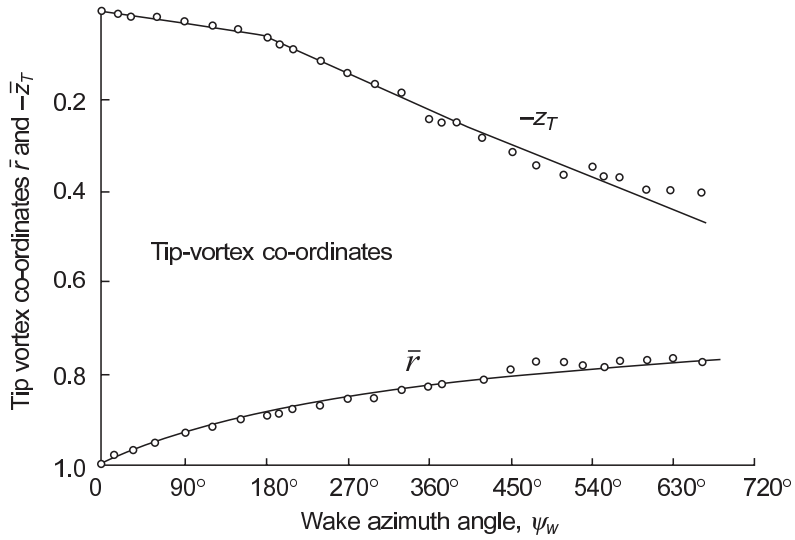
Figure 2.13: Tip Vortex Coordinates Bramwell (2001)

age Ψ_w.

$$\frac{z_{tip}}{R} = k_1 \cdot \Psi \quad for\ 0 \leq \Psi_w \leq \frac{2\pi}{N_b} \tag{2.96}$$

$$\frac{z_{tip}}{R} = (\frac{z_{tip}}{R})_{\Psi_w = \frac{2\pi}{N_b}} + k_2(\Psi_w - \frac{2\pi}{N_b})\ for\ \Psi_w \geq \frac{2\pi}{N_b} \tag{2.97}$$

The main value which determines the coordinates is the wake azimuth angle relative to the blade Ψ_w. Now the wake age has to be calculated to determine which function to use to describe the axial position of the vortex. Using the wake age of the transition point shown in 2.98, the vertical distance is calculated using equation 2.96. The result is equation 2.99.

$$\Psi_w = \frac{2\pi}{N_b} \tag{2.98}$$

$$H_{first} = K_1 \cdot \Psi_w \tag{2.99}$$

If the distance between the rotors is larger or equal to the separation distance shown in 2.99, equation 2.100 will determine the 'new' wake age. This is the wake age of the wake at the lower rotor. When this is not the case the new wake age is determined by equation 2.101.

$$\Psi_{wn} = \frac{h_{nd}}{K_1} \tag{2.100}$$

$$\Psi_{wn} = \frac{(h_{nd} - H_{first} + K_2 \cdot \frac{2\pi}{N_b})}{K_2} \tag{2.101}$$

To calculate the vortex positions using equations 2.95, 2.96 and 2.97 a number of coefficients are required. For the radial position two coefficients are used. These were determined empirically by Landgrebe (1971). One is a constant $A = 0.78$. The other can be calculated using equation 2.102. The only requirement for this is the thrust coefficient from the rotor that the wake is coming from.

$$\Lambda = 0.145 + 27 \cdot C_t \tag{2.102}$$

The axial position is calculated using two other coefficients. These coefficients $k1$ and $k2$ are determined from the same data in Landgrebe (1971). The result is equations 2.103 and 2.104. These coefficients are again dependent on the thrust coefficient of the rotor. Other variables required are the rotor solidity σ and the twist angle θ_{tw}.

$$k_1 = \frac{C_t}{\sigma} + 0.001 \cdot \theta_{tw} \cdot 0.25 \tag{2.103}$$

$$k_2 = -(1.41 + 0.0141 \cdot \theta_{tw} \cdot \sqrt{\frac{C_t}{2}} \tag{2.104}$$

The rotor solidity is calculated using the standard definition. It can be seen in equation 2.105.

$$\sigma = \frac{N_b \cdot c}{\pi \cdot R} \tag{2.105}$$

The required data from the model can now be described by a number of variables. For the rotor solidity these are: the number of blades N_b, the rotor chord length c and the rotor radius R. For the coefficients the thrust coefficient C_t and the rotor twist angel θ_{tw} are required. The last part is to calculate the wake contraction ratio. The contraction ratio is calculated using equation 2.107 and the wake age calculated by 2.100 or 2.101.

$$wc = A + (1 - A) \cdot e^{-(0.145 + 27 \cdot C_t \cdot \Psi_{wn})} \tag{2.106}$$

$$j = \frac{1}{wc} \tag{2.107}$$

2.3.2 Attenuation Coefficients

Having determined the contraction ratio the other aspect for the wake calculation is the influence of the down-wash. This effect is approximated by applying an attenuation value to the induced velocity. In this way an increased inflow inside the wake and a decrease outside the wake is obtained. The attenuation coefficients are calculated using a method developed by Castles and Leeuw (1953a). The general work flow for this method can be seen in figure 2.14. It uses the assumption that rotor wake vortex distribution consists of straight semi-infinite elliptic cylinder, which are formed by an infinite number of vortex rings lying in planes parallel to the Tip Path Plane.

Using this method the ratio of the normal component of the induced velocity with respect to the value at the centre of the disk can be calculated for each point r, ψ on the rotordisk. To calculate the attenuation coefficient first another angle needs to be defined. This is δ it is the azimuth angle of a wake vortex element measured from the negative x-direction as can be seen in figure 2.15 as ϕ.

For forward flight the wake is modelled as a straight skewed tube. The skew angle as shown in figure 2.16 is calculated according to equation 2.108. The non-dimensional velocities μ_x, μ_z and the induced velocity λ_i are used to perform this calculation.

$$\chi = \arctan\left(\frac{\mu_x}{-\mu_z + \lambda_i}\right) \tag{2.108}$$

The other parameters required for the calculation of the attenuation coefficient are the separation distance between the two rotors as well as the wakes contraction ratio. The wake geometry is defined by a radius y and azimuth angle Ψ. Using the variables and parameters as defined earlier the different parts A, B, C and D can be calculated. These relations are shown in equations 2.109 to 2.112.

$$A = \frac{1 + (y \cdot j) \cdot \cos(\Psi - \delta)}{R} \tag{2.109}$$

$$B = \frac{\tan(\chi) \cdot \cos(\delta)}{\sqrt{(1 + \tan(\chi))^2}} \tag{2.110}$$

$$C = 1 + \left(\frac{y \cdot j}{R}\right)^2 + \left(\frac{H}{R}\right)^2 + \frac{2 \cdot (y \cdot j) \cdot \cos(\Psi - \delta)}{R} \tag{2.111}$$

$$D = \left(\frac{H}{R}\right) + \frac{y \cdot j}{R} \cdot \tan(\chi) \cdot \cos(\Psi) + \frac{\tan(\chi) \cdot \cos(\delta)}{\sqrt{1 + \tan(\chi)^2}} \tag{2.112}$$

These parts can be combined into a function for the influence of one vortex ring at one point dV as is shown in equation 2.113. When this is integrated over the full circle of the
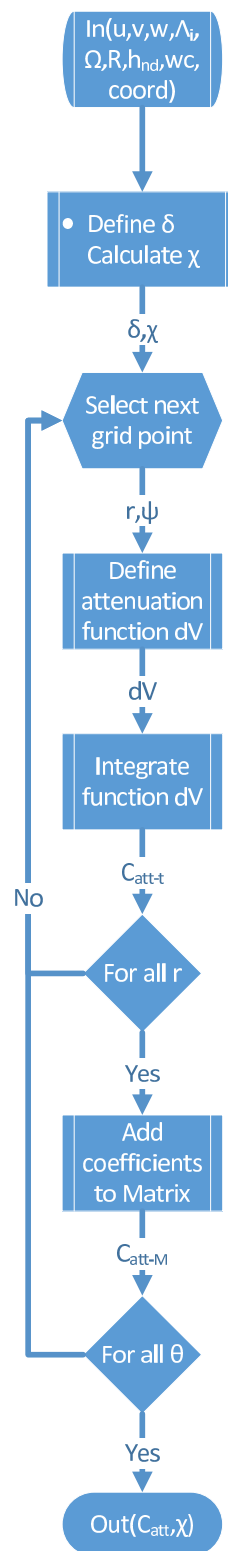
Figure 2.14: Workflow diagram for the Attenuation coefficients
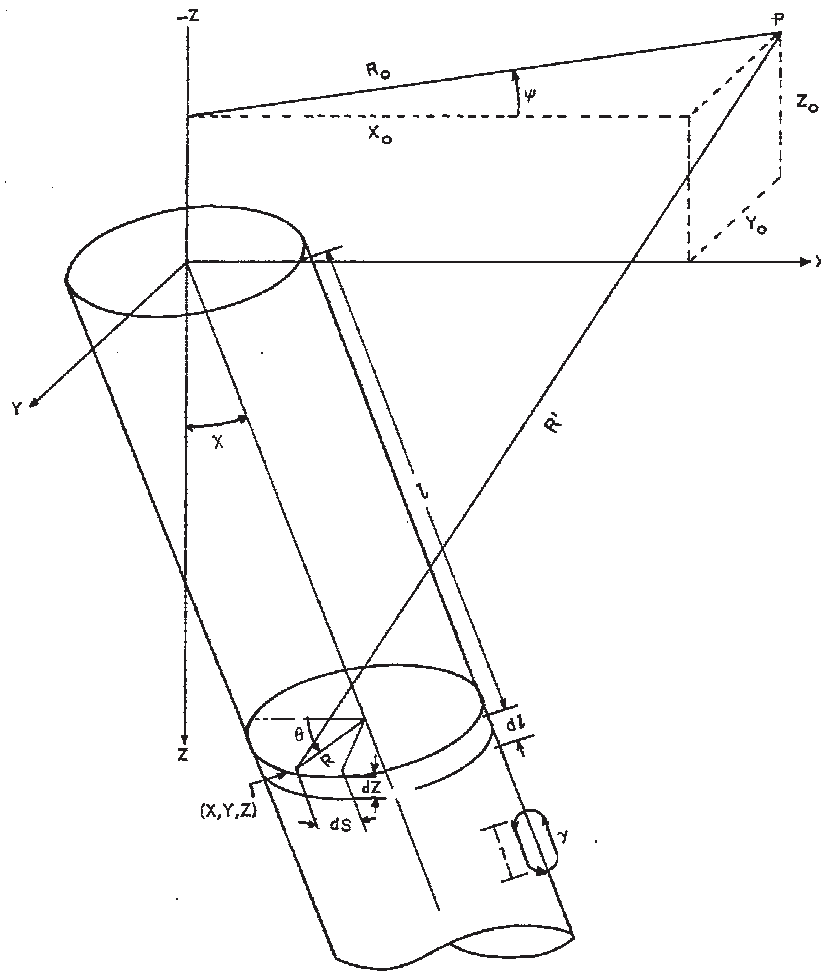
Figure 2.15: Angle definition for the attenuation calculation Castles and Leeuw (1953a)

angle δ as is shown in equation 2.114 the contribution of all vortex rings are incorporated. The result is the influence factor C_{att} at a specific point. This process is repeated for the whole rotor disk. The result is a matrix with attenuation coefficients.

$$dV = \frac{1}{2\pi} \cdot \frac{A - B \cdot \sqrt{C}}{\sqrt{C} \cdot \sqrt{C - D}} \tag{2.113}$$

$$C_{att} = \int_0^{2\pi} dV \, d\delta \tag{2.114}$$
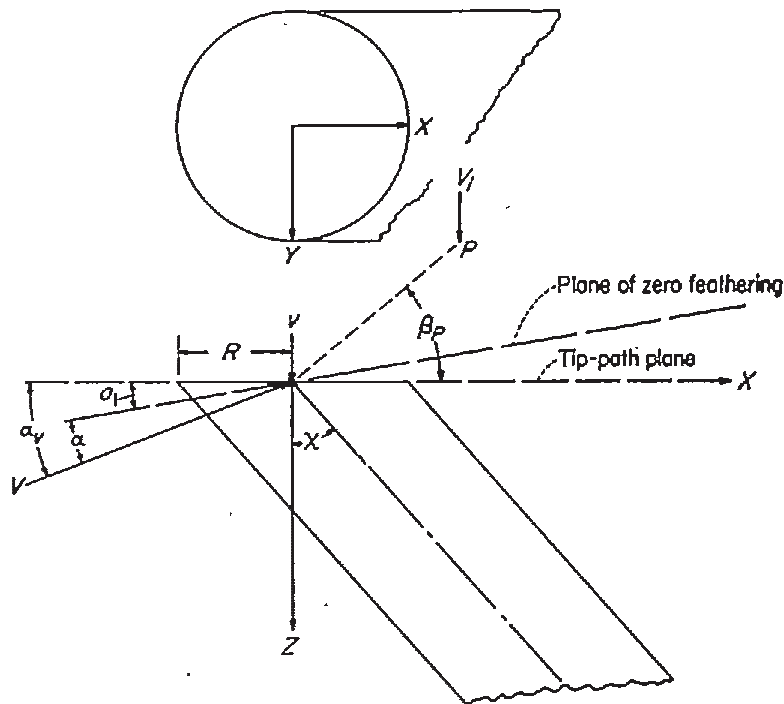
Figure 2.16: Skew angle definition for use by the attenuation coefficients Castles and
Durham (1956)

2.4   Trimmed Flight

In this section the method used to obtain a trimmed flight condition is described. The
definition of the objective function used to define the trimmed flight condition will be
explained. Also, the implementation of the method to use the objective function will be
described.

2.4.1   States & Controls

To be able to start the trim process an initial guess for the variables is required. This
is the starting point. The starting point is a complete state vector as can be seen in
2.115. This state vector is used as input for the model. Then the model calculates the
time derivative for each of the state variables in the input vector. This makes it possible
to find a steady state. The control vector as shown in 2.116 defines the controls for the
model. They consist of the rotorcraft body angles the collective and cyclic control angles.
The last two variables are the non-dimensional induced velocities, these are added to be
able to use a quasi steady inflow for the BEMT.

$$\begin{pmatrix} u & v & w & p & q & r & \psi & \theta & \phi & x & y & z & \Lambda_{0u} & \Lambda_{0l} \end{pmatrix} \tag{2.115}$$

$$\begin{pmatrix} \theta & \phi & \theta_{0u} & \theta_{0l} & \theta_{1s} & \theta_{1c} & \Lambda_{0u} & \Lambda_{0l} \end{pmatrix} \tag{2.116}$$

The trim variables are used to calculate the objective function, which is explained in subsection 2.4.2. In the course of the search a number of solvers was used to find a trimmed flight solution. The first method to be explained is the Newton iteration method. It is described in subsection 2.5. Due to the fact that this method doesn't always provides a solution. The exhaustive sweep calculations as solving method was also used. It will be explained in section 2.6. The native Matlab methods used are finally explained in appendix C.

2.4.2   Objective function(s)

The main purpose of the objective function is to use the relation between the trim variables 2.116 and the output from the model, the accelerations, to describe the quality of the current point as a solution for trimmed flight. In other words, the problem definition using a mathematical description. The objective value is determined from the output of the model. The states have to be constant for the trim case, except the velocities in the earth inertial reference frame. These values can be defined as the rate change of the states as is shown in vector 2.117. The angular velocities being zero also means the time derivatives of the attitude angles is zero. When the last two variables λ_{0u} and λ_{0l} are constant, it indicates that there is no transient behaviour in the non-dimensional inflow velocity. This means that the rotor is operating at a steady state.

$$f = [\dot{u} \ \dot{v} \ \dot{w} \ \dot{p} \ \dot{q} \ \dot{r} \ \dot{\lambda}_{0u} \ \dot{\lambda}_{0l}] \tag{2.117}$$

The objective is to make all values in the objective vector 2.117 zero. This means that all velocities are constant and the accelerations are zero, when this is the case there is a steady state. Some solvers require a single objective value. The single objective value is defined as the maximum of the absolute value of each entry of the objective vector. This objective vector can also be extended to include a gradient value. The gradient is calculated with respect to the control inputs. It is defined as df/dx with respect to a single control input. The resulting gradient is included in the output of the objective function. This gradient is calculated using a small step size δ, the controls used to calculate the objective vector are then one by one perturbed by this small step. The result is a new objective vector. The sensitivity to the change can then be calculated using equation 2.118. This process is repeated for all control inputs as shown in 2.116 and the results can be compiled into a Jacobian matrix as shown in 2.119.

$$df = \frac{f_{new} - f}{\delta} \tag{2.118}$$

$$\frac{df}{dx} = [df(1) \cdots df(i) \cdots df(8)] \tag{2.119}$$

2.5   Newton iteration Method

The Newton iteration method is essentially the same solver written by Campfens (2008) for his model. It has been adapted to be used with the new model. The main changes are the separation of the method from the model. This includes providing the corresponding input and output to and from the model. Figure 2.17 shows the work flow to find a trimmed flight solution using the Newton iteration method.
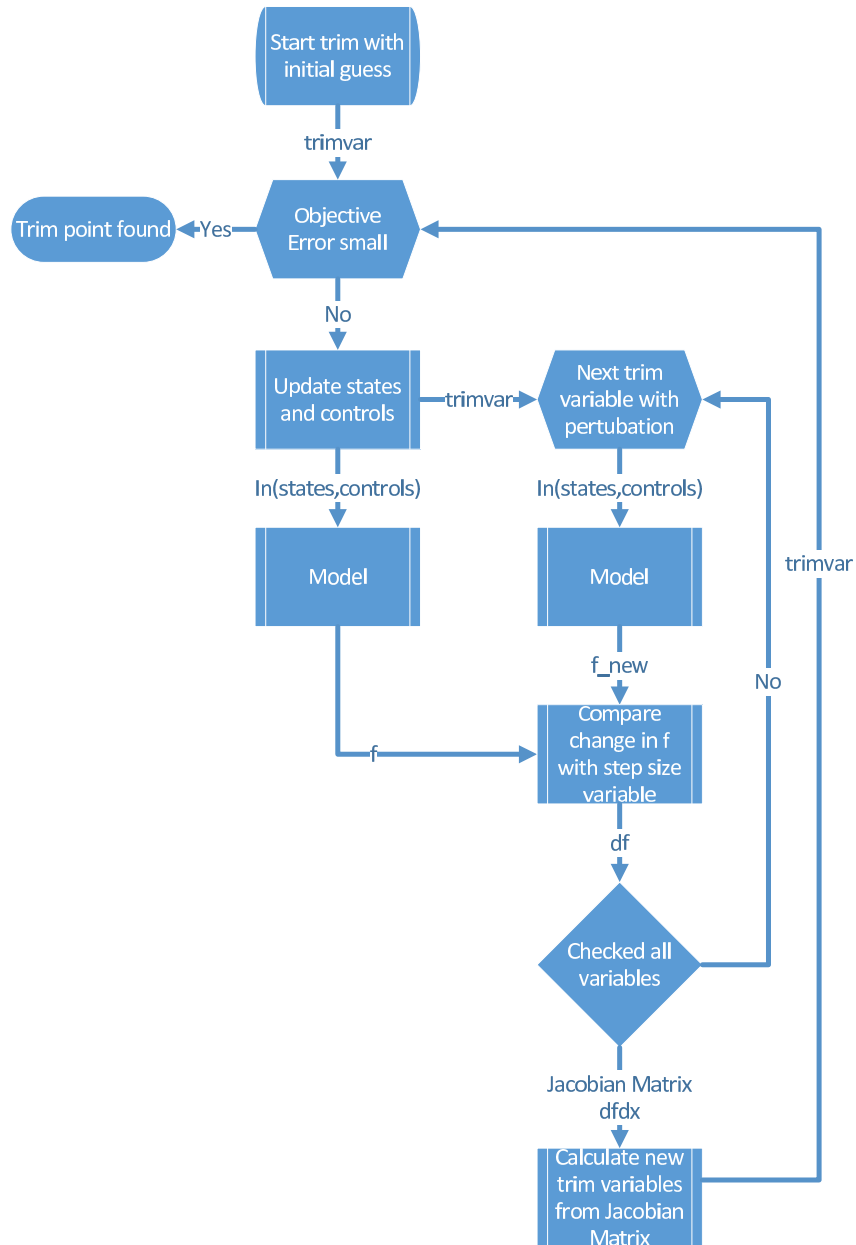
Figure 2.17: Workflow diagram Newton Iteration Method Solver

The trim process uses the gradient calculated from the trim variables using a perturbation vector. This is essentially the same procedure as is explained in section 2.4.2. The states

and controls are given to the model as input. The output is the rate change of the states called f. In the trim condition the vector f consists of only zeros. The control values can then be saved as the old *trim variables* (X). Then the Jacobian matrix $[\frac{df}{dx}]$ is calculated using the previous defined step change for the trim variables. It will have the same length as the trim variables and describes the changes in the objective vector (f) with respect to the control inputs. The new trim variables can be calculated using the inverse of the Jacobian matrix and the initial trim-variables. This is shown in equation 2.121

$$\Delta X = -[\frac{df}{dx}]^{-1} \cdot f \tag{2.120}$$

$$X_{new} = \Delta X + X \tag{2.121}$$

The new trim-variables can then be used to calculate the objective function to evaluate the quality of the solution. The next iteration can then be started using the new trim-variables as the start. This is process is repeated until the objective value is sufficiently small $1e^{-1}$. When this is the case the solution is accepted as a trimmed result and the states and controls are saved. The corresponding results from the trim calculations are shown in chapter 3.

2.6   Controls Sweep Method

Using the Newton Iteration method as described in section 2.5 was unfortunately unsuccessful for the Micro aerial Vehicle (MAV). Using the same objective function several Matlab methods were tried to find a suitable trim point. The main methods that were used are described in appendix C.4. Since the cause of the inability to find a trim point was unknown, the choice was made to visualize the solution space. This was done by looking at the forces and moments with changing controls settings. This solution method is called a sweep calculation.

The term sweep was chosen because it means "movement to search an area". In this case, for a solution. The sweep method can be used to search a range of input values for a trim solution. At the same time, the relation between the controls and the forces can be visualized. The term sweep also indicated a range to indicate the extent of possibilities. This applies to the method as it is used to assess a large range of possible control inputs.

Just as with the Newton Iteration method the Sweep method requires an initial guess for the states and controls. The first part as shown in figure 2.18 is solving the Collective control angles. This is achieved by varying the control angles for the upper and lower rotors and plotting the corresponding difference between the thrust and the weight.

The resulting plot showed a field which varied from the weight of the rotorcraft at the minimum setting for both angles to the maximum thrust value when both collective angles are at there maximum. This process is then repeated for the yawing moment. The results can be plotted to show the relation between the differential collective angle and the yawing moment. For a trimmed flight condition the thrust has to equal the weight. Also, the yawing moment from the upper rotor has to be equal to the yawing moment from the lower rotor. These conditions give two lines, One were the combination of controls has no
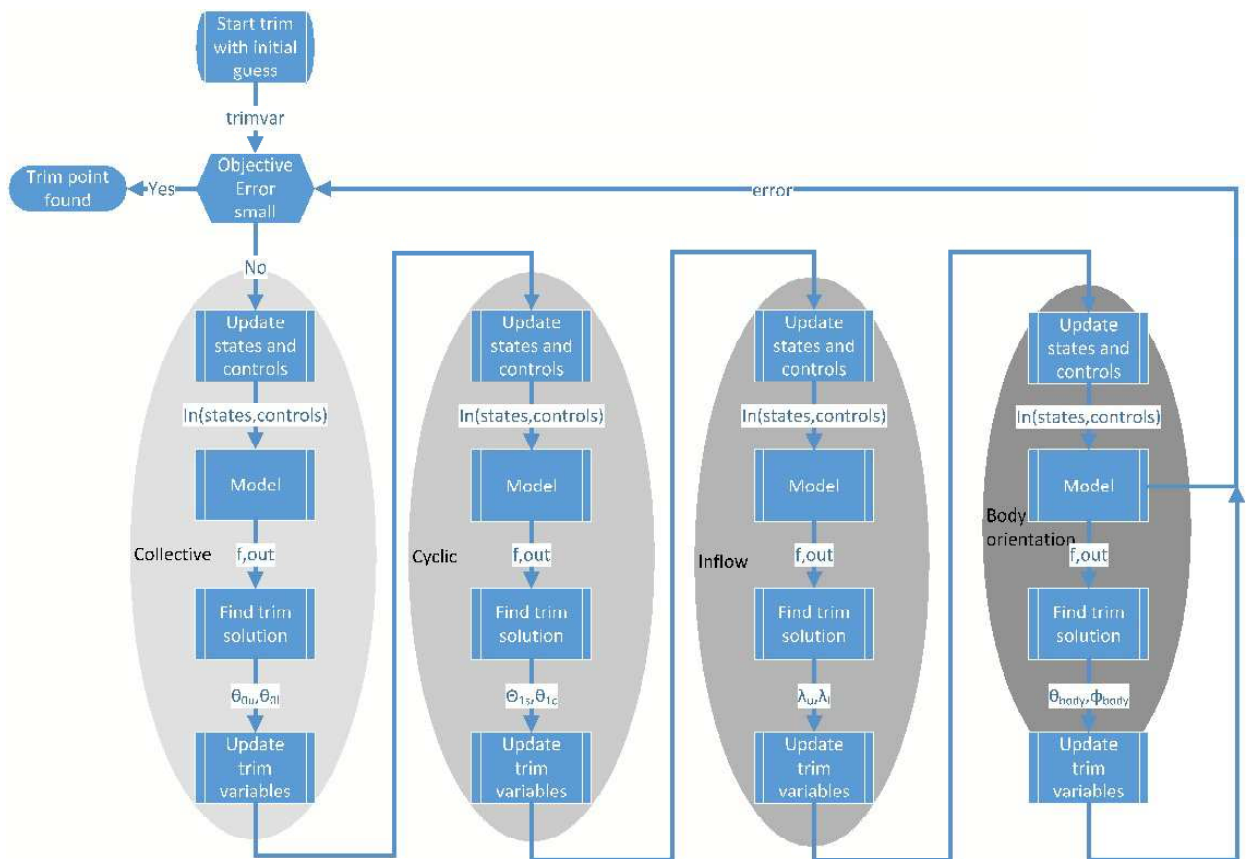
Figure 2.18: Workflow diagram Sweep solving method

vertical acceleration and one were the yawing moment is zero. The intersection of these lines indicates a trim-point. An example of such a plot can be seen in figure 2.19. The found intersection gives a solution for both collective angles.

The controls are then updated with these new collective angles. The next step is to repeat this procedure for the cyclic control angles. Now the angles are varied between $-25°$ and $25°$ and the pitch and roll moments are compared to find and equilibrium. The resulting trim point will add the lateral and longitudinal cyclic angle to the solution that is found. To find the trim-point this process has to be repeated for all trim variables. This means the inflow velocities for the upper and lower rotor are used to obtain an equilibrium in the momentum and BEM thrust. And the fuselage pitch and roll angles are changed to find an equilibrium for the lateral and longitudinal forces. The last step is to calculate the objective value using the newly calculated control inputs. When the objective value is smaller than the predefined limit the control inputs are accepted as the trim solution.
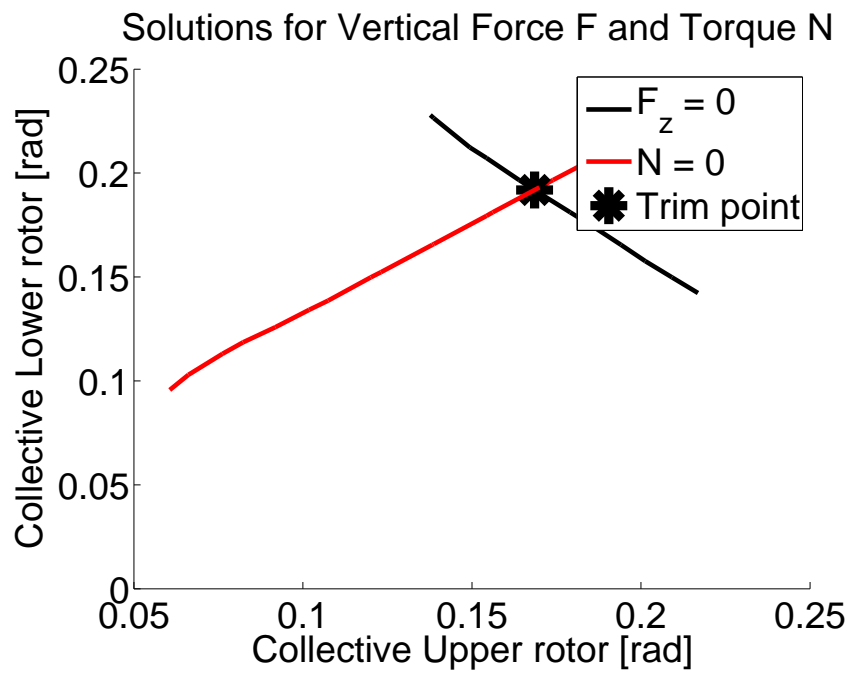
Figure 2.19: Example of the collective sweep trim point

Chapter 3

Results

The main results that can be presented are the trimmed flight results. Also, the performance calculations will be presented here. With the goal of getting insight in the limits and capabilities of the developed model. The assessment of these limits and capabilities was difficult since there was little reference information available. The main source for the reference material used is the paper by Campfens (2008). For the coaxial data this was the only source. It is also noted by Campfens (2008) that the references to validate the model were difficult to find. The process will, however, give a general sense of the correctness of the models responses. In section 1.4.3, the ability of the modular set-up was verified. The trim results from the 'new' model were compared to the results from the reference Model provided by Campfens (2008). This verification was to check the results for a full-sized helicopter. Also, the different solving methods are compared here. The second part was to check the performance indicators for the Ka-32. This was to check the results from the 'new' models power calculations with those of the reference model.

The last part will present the same results for the small UAV case. Here, the results for the Guardian Angle MAV as well as the commercial Walkera Lama are presented. The result from the calculation process is shown for a single trimmed flight speed. This is to show how the trim curve was obtained. The trim curves for both the Guardian Angle and the Walkera Lama are presented next. Here, the effect of the different levels of accuracy of the calculation effect are shown. Finally, the results from the performance calculations for these MAVs are presented in section 3.2.3.

3.1 Modular Updated Model

3.1.1 Controls & states

There is little information on and availability of reference data for a coaxial rotorcraft. For this reason the verification of the model was more difficult than expected. The references were chosen to be the same as those of the reference model Campfens (2008). Here, the data are from a conventional Puma helicopter, which is comparable to the Ka-32 in size and role. Also, different solution method for the coaxial Ka-32 are compared to each other and to the references. To determine if the simulation data is fair and reasonable the results are compared to:

base Analytical model by Campfens (2008)

Newton New model using the Newton Iteration method

**Sweep** New model using the Sweep calculation method

1 New model using the Newton iteration method with a smaller step size

MoGeHM Puma trim Numerical BEM Model MoGeHM

SAAF Puma measurements Puma SAAF measurements

Comparing the results to these data sets would give a general idea of the fidelity of the results. In addition, the baselines of the expected behaviour for the model will be shown.

Collective angles
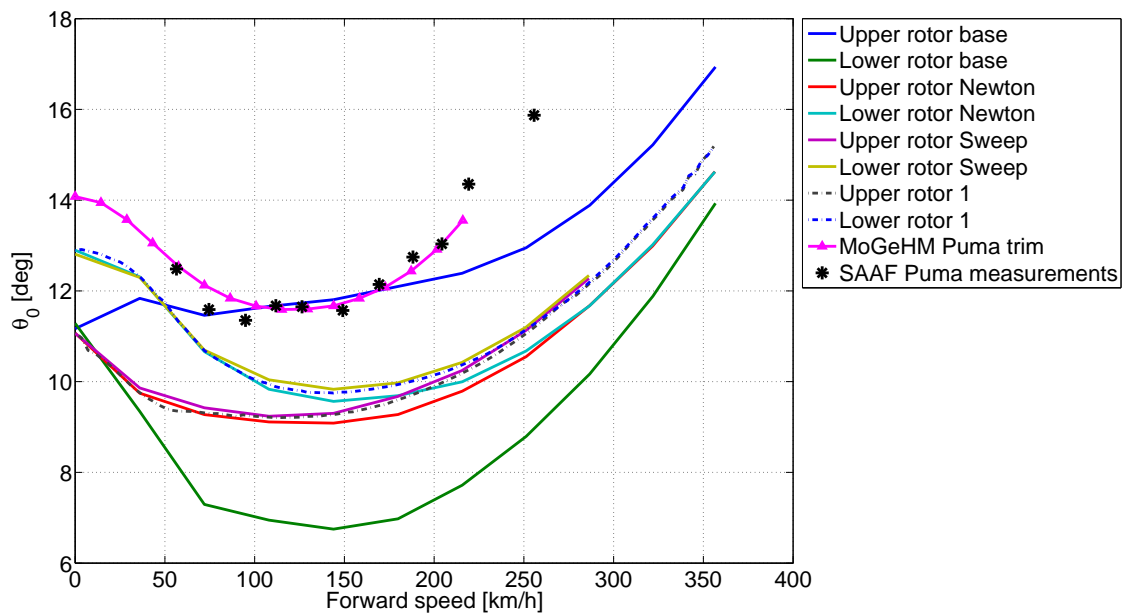
Figure 3.1: Collective angle verification

The first control input to be checked is the collective angle of both the upper and lower rotor. As can be observed in figure 3.1 the expected bucket shape can be observed in both the coaxial model and the conventional helicopter data.As can be observed the lower rotor collective angle has a larger value then the upper rotor for the new model. This is the opposite of what can be seen in the analytical model. The difference can be explained in two ways.Due to the interference effect from the upper rotor there is more collective required for the lower rotor. The extra induced velocity has its effect on the inflow angle ϕ. A larger inflow angle requires a larger control angle to obtain a similar angle of attack, which is required for a torque equilibrium.The second explanation is that the positive influence of the wake leads to a decrease in the drag that is generated on the lower rotor outside the wake. For torque equilibrium more collective angle for the lower rotor is required, which leads to more thrust being generated by the lower rotor. For a trimmed

(a) Upper rotor   (b) Lower rotor
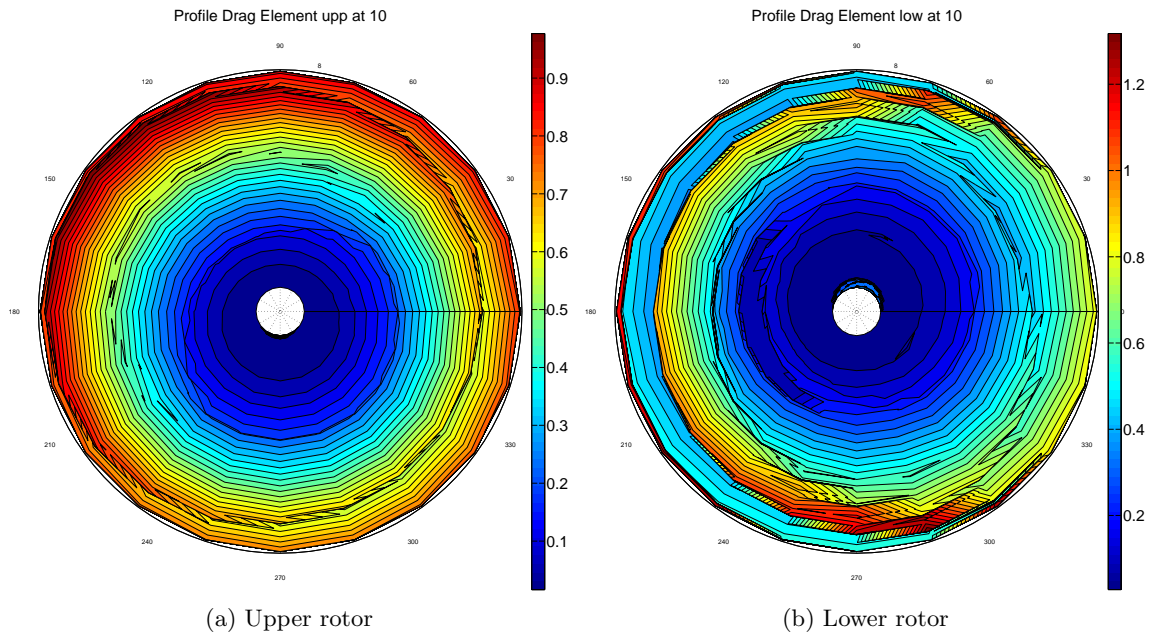
Figure 3.2: Local drag distribution at $10 \ m/s$

flight, weight is thrust, the upper rotor needs to generate less thrust in this case. This distribution was also observed by T. Nagashima and Nakanishi (1983).

The collective angles for the upper and lower rotors for the new model using different solving methods were expected to be the same. This is initially the case, but with an increase in forward velocity the collective angles as calculated by the sweep method become larger than those calculated by the Newton iteration method. The difference can be explained by the increased accuracy of the solution from the sweep calculations. This is confirmed when the results are compared with the Newton iteration method with a smaller step size. The smaller step size results follow the sweep calculation results more closely. It is further observed that the required collective angles at larger forward speed is larger for the more accurate calculation methods. The analytical model as explained earlier in section 1.4.2 shows the collective angle ratio in exactly the other way around. The upper rotor being the larger of the two collective angles. The jumps in collective control angles can be seen at 25.2 and 90 km/h these are caused by the wake modelling switching between functions used to calculate the effect.

Lateral cyclic

As stated in chapter 1 the coaxial rotor configuration has as a strength that there is no cross coupling between the control inputs. This means that the lateral cyclic should be zero in forward flight. In figure 3.3 it can be observed that this is not the case. All the coaxial models show an initial interference effect. The influence of the interference end at about 100 km/h. The analytical model shows the larger deviation with respect to the ideal. An increase in accuracy of the calculation method also doesn't change the results. A direct cause for this effect can be found in the asymmetric distribution of the local angle of attack. An example is shown in figure 3.4
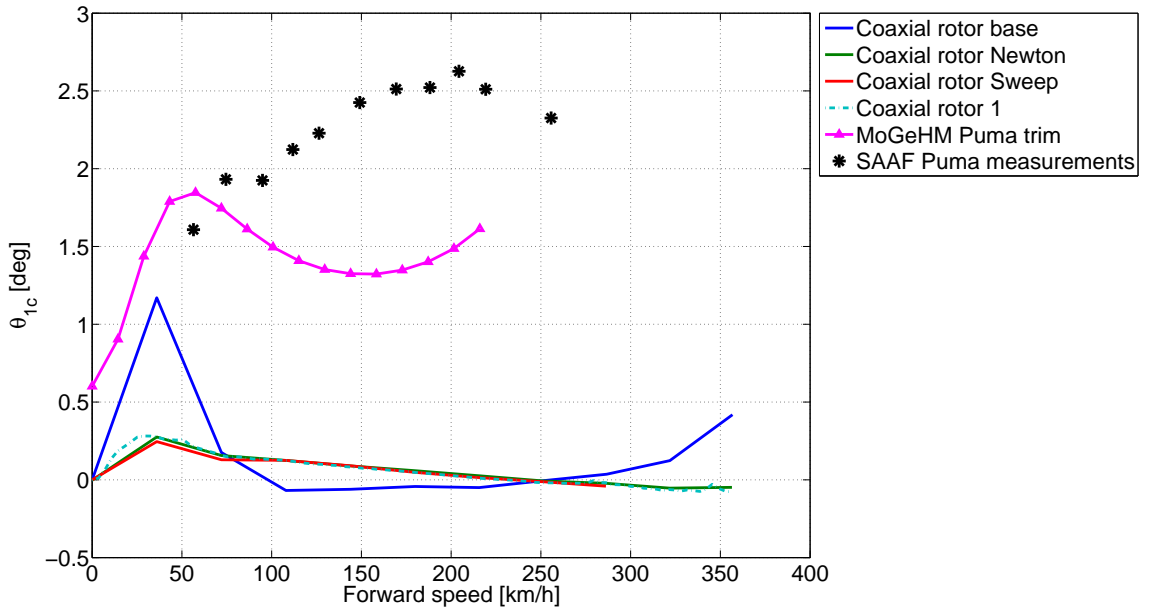
Figure 3.3: Lateral cyclic angle comparison
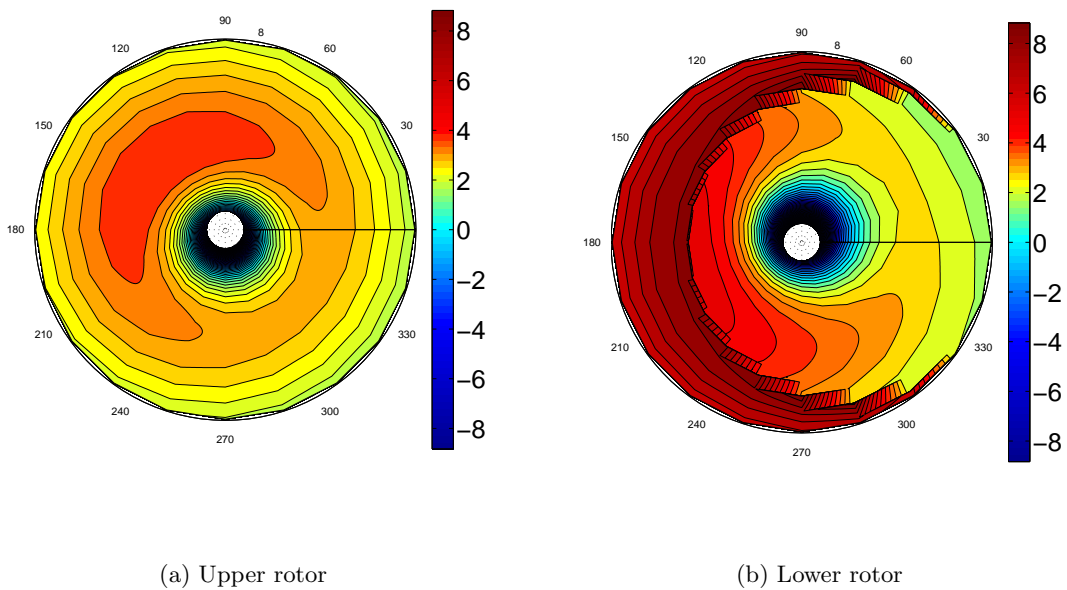
(a) Upper rotor   (b) Lower rotor

Figure 3.4: Local angle of attack at $10\ m/s$

This is the most likely caused by a strong influence of the upper rotors down-wash on the inflow of the lower rotor. Since the local angle of attack is dependent on the inflow angle and thus the generated lift. It can be argued that the lateral forces are different for both rotors. Thus, with the same lateral cyclic input the force for the upper rotor is not

the same as the lower rotor. The model uses a single lateral cyclic input this is the most likely cause. This cause also explains why the required lateral cyclic angle decreases with increasing forward velocity. This is due to the effect of the inflow angle on the angle of attack. With an increase of forward velocity the inflow angle decreases and thus the effect on the angle of attack. The Modular Reference Model shows the same behaviour albeit exaggerated. This large lateral cyclic input is carried over at a function switch point at 25.2 km/h resulting in a large jump in figure 3.3. Also, at the next switch point at 90 km/h a jump can be seen now to the expected zero input. The lateral cyclic inputs for trim of the Puma helicopter show that in comparison to a conventional helicopter the model does exhibit low lateral cyclic input.

Longitudinal cyclic

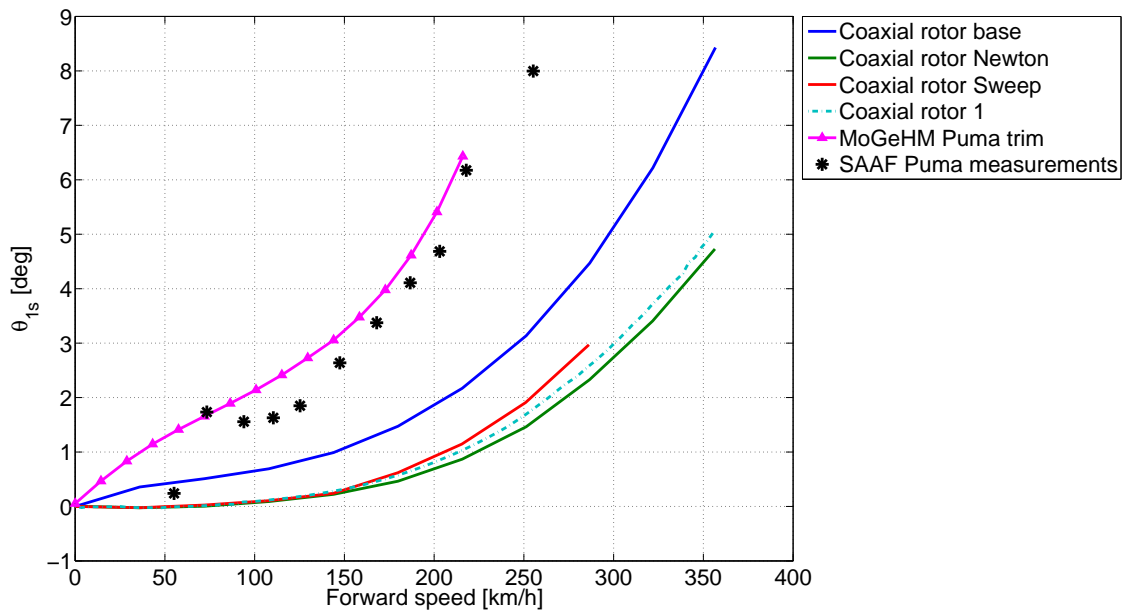**Figure 3.5:** Longitudinal cyclic comparison

The longitudinal cyclic angle is expected to increase with an increasing forward velocity. This effect can be observed in figure 3.5. At low speed the increase in longitudinal cyclic angle of the numerical models lags behind those of the references. Both the analytical model and the data for the Puma helicopter require a larger cyclic angle for a trimmed flight condition. A possible cause can be found in the resultant X force produced by the rotors. As can be seen in figure 3.6 this will provide forward force. Thus, reducing the required tilt of the thrust to counteract the drag.

At high-speed this is the cause of the reduced cyclic pitch angle with respect to the reference data. The general shape and the behaviour of the input, however, follow the same trend. Another possible cause can be found in the wake attenuation effect. At low forward velocities it will cause more loading at the rear of the lower rotor. The rear loading causes a moment which leads to a reduced requirement of the cyclic pitch.
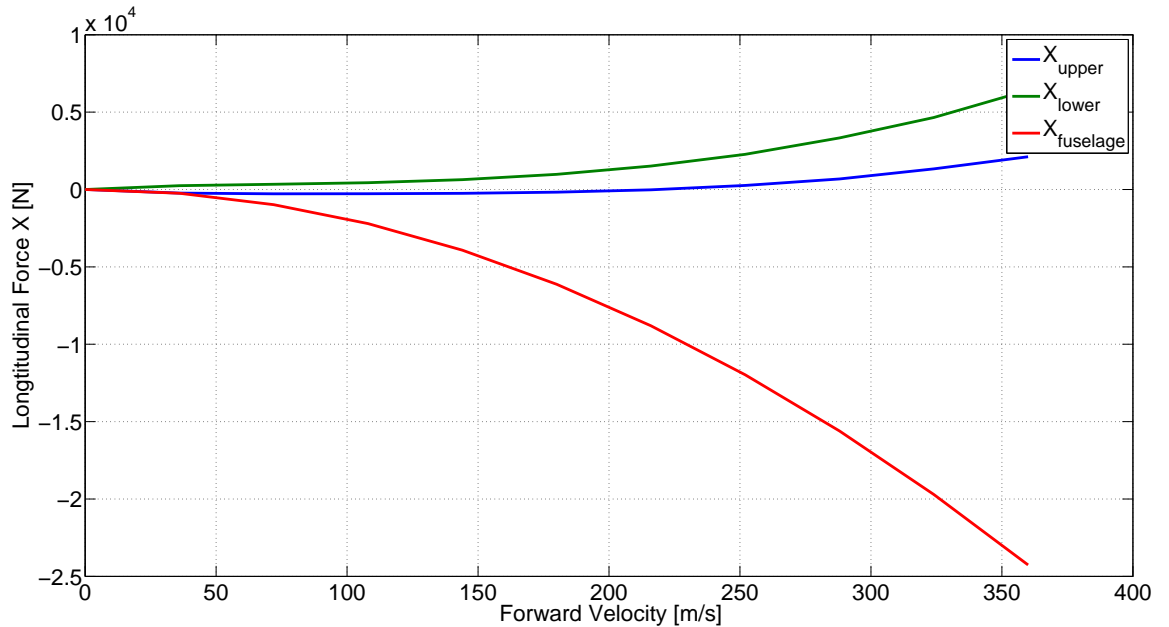
Figure 3.6: X force as a function of trim velocity

Fuselage pitch

The fuselage pitch angle is another comparison point. In figure 3.7 the main difference that can be observed is the change of fuselage pitch with forward velocity. The coaxial rotorcraft requires more body tilt at high-speed, which is likely caused by more aerodynamic drag produced by the rotorhead. There was an initial difference with the Puma data, which was caused by the difference in the rotor shaft tilt. For this reason, the Puma data has been shifted. The shifted results correspond well with those of the model as can be seen in figure 3.7.

Fuselage roll

The fuselage roll angle as a function of forward trimmed flight is shown in figure 3.8. As already stated the roll angle should be zero for the coaxial rotorcraft case due to the absence of the cross-coupling effect of the controls. The reference model shows a small fuselage roll with a larger jump at one of the wake calculation switch points. A more expected behaviour is shown in the new model. The jump at 25.2 km/h is gone and the body roll is very small up to about 144 km/h. At higher forward velocities the roll angle will, however, require larger control angles. This was not expected. For the sweep solving method and the increased accuracy Newton iteration method the results follow the same trend. Comparing these larger roll angles at high forward speed to the values from the conventional Puma helicopter show that the body roll is relative small.
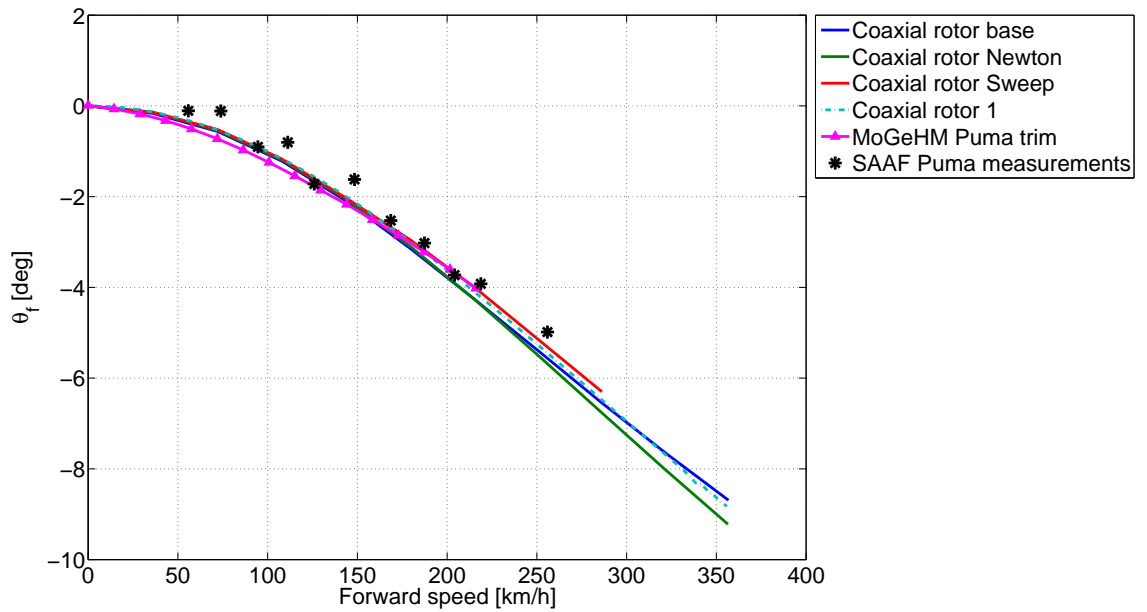
Figure 3.7: Fuselage pitch angle comparison
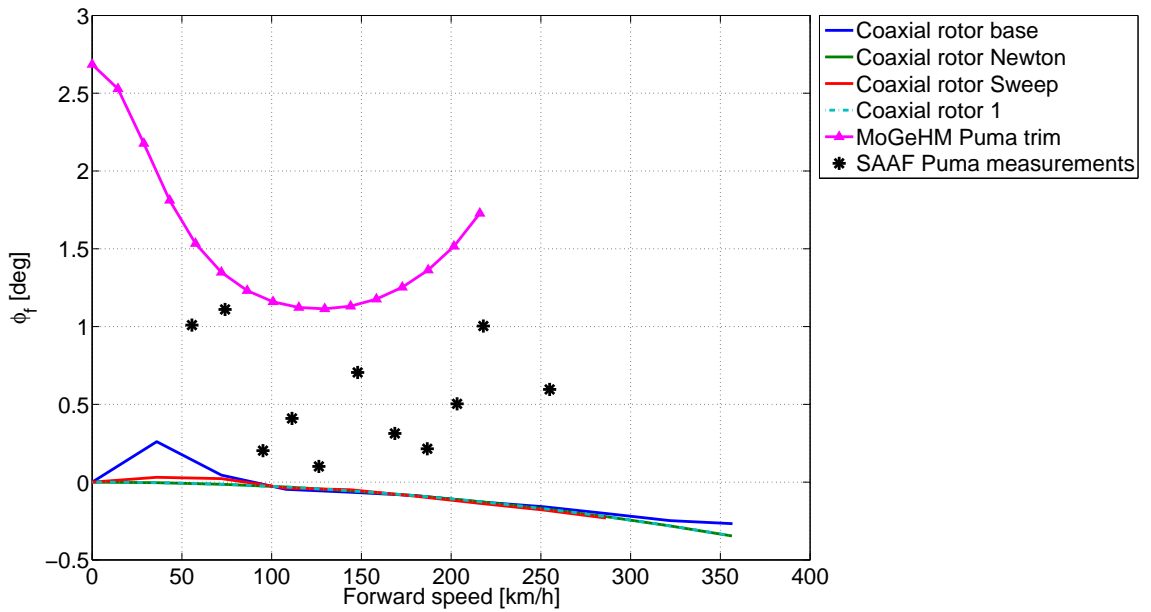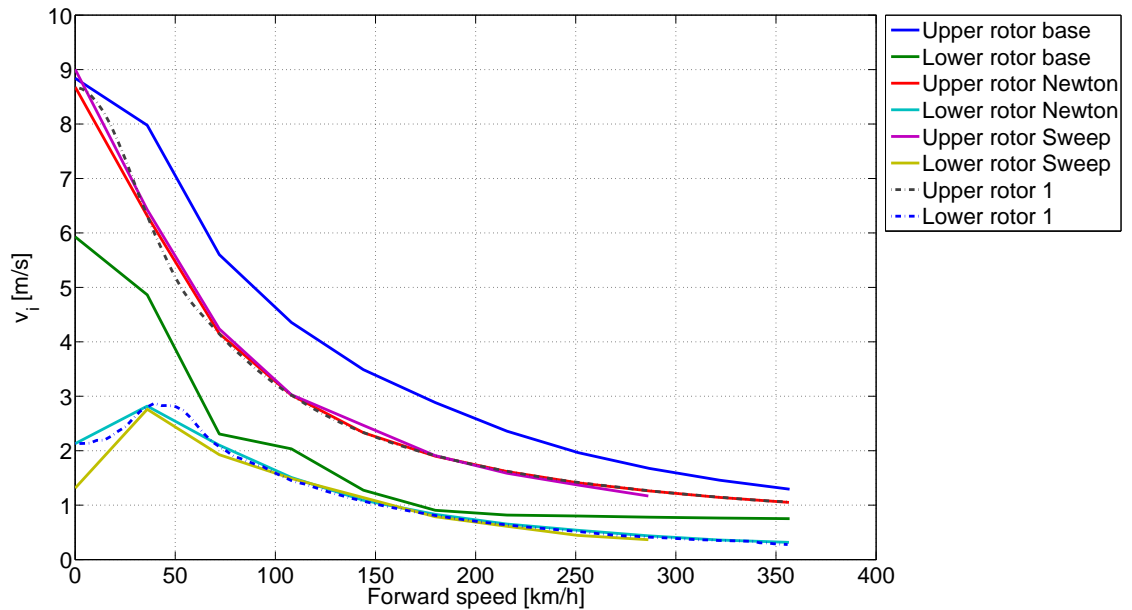

Figure 3.8: Fuselage roll angle comparison

Induced velocity

The coaxial model use a non-dimensional inflow velocity. The isolated induced velocity
of the upper rotor should always be higher than the one for the lower rotor. This is

Figure 3.9: Comparison of the induced velocities

when the attenuation coefficients are positive, in other word the wake is going down.The induced velocity for the lower rotor is indeed lower than for the upper rotor. This is the case for both the base model and for the new model. With increasing forward velocity it is expected that the induced velocities of the upper and lower rotor will approach each other due to the decrease of the interference effect at higher forward velocities.

For the new model the initial rise in the induced velocity of the lower rotor is noticed in figure 3.9. This effect can also be seen in the solution with a higher accuracy and using the sweep solution method. It is likely caused by the lack of torque which requires the controls to increase the pitch angle of the blade θ to increase the angle of attack α. For a trimmed situation the momentum thrust has to be equal to the blade element thrust. Thus, the induced velocity has to increase as well. This larger pitch angle can also be seen in the required powers in the next subsection. The induced velocity of the upper and lower rotor converge slowly for the reference model. A similar behaviour can be observed for the new model, although the effect is less. Proving the effect of the wake ebbs away at forward velocity. The lower rotor is, however, still influenced by the upper rotor. This can be seen in the fact that the induced velocity of the lower rotor is still smaller than for the upper rotor. The reference model has jumps due to the implementation of the wakes switch points. These jumps are absent in the numerical model which means that the new Models implementation of the wake/attenuation is working as it should.

3.1.2   Performance calculations

The new model could not be validated using the data presented in the previous section. There is, however, a continues power and a maximum velocity available at Jane's all the world aircraft. With the obtained states and control settings the power requirements of

the rotorcrafts parts can be calculated. Adding all the power requirements up leads to a total required power for the rotorcraft. In combination with the maximum available power this can be used to calculate the maximum velocity which can then be compared.

Parasite drag The first contribution is the parasite drag, which is defined as all non-rotor drag. It has been chosen to calculate this power by using the equivalent flat plate area as is shown in 3.1.

$$P_{par} = f \cdot \frac{1}{2} \cdot \rho V^3 \tag{3.1}$$

Drag and profile power The second contribution is the rotor drag and profile power requirement. This power is calculated in two ways. The first is extraction the power requirement from the results of the BEM calculations. This method is only available in the numerical implementation and uses the local drag on the rotor blade to calculate the power required. These calculations are explained in section 2.2.3. The second is using the drag profile approximation as specified by Bennet. The Bennets approximation as described in van Holten and Melkert (2002) is used and can be seen in equation 3.2.

$$P_p + P_d = \frac{\sigma \bar{C}_{Dp}}{8} \rho (\Omega R)^3 \pi R^2 (1 + 4.65 \mu_x^2) \tag{3.2}$$

Induced Power Also, the induced power requirement has two ways to calculate. The first method is again extraction from the results of the BEM calculations. This is done using the local thrust and induced velocities. The second is using the same definition of the power requirement by the tilting back of the thrust vector due to the induced velocity, but now for the whole rotor. The functions used are shown in equation 3.5.The total induced power for the coaxial rotorcraft is then the sum of both rotors.

$$P_{i-u} = kT_u \cdot v_{i-u} \tag{3.3}$$
$$P_{i-l} = kT_l \cdot v_{i-l} \tag{3.4}$$
$$P_i = P_{i-u} + P_{i-l} \tag{3.5}$$

Available power The available power can be calculated by multiplying the available power with the mechanical efficiency and the maximum continues power factor. This is shown in 3.6.

$$P_a v = P_e ng \cdot \nu_{mech} \cdot K_{cont} \tag{3.6}$$

Using the required power as shown in figure 3.10 the maximum forward velocity can be calculated. The velocity where the available and required power are equal is 240 km/h. This is higher than expected, which is either due to low parasitic power or to low profile drag.
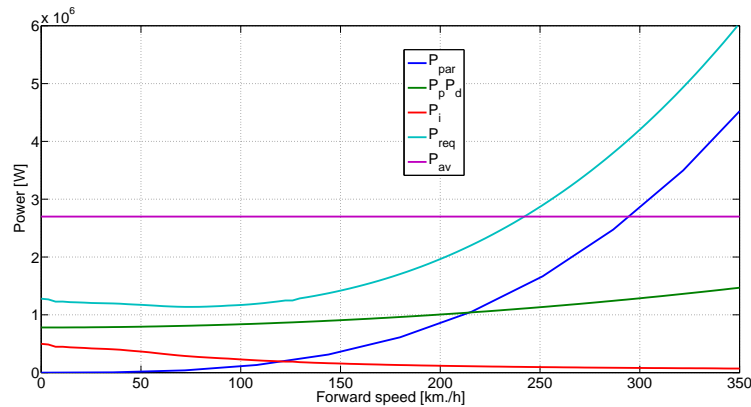
Figure 3.10: Power requirements parts using analytical calculations
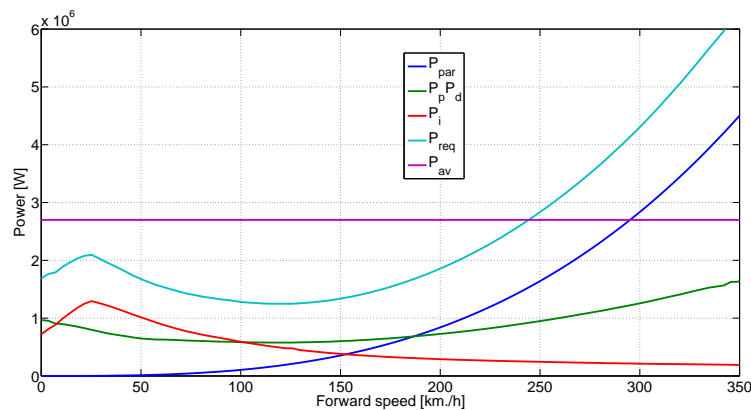
Figure 3.11: Power requirements parts using numerical calculations

The same figure is made, but now using the data provided by the Blade Element Method of the numerical Model as can be seen in section 2.2.3. The result is figure 3.11, and the maximum forward velocity can be calculated as 245 km/h. These calculated maximum velocities are close together. The difference is only 5 km/h, while using completely different method to calculate the resulting trim curves. Another phenomenon that can be observed in figure 3.11 is the wake influence shifting to the back at forward velocities. This can be seen as an increase in the power required and the induced power. This is caused by the extra pitch for the lower rotor blades, which is required to maintain a torque equilibrium. When the wake moves even further back the wake effect on the lower rotor reduces and so does the required power.

The contributions of the power requirement of the rotors towards the total power requirement is shown in figure 3.12. It can be observed that in hover, the power requirement of the rotors is almost the same as the total power requirement. The observation made in the induced velocity plot 3.9 can also be seen in these power calculations. The initial increase in induced velocity for the lower rotor with increasing forward velocity is thus translated to the rotors power requirement. This increase in induced power from the lower rotor is caused by the rotor wake shifting toward the back. This reduces the inflow velocity from
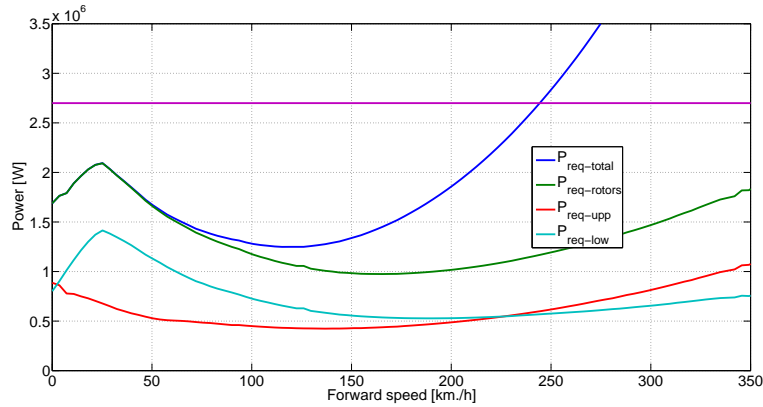
Figure 3.12: Contribution of the rotors towards the total

the upper rotor which requires the lower rotor to 'produce' additional induced velocity. The last observation that can be made in this figure is that the parasitic power determines the maximum velocity. The total power requirement of the rotors is only half of the total power requirement at the maximum forward velocity.
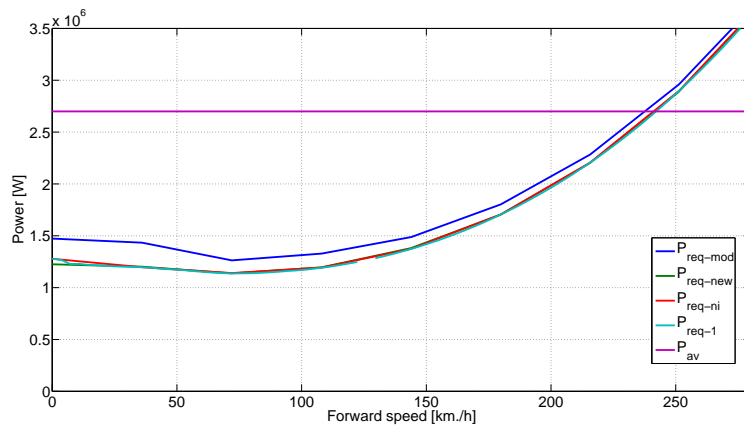
Figure 3.13: Comparison of the power requirement for different solving methods

Using the analytical power calculations the power requirements from the different solving methods can be compared. The result is figure 3.13. It can be seen that the power requirement for the reference model $P_{req-mod}$ is always higher than for the numerical model. For the new model the results show that the solving method $P_{req-new}$ compared to P_{req-ni} doesn't influence the resulting power requirement. Also, an increase in accuracy P_{req-ni} compared to P_{req-1} yields the same results.

3.2 Scaled modular updated model

Using the same methods as for the Ka-32a a trim curve for the small coaxial rotorcraft could not be obtained. For this reason a general calculation scheme was made to find

the resultant forces and moments corresponding to a specific set of control inputs. The purpose was to find the reason for the trim problem and/or find another way for a solution for trimmed flight. The general input data is from the Guardian Angel MAV and is shown in appendix A.3. To compare the possible input data as a cause for the problem also data from the Walkera Lama MAV was used. This data can be found in appendix A.2.

3.2.1   Sweep Trimpoint Calculation

In this section an example of the results from the general calculation scheme is shown. The flight condition for which the trim solution was searched was specified by the state vector and the control vector as defined in 2.4.1. For the forward velocity of 1 m/s, the altitude 30.48 m as well as initial values for the non-dimensional inflow for both the upper and lower rotor were assigned to the state vector. The control vector containing the collective angles for both rotors and the lateral and longitudinal cyclic were set to zero at the start. Evaluating a pair of controls over a range of possible values while keeping the rest of the states and controls constant a trim point can be determined. The resultant forces and moments and accelerations can then be shown in a plot. The trim point can then visually be identified by looking for the combination of control settings were both selected accelerations are zero. Which is then used to update the states and controls for the next calculation step. This process is repeated until all accelerations are small. The first pair of controls is the collective angle of the upper and lower rotor. A combination of these controls will be used to find a trim solution for the vertical resultant force and resultant yaw moment. The next step is to solve the lateral and longitudinal cyclic angle using the roll and pitch moments. The third step is to solve the induced velocities using the quasi-steady inflow value for the upper and lower rotor. Then, the fourth and last case is the body pitch and roll angles. These are solved using the lateral and longitudinal resultant forces.

(a) Guardian Angel   (b) Walkera Lama
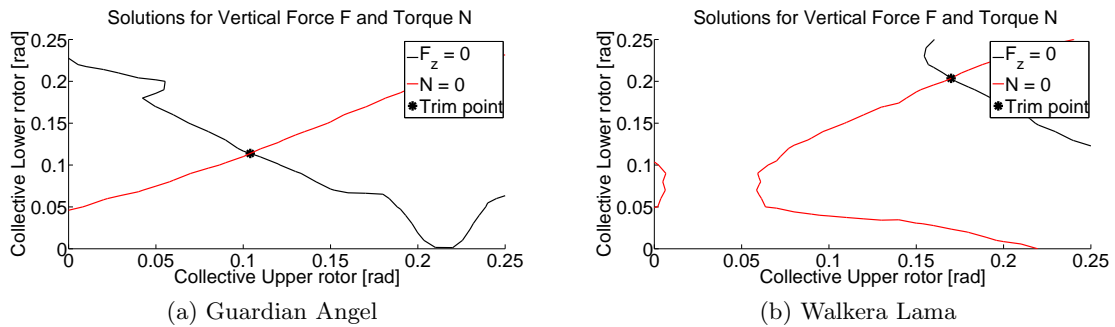
Figure 3.14: Collective angle trimpoint

To find a solution for the collective angles the choice was made to use the resultant vertical force F_z and yawing moment N. In figure 3.14 the solution for the resultant vertical force is shown in black while Torque equilibrium is shown in red. The plots for both the Guardian Angel 3.14a and the Walkera Lama 3.14b are very similar in how the solution space looks like. As expected the yawing moment solution is a line with similar upper and lower collective angles. This is due to the equilibrium between the two rotors. The lower rotors torque needs to be the same as the torque for the upper rotor. It is noticed that

the line starts with no upper rotor collective and a significant lower collective input. The resultant vertical force is a line from the lower rotor generating the lift for the complete rotorcraft at the top left to the upper rotor generating the same lift at the bottom right. The last part of the line indicates the upper rotor stalling, this requires the lower rotor to generate more lift. Similar trends were found in the solution for the full-size helicopter as can be seen in appendix B.1.

To find the lateral and longitudinal cyclic pitch angles for trimmed flight the pitching and rolling moments were used. Unfortunately no solution could be found for the Guardian Angel rotorcraft. The main cause lies in the large fluctuations in the size of the resultant moments. As a reference, the full-scale rotorcraft results show a linear dependence on the control inputs. The trim point is then easy to find. This can be seen in appendix B.1. The most likely reason the solver can find a solution is because of these fluctuations that are present in these moments. Taking a more detailed look the fluctuations in the moments are caused by fluctuations in the rotors angle of attack. Also, the angles are larger than was expected. The cause was found in the effect of the flapping motion on the angle of attack. The flapping motion as described in subsection 2.2.1 was checked and the cause was found in the combination of the models discritization and the geometric data for the rotor blades. When the discretization is to course, the solution is not found. There are thus more steps required which will take more calculation time. The solution can also be found if the size of the blade moment of inertia is increased. This is because the flapping motion doesn't fluctuate that much when the blade moment of inertia is increased. This conclusion is confirmed by the calculations for a slightly larger MAV the Walkera Lama. Here, the solution can be found without any changes to the blade moment of inertia. This can be seen in figure 3.15.
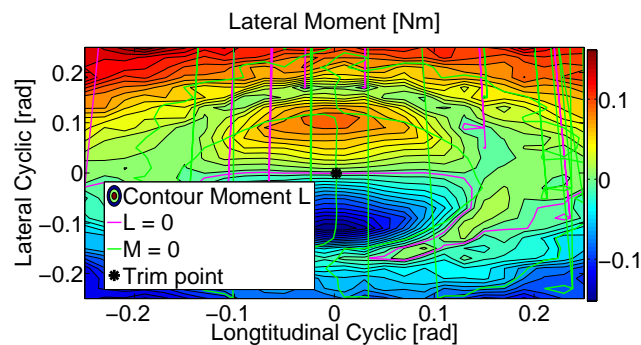
Figure 3.15: Cyclic roll moment results for the Walkera Lama

When the blade moment of inertia for the Guardian Angel is increased the results show the expected results as is shown in figures 3.16a and 3.16b.

Because of the use of the quasi-steady inflow the inflow values of the upper and lower rotor are part of the controls. The inflow should be such that the difference between momentum thrust and BEM thrust is small. As can be seen in figure 3.17a the error for the upper rotor only dependence on the value of the inflow on the upper rotor. This leads to the solution to be a vertical line as the inflow for the lower rotor does not matter for the solution. The results for the lower rotor as are presented in figure 3.17b are more complex. This is because when the upper rotor inflow is increased the lower rotor operating in its down wash is directly affected by this increase. With increasing inflow velocity the error

(a) Cyclic roll moment

(b) Cyclic pitch moment
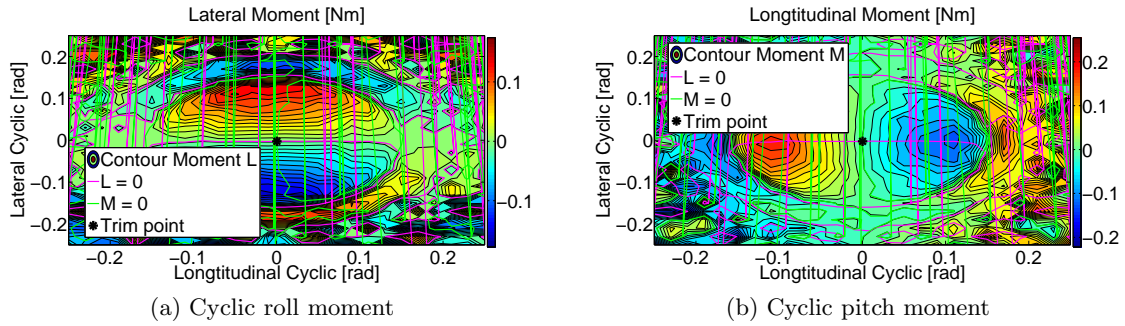
Figure 3.16: Moments with increased blade Moment of Inertia

(a) Upper induced velocity

(b) Lower induced velocity
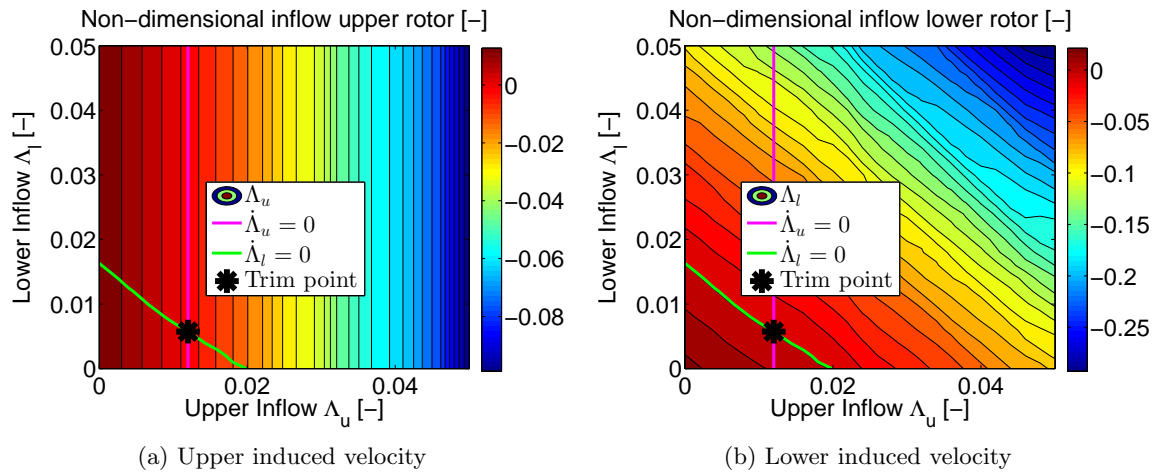
Figure 3.17: Quasi-steady Induced velocity

becomes more negative as the momentum thrust increases. The extremes are there for expected in the top right corner and the bottom left corner. Also, for the lower rotors a solution can be found for the inflow, it depends on both inflow values. The general solution for the inflow is then the intersection of these two line as shown in both figures.

(a) Longitudinal forces
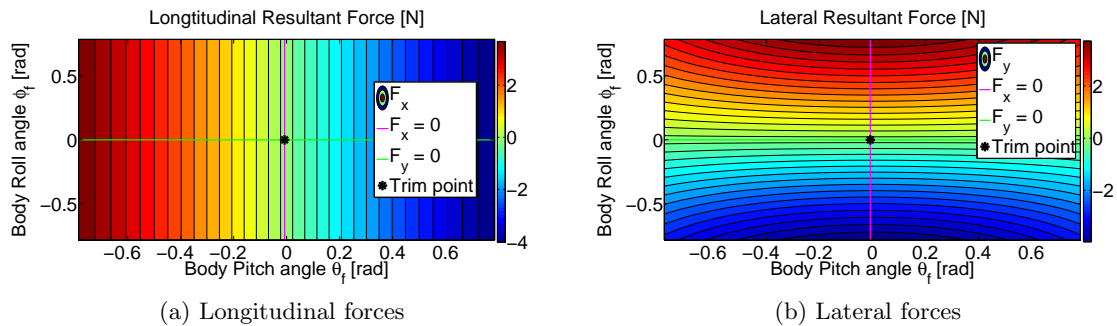
(b) Lateral forces

Figure 3.18: Sweep plot Body angles

The fuselages pitch and roll angle are the last control inputs to be changed. Now the lateral and longitudinal resultant forces are used to find an equilibrium position. As can be seen in figure 3.18a the resultant x forces varies with the pitch angle. The solution is

then a vertical line at a specific pitch angle. In figure 3.18b the lateral force y is shown. Here, the main influence is the roll angle, although at larger roll angles the pitch angle also has influence on the resultant force. The solution is then found in the form of a line for the roll angle were the lateral resultant force is zero. The trim condition is then specified as the intersection of these two lines. Thus, defining the body orientation.

Accelerations vs. Control inputs

Using this process to find a solution for a steady state trimmed flight condition takes around 3 hours to calculate. After a number iterations, the error in the objective function is reduced to around 0.5. Meaning the largest acceleration is 0.5 m/s^2 or rad/s^2. At this point the accelerations of the rotorcraft are set-out against the control inputs. Due to the link between the upper and lower collective with both the vertical acceleration $\dot{w}$ and the yawing acceleration $\dot{p}$ the influence of both collective angles is explored as can be seen in figure 3.19.

Figure 3.19: Vertical and yaw acceleration vs. Rotor Collective angles

For the rest of the body motions a single control input has the most influence on the corresponding accelerations. These are for the cyclic input the lateral cyclic θ_{1s} and the rolling acceleration $\dot{q}$ as well as the longitudinal cyclic θ_{1c} and the pitching acceleration $\d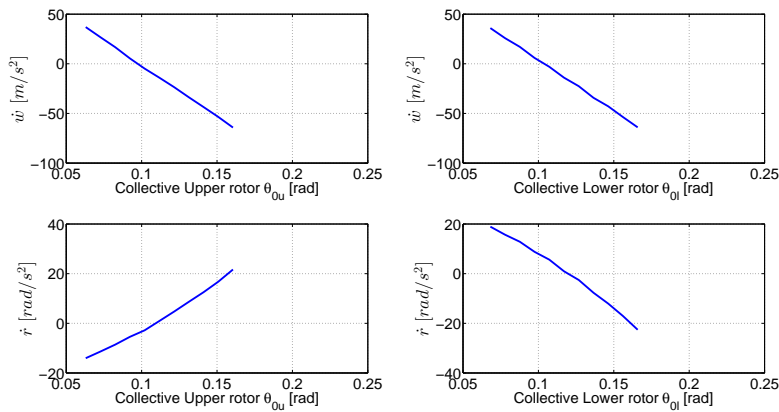ot{p}$ as is shown in figure 3.20. Since the rotation rates are set to zero at the start of the trim routine, a rotational acceleration of zero leads to a steady state.

The body roll angle ϕ_f and the lateral acceleration $\dot{u}$ are linked. This is also the case for the body pitch angle θ_f and the longitudinal acceleration $\dot{v}$ as shown in figure 3.21.

Although the inflow of the upper rotor influences the inflow of the lower rotor, it is chosen to only show the influence of the respective rotor. Thus, the quasi-dynamic inflow of the upper rotor is shown with the change in inflow of the upper rotor. This process is repeated for the lower rotor as can be seen in figure 3.22. More information can be found in appendix C.3.
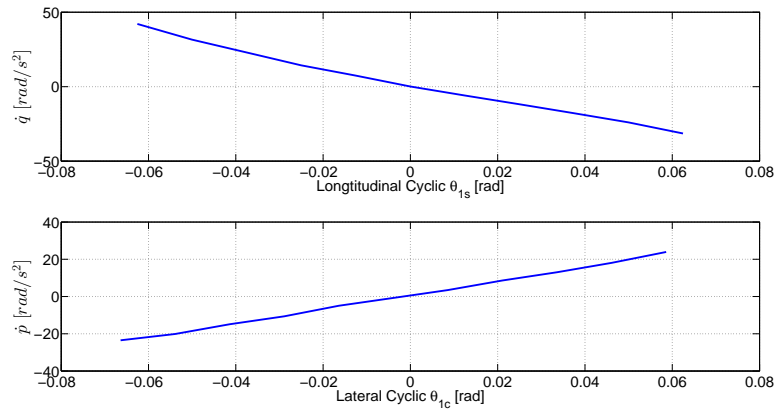
Figure 3.20: Pitch and roll acceleration as a function of Cyclic angle
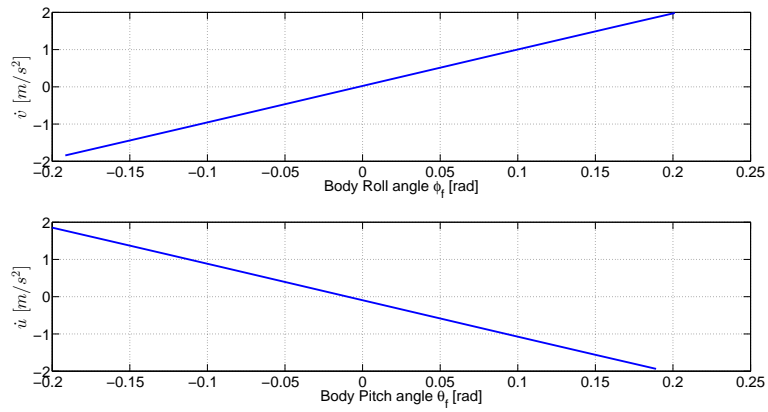
Figure 3.21: Body translational acceleration vs. body pitch and roll angle
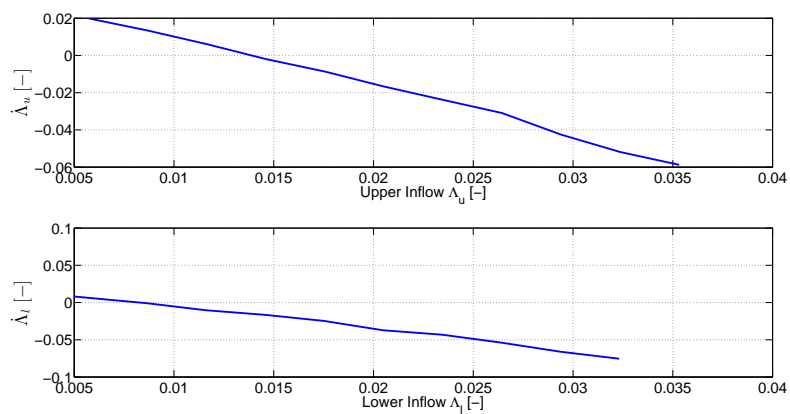
Figure 3.22: Quasi-dynamic inflow of the upper and lower rotor

3.2.2   Controls & States

The sweep calculation results as are explained in section 3.2.1 can also be repeated for other flight velocities. The result is a complete trimmed flight curve for both the modified Guardian Angel MAV and the Walkera Lama. Due to the limited availability of reference data the trim results for the control settings can be used to determine if the results are reasonable. This is done by assessing the values and the general shape with expectations. Also, the power calculation can be used in the same way as for the large coaxial rotorcraft to determine among others the maximum forward velocity. The data to be compared is with low, medium or high-level of accuracy. This means that the accelerations for the trim situation are below 0.9, 0.5 or 0.1 m/s^2 or rad/s^2.
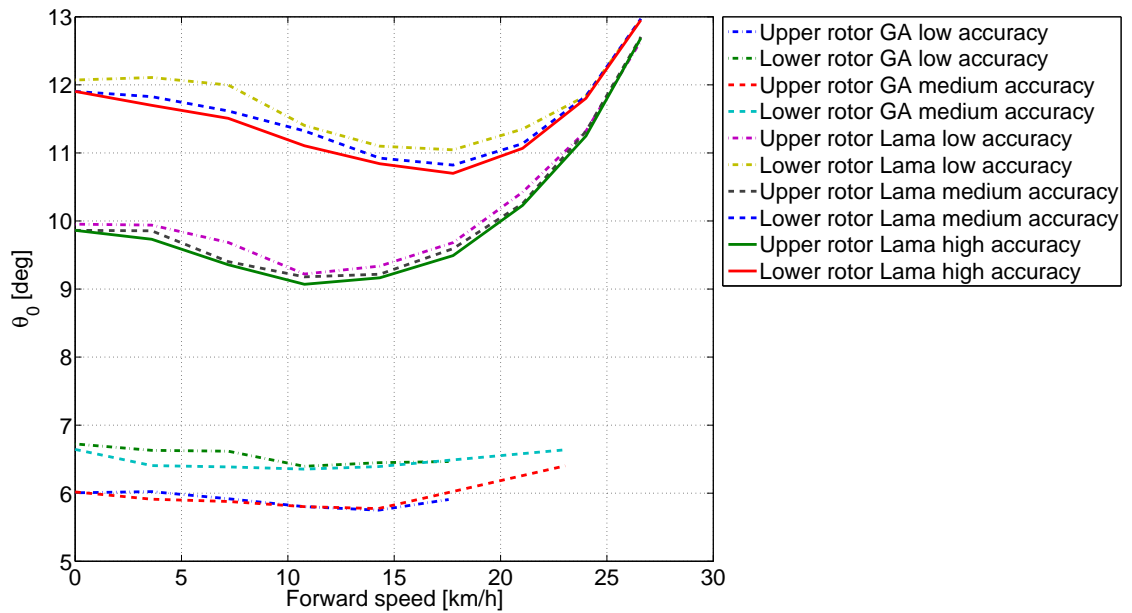
Figure 3.23: Comparison of the Collective angles

The collective angles for both the upper and the lower rotor are the first to be reviewed. In figure 3.23 it can be observed that the expected bucket shape is only shown in the Walkera Lama results. The Guardian Angel collective angles show a rather flat profile. The cause was found in the high rotational speed of the rotors in the Guardian Angel MAV. In all the results, the lower rotors collective angle is larger than the collective angle for the upper rotor. This was also the case for the larger helicopter using the same model. The required collective angle for the upper and lower rotor also approach each other high forward velocity, which was also seen in the results for the larger helicopter. The accuracy has an effect on the collective angles for trimmed flight. With an increase in accuracy the required collective angle for both the upper and lower rotor decreases slightly. This is the case for both the Guardian Angel MAV and the Walkera Lama.

Due to the coaxial configuration the lateral cyclic was expected to be small or even zero. In figure 3.24b it can be seen that this is not the case. The lateral cyclic is not small compared to the longitudinal cyclic. It further shows some irregular behaviour. The

(a) Longtitudinal Cyclic angle   (b) Lateral Cyclic angle
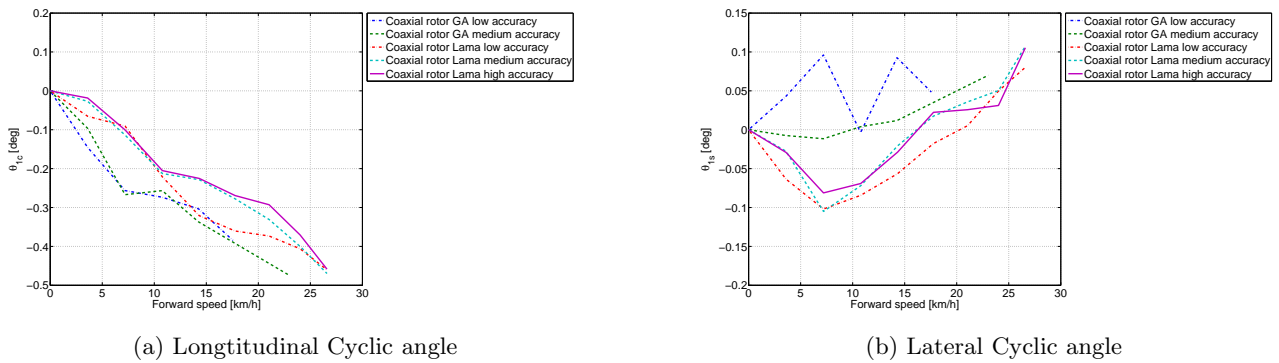
Figure 3.24: Comparison of the cyclic controls for the GA and Lama

observed wake effect seen in the large helicopter can also be seen in the data for the Walkera Lama. The deviation in the control angle is shown between 0 and 15 km/h. In the Kamov the asymmetric lift effect was observed to disappear with forward velocity. This is not the case for the Walker Lama. The longitudinal cyclic is shown in figure 3.24a. For both the small scale rotorcraft it doesn't increase with increasing forward velocity as was expected and seen in the results for the Kamov. The longitudinal cyclic does, however, flow the trend that the control angle increase with forward velocity albeit in the negative direction. A possible cause can be the loading of the rear of the lower rotor at low speeds. This was also noted for the results of the larger helicopter.

(a) Pitch Angle   (b) Roll Angle
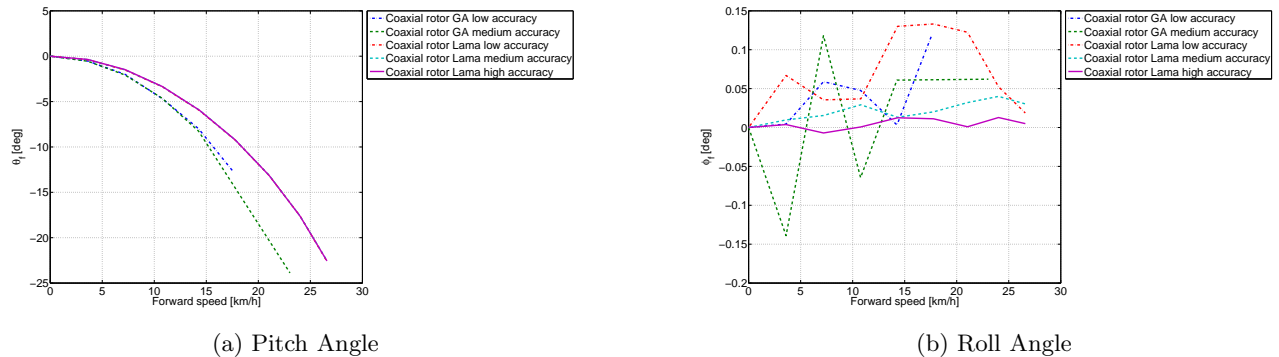
Figure 3.25: Comparison of the body orientation for the GA and Lama

The next results are the body orientation of the MAVs as seen in figure 3.25. A coherent body pitch angle result for the Lama MAV is shown. The angle increases with increasing forward velocity with the accuracy of the calculation having no visible influence on the results. The Guardian Angel also shows the same behaviour, but now the medium accuracy calculation show larger body pitch angels than the same low accuracy results. The most noticeable part is that the required pitch angles for the MAVs are much larger than for the large helicopter. The roll angle results show the same irregular behaviour as was observed for the lateral cyclic input. This is the case for all results except the high accuracy results for the Lama. Here, the body roll is very small and almost steady, as is to be expected for a coaxial rotorcraft. So the calculation accuracy has a significant influence on the lateral motion of the MAVs.
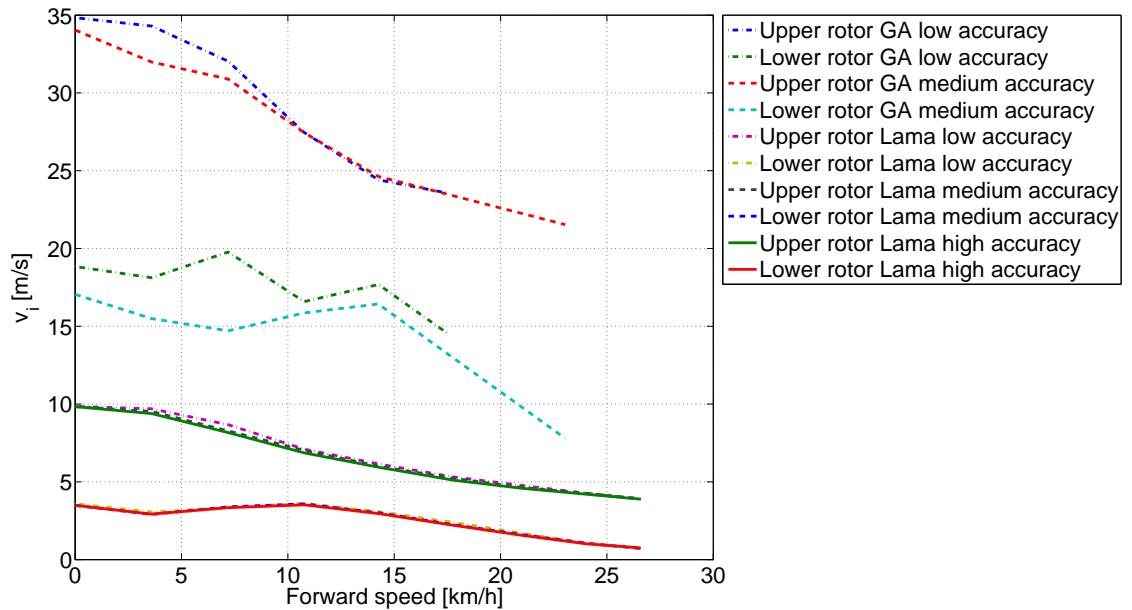
Figure 3.26: Comparison of the generated induced velocity

As the used coaxial model is the same as for the larger helicopter the model uses non-dimensional inflow velocities. Again, when the wake is going down, the attenuation coefficient is positive. In this case, the induced velocity of the upper rotor should be higher than the induced velocity of the lower rotor. For both the Guardian Angel and Walkera Lama this is exactly the case as can be seen in figure 3.26. The upper rotor has a higher induced inflow velocity than the lower rotor. There are two things that are noticed initially. The first is that the induced velocities seem to decrease linear, while this was not the case for the large Kamov. Also, the induced velocity of the upper and lower rotor do not appear to approach each other at higher forward velocities. This is especially the case for the Guardian Angel. This can be interpreted as that even at higher forward velocities the upper rotor some influence has on the lower rotor. The initial rise in induced velocity for the lower rotor is also not observed. This is an indication that the lower rotor generates a similar required torque as for the upper rotor for hover and low speed forward flight. The induced velocities as required by the Walkera Lama are in the same order of magnitude as the Kamov 32. The Guardian Angel needs about three and halve times this inflow velocity. A likely cause can be found in a relative small rotor diameter compared to the weight. Also, the high rotational velocity of the rotors will cause a small rotor pitch angle to produce a relative large down-flow. What can also be observed is that the results with a higher accuracy needless induced velocity.

3.2.3 Performance calculations

The performance quality of the model can be assessed by comparing the maximum velocity as specified with the developed power by the motors. Both the maximum velocity and the type of motors used by the Guardian Angel and Walkera Lama are known. With

the states and controls for a trimmed flight the power requirements of the different parts of the rotorcraft can be calculated. The required power can be calculated by adding all these power requirements up. Also, the available power can be plotted. The maximum velocity is then the velocity where the available power is the required power. The power requirements for the rotor in these MAV models is calculated by the blade element method.

(a) Guardian Angel

(b) Walkera Lama
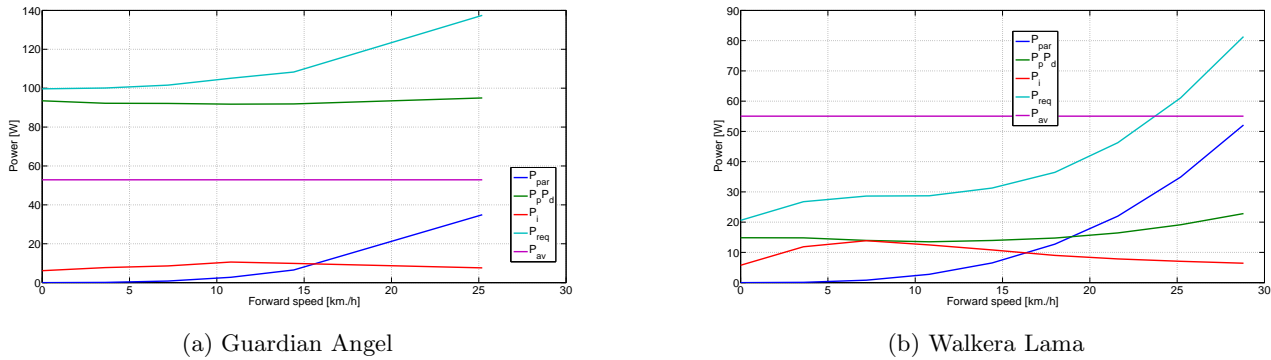
Figure 3.27: General Power calculations

The maximum velocity can be calculated from the data as presented in figure 3.26. For the Guardian Angel the required power is much larger than the available power specified in the design. In figure 3.27a the available power is 56 Watt while the required power can rise to 140 Watts at a forward velocity of 25 km/h. It is there for impossible to estimate the quality of the model's performance based on the results form the Guardian Angel. The maximum velocity for the Walkera Lama is specified as about 15 miles per hour, this is 24 km/h. Comparing the available power with the power requirement as shown in figure 3.27b, the maximum velocity can be determined to be 24 km/h. This means that the performance for the Walkera Lama is predicted reasonable well. While the wake influence on the induced velocity was not visible, it can be observed in the power calculations. The Induced power increases initially until about 10 km/h. This is an indication that the lower rotor in the Walkera Lama model needs more pitch to increase the torque for a trimmed flight situation.

(a) Guardian Angel

(b) Walkera Lama
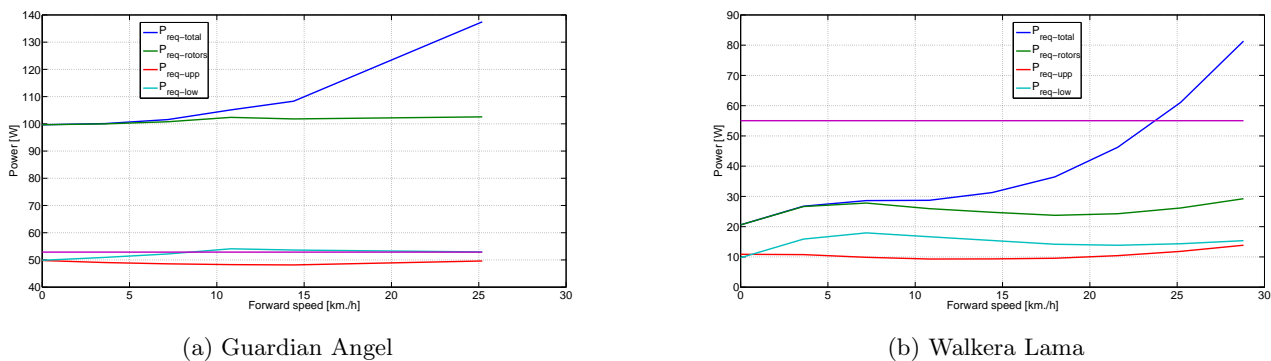
Figure 3.28: General Power calculations parts

The contribution of the different parts of the rotorcraft towards the total required power can be seen in figure 3.28. Again, the power consumption at hovering flight is almost

completely required for the rotors. This is the case for both the Guardian Angel and the Walkera Lama. For the Walkera Lama the same observations as for the Kamov 32 can be made albeit tuned down and at a smaller scale. From the hump in the power requirement of the lower rotor to the parasitic drag determining the maximum velocity, all these effects are present. The plot for the Guardian Angel looks different. The plot is dominated by the rotors power requirement, which is two times 50 Watts. It is further observed that the power requirement of the rotors changes very little with forward velocity, which was not expected. This might be the cause of the difficulties encountered trimming the Guardian Angel model. From the previous results for the MAV models it can be concluded that the performance can be estimated relative well. However, when the rotorcraft becomes to small the used modelling is unable to find a suitable trimmed flight situation. It was also observed that the results greatly depend on the chosen discritization and solving method. In general, the larger the number of sections the better the results. A downside is that the required calculation time increases accordingly. For the MAV the required calculation time varies between 10 and 18 minutes for a single trim point. This means that the complete trimmed flight curve takes about three hours to be calculated.

Chapter 4

Conclusion

One of the goals was to adapt a coaxial model to incorporate a numerical Blade Element Momentum Theory for a coaxial rotorcraft. Another objective was to model the non-linear aerodynamic behaviour on the rotor blades. To be able to implement these adaptations. It was necessary to change the aerodynamic and mechanic modelling of the rotor. A modular approach was taken to ensure compatibility and ease of changing the modelling methods. The main objective was the implementation of the numerical Blade Element Momentum Theory. This made it possible to implement the complete modelling parameters for the rotor blades. The first observation that can be made is that making a numerical coaxial rotorcraft model using a BEM and a wake model is possible. This disproves the statement made by Campfens (2008). That is that numerical integration of the BEM with a wake model will not work. The numerical integration of forces works correctly. Although the time required to do so is larger than was expected. The main cause for this was the required discretization to obtain a usable result.

One of the challenges encountered was to obtain the data required to initiate the rotor calculations. The most important being the look-up tables containing the aerodynamic lift, drag and moment coefficients. The look-up process (using the local angle of attack, Mach and Reynolds number to find the corresponding lift, drag and moment coefficients) was implemented correctly. It was also observed that not every table can be used for this purpose. The requirement of the combination of a low Reynolds number and a high Mach number makes finding suitable tables difficult. Another problem was that some tables are not smooth enough for the lift curve slope $C_{L\alpha}$ to be used reliable. Finding a complete list of the geometric and mass data for the rotorcraft was also not easy. This was caused by difficulty finding the properties of the fuselage of the Ka-32 and the Lama MAV. The properties of the Guardian Angel MAV were extracted from the CAD drawings solving part of the problem. For the Ka-32 the missing properties were substituted with values from the Puma SA-330, which is a similar helicopter. The implementation of the modular setup for the model was a success. The modular set-up makes it possible to check parts of the model separately. Also, the individual parts can be swapped with newer versions or with better modelling methods. The main challenge encountered here was making the connections between the different parts of the model. The correct implementation of the rotor's wake was the most difficult task. Due to the encountered problems a thorough look at the input and output definition was taken. Solving the connection issue, also the data management was improved. As a result the required calculation times were reduced.

To make a complete model was also one of the goals. This means being able to use the design parameters specified in input files to evaluate the specified design. The design parameters to describe the design include the fuselage including possible control surfaces at the tail. Also, the design of the rotorblades can be fully described. For example, the

local chord length, twist angle and aerofoil type can be specified just as the user would like. These specifications are all assigned to the blade station. From a designer's point of view the increasing number of inputs to describe the design is good. The downside is, however, that the increasing complexity of the blade definition leads to an increase in calculation time. This is caused by the requirement of a finer discritization of the mesh to find the steady state operating point. Although this increasing number of inputs is good to describe the exact changes made to the design, from a calculation point of view the increasing complexity of the blade definition leads to the requirement of a finer discritization mesh. The result is larger calculation times. As part of making a complete model of a coaxial rotorcraft, the influence of the wake on the rotor also needed to be modelled. The choice was made to use Landgrebe's generalized wake model to determine the area of effect of the wake. The influence on the lower rotor was determined using the practical methods of Walther Castles. These methods use attenuation coefficients to calculate the induced velocity distribution below a lifting rotor. Both methods were chosen for comparison purposes, using the same methods used in the reference model. During the implementation of the wake and attenuation calculations the option of using other methods was taken into account.

Another observation was that finding a steady state trim situation was more problematic than anticipated. This was the case for the full-scale helicopter Ka-32, but even more so for the small sized MAV. The initial problems were solved after an extensive search. During this search also errors were found in the reference model. The most important being. A wrong wake transition check causing the solver to crash. Also, the attenuation matrix for a rotor section was calculated, but not used. This lead to a difference in the lower rotor's inflow velocity and as a result a different steady state situation. It took considerable time and effort to find and correct these problems. The final result was that a 'reasonable' steady state could be found for both test cases.

The general performance characteristics of the coaxial rotorcraft (Ka-32) show a similar behaviour to the analytical model. The control inputs show in general the same behaviour, even though the power requirements show a different behaviour. This behaviour is especially strong at hover and low forward velocity. It is caused by the requirement for a coaxial rotorcraft to have a torque equilibrium. In combination with the influence of the upper rotor's down flow on the lower rotor leads to an increase in the lower rotors angle of attack. This in turn causes the induced power for the lower rotor to increase. The expected result is to show the performance characteristics of a coaxial rotorcraft. Considering the result this is achieved quite well.

Another expectation was to be able to see the local effect at the blade elements. This was achieved by implementing a numerical integration method for the rotor blades. The result is that the user is able to see the local angle of attack and flow velocity as input values for the aerodynamic calculations. Also, the output values of these calculations, like the lift and drag coefficients can be viewed. The expectation was to be able to use numerical integration in combination with the Blade element method to observe the local flow effects. This part works as expected. As expected, the implementation of the numerical methods to calculate the trimmed flight results would not deviate too much from the analytical reference. The results show a similar behaviour of both methods. The results from the numerical method deviate from the reference values at a number of places. These differences can be explained by looking at aerodynamic behaviour at

the blades and the way the numerical method works. The most notable difference is the behaviour of the model at hover and low speed flight. At high forward speed the numerical implementation shows that the required collective inputs of both rotors approaches each other. This is not the case in the analytical model. Although the results differ from the expected result of being almost the same as the reference. The difference can be explained enough to say that the results could have been expected.

Another interest was to find out which design parameters of the rotor had the most influence on the performance of the helicopter. To be able to assess the effect of the parameters on the performance it is necessary to variate the different design parameters. Due to the difficulties obtaining an initial result, such a variation of the aerofoil type, chord length and local twist angle was not performed. The question 'which design parameter has the most influence on the performance?' can for this reason not be answered. Maybe in a follow-up to this research such a variation can be performed.

Also, of interest was the source of the highest power consumption. The total power consumption of the rotorcraft was divided into a part for the rotors and the rest of the helicopter. The power calculations for the rest of the rotorcraft are calculated using an equivalent flat plate area. For the power consumption of the rotors. It can be specified as caused by the profile and drag power or caused by the induced drag. Also, the power consumption of the upper and lower rotor can be evaluated separately. The result is that the induced power requirement is larger in the new model. This effect is the most notable at hover and low speed. When looking at the rotors separate, it can be observed that the extra induced power is caused by the lower rotor. This is due to the extra pitch angle for the lower rotor, which is required to obtain a torque equilibrium. When the rotorcraft's speed increases, this effect fades away. The performance of the aerodynamic modelling using a database to link the flight conditions to the forces acting works as expected. The modelling was implemented using a look-up table which links the angle of attack to a lift and drag coefficient. For the small scale extra tables can be added at appropriate Reynolds numbers to take the effects of the flow viscosity into account. These coefficients can be corrected for compressibility effects using the local Mach number. The main drawback that is observed on the implemented system is the required calculation time. This effect is enhanced by the required increase in discritization for use at a small scale.

The calculation of a generic MAV using the developed generic coaxial model was a success. Two different MAV were evaluated, the Guardian Angel and the Walkera Lama. The accuracy of the result, however, is difficult to assess. Due to a lack of reference data the accuracy of this model at a small scale cannot be verified. Especially the assumption made to model the wake in the same way as large scale rotorcraft contributes to this conclusion. The performance of the Blade Element Method at the small scale of an MAV is good. The calculation method performs the same as for a large helicopter. There was only one problem the small numbers in combination with the rounding of the answers may prevent the solvers from finding a trimmed flight solution.

Due to the difficulty of finding trimmed flight solution for the MAV. The effect of scaling on the performance cannot be assessed. Even though all indications are that the general behaviour is the same as for a larger helicopter.The main uncertainties that are encountered for the MAV are as already stated. This includes the uncertainty in the result of

the look-up table that is used. From CAD drawings the mass moment of inertia and mass properties were estimated. This means they have an uncertainty in their value. The generic setup of the coaxial rotorcraft model to evaluate a design was a success. Also, the model can use the input data of a small coaxial rotorcraft correctly. The use of the model to design an MAV, however, is possible. This is on the condition that the MAVs rotorblades Moment of Inertia is not too small. If the blades are too small, the model will be unable to find a trimmed flight condition. To develop a design tool, able to quickly evaluate a design it is a requirement to have an accurate model. The developed generic coaxial rotorcraft model cannot be verified to be accurate. This is because the uncertainties in the input and the lack of a suitable reference material. The development of a tool to quickly evaluate the effects of a designing on the performance of a coaxial rotorcraft are due to the above described limitations not possible. The main reason for this is the large calculation time required to obtain the results, especially at small scales. This in combination with the uncertainty of the accuracy leads to this conclusion. New insight about the importance of parameters for performance can therefore not be provided.

The validation and verification were not conclusive due to difficulties obtaining suitable reference material. The model can also be used to transform the rotorcrafts flight situation for the aerodynamic analysis. Modelling the upper rotor inflow with a uniform inflow is the main uncertainty, although it is a fair assumption to make with respect to the real flight conditions. For the small scale it might not be the case. The windtunnel data is assumed to capture the aerodynamic behaviour although at low Reynolds number the accuracy cannot be assessed. For the blade calculations the full 3D flow is simplified to a 2D flow for calculations thus neglecting the cross-flow component. This means that the swirl and the associated power consumption is neglected. The rotor forces are calculated as an average over one rotation, the effect to see the transient behaviour is not known and was not the purpose of the model.

The wake model is complex due to the large number of influences that act on the outcome of the wake. This was the reason to start with a simple base to assess the effects before increasing its complexity. Despite the initial expectations for the model, the final results were disappointing. This was due to the large calculation time required to solve the model as well as the increased complexity of the model.

The numerical model as developed can obtain trimmed flight curve for the reference helicopter the Kamov-32. As already stated the results could not be validated, but qualitative analysis shows the expected behaviours in the updated model. In this case, the expected behaviour is a bath tub shaped curve of the collective controls. It is, however, observed that the new model requires less forward cyclic input for the same cruise speed. Also, the cross coupling effects are visibly smaller. Due to the numerical integration additional information can be obtained from the model, in comparison to the analytical model. This additional data can be used to take a closer look at some unexplained behaviours also observed in the reference model. One of these is the unwanted roll behaviour at low speed. The cause as seen in the rotor conditions is the asymmetry in the local angle of attack. This angle of attack is caused by the extra induced velocity due to the wake. The effect of the induced velocity is strongest at low forward speed. In combination with the influence of the rotation direction on the local speed, which effect is also strong at low forward speed. These results were found only due to the implementation of the full wake attenuation in combination with a numerical BEM calculations of the forces on the

rotors.

The results show that there is a numerical limit for finding the lateral and longitudinal cyclic trim point. The choice of calculation steps in the sweep calculation as well as the discritization grid for the rotordisks have a very large influence on finding a trimmed flight solution. Also, the fluctuations in the roll and pitch moments show that the discretzation has more influence than initially expected. This is confirmed as a solution can be found when using a fine consistent (for the rotor and wake) mesh. The limit was found to originate in the calculation of the flapping motion. The rest of the resultant forces and moment yield the expected results and responses to the control inputs. Also, disappointing was the fact that the use of the blades equations of motion to find the flapping motion lead to a high calculation time. The calculation of a full rotation took six hours. The goal was to obtain result quickly. As a result this numerical method was not used and an analytical method was implemented.

Finding a suitable trim situation using the new model requires a lot of effort. The main problem was to reduce the accelerations to a reasonably small size. One of the possible future leads is to find the cause of these relative large accelerations. During the verification it was found that also the reference model contains errors. A number of these were corrected, but it leaves the option open for the verification of the new model to be improved. The final trim solution as found with the new model shows a smooth and logical curve, which is a better result than from the reference model. The main reason for this is the continues change of the attenuation matrix in the numerical model while the analytical model uses separate pre-calculated functions and checks to see which of these to use. Using the analytical method, the result is a fast method. The downside of this method are the jumps in the solution. The numerical model shows a smooth solution curve, but takes a relative long time to find it. For future research it might be beneficial to improve the analytical model with the jumps to have a good solution and a fast solution time.

In the analytical reference model an unexplained roll behaviour was observed. The same behaviour was shown in the numerical model. Using the additional information for the rotor in the numerical model it was found that the cause originated in the asymmetric inflow conditions caused by the rotation direction of the rotors. This behaviour is shown in the model, but it would be interesting to see if this behaviour also has physical significance by checking these results with windtunnel test or CFD calculations. The Sweep method used to obtain trim results for the MAVs is sensitive to discretization choices as well as requiring manual trim point choices to continue. The most likely cause is the aerodynamic input data. This can be confirmed or denied by checking the behaviour of the model using input data with different levels of accuracy. Initially the goal was to use the equations of motion for the blade to describe the flapping motion. Unfortunately this process took too long. When the flapping motion can be described quickly, about minutes, using the forces on the blade this might improve the solution for the trim calculation. The ultimate goal was to find a quick design tool. The developed model is, however, unable to full fill this goal. This was caused by the fact that even at 'rough' discritization it takes too long to find a trim situation. In table 4.1 the time required to find a trim situation with accelerations below $0.9m/s^2$ are shown as a function of the discritization and calculation steps.

The search has gained some scientific interesting looking at the modelling methods used

Discritization Rotor	Discritization Sweep Calculation	Time per step	Number of steps
8	25	00:03	12
20	25	00:15	7
40	25	00:53	8
80	25	03:20	8
20	12	00:03	7
20	25	00:15	7
20	50	00:52	10
20	100	04:10	10

Table 4.1: Required calculation times for a trimmed flight situation

and their limitations. The numerical BEMT modelling works fine. A trimmed flight condition can be found with the corresponding control inputs. Due to the modular nature of the model also parts of the model can be compared. The comparison of the numerical with the analytical parts correspond well with each other. The main difference lies in the flapping motion and the rotor forces which were expected due to the inherent modelling differences. Examples are the use of the aerodynamic look-up table and numerical integration. The increased complexity to the model also leads to the situation that the solution takes increasingly more time, which is undesirable. Despite the set-backs there are some successes. The main susuccesss the implementation of a coaxial rotorcraft with a numerical integration of the forces on the rotors. The rotorblades as well as the configuration can be changed using the implementation of the design parameters. Also, the implemented sweep solver makes it possible to see the behaviour of the stability and control around a trim point. The aerodynamic input can also be observed in more detail. The limits for the Reynolds- and Mach number as well as the angle of attack can be linked to the requirements for the aerodynamic behaviour. Using these limits and the expected behaviour the requirements for the look-up table can be formulated. The distribution of the forces on the rotordisk could give some insight in the behaviour of the rotorblades. This is even more the case when looking at the results with the wake influence incorporated. An example of this is finding the cause of the unexplained roll behaviour as was observed in the model.

Chapter 5

Recommendations

The development of this model delivered a complete model. The general results are also as initially were set out, although the calculation time to find these trim solutions are much higher than expected. Despite the high calculation time the model and parts of the model can still be used. With this in mind a number of recommendations can be made.

One of the feature of this model is the ability to calculate the operating conditions of a rotor. A problem that arose was the inability to validate the results. This was caused by a lack of relevant flight performance data. The same problem applies to the aerodynamic data tables. These are used to link the flight conditions to the forces generated on the blade. These tables were hard to find and rarely complete for the use in this model. The rotor aerofoils require an angle of attack range of -30 to 30 °. This in combination with a Mach number up-to 0.8 and at different Reynolds numbers. Obtaining this data might be a logical follow up to this research to check the validity of the model. Another point of interest is the unexpected roll behaviour found in the model by John Campfens. Initially it was thought to be caused by the simplification in the attenuation coefficients. It was, however, also found in the more extensive model without the simplification of the attenuation coefficients. The cause of this behaviour was found in an asymmetric angle of attack distribution on the rotor. The asymmetric angle of attack was in turn caused by the influence of the upper rotor on the lower rotor. To be specific the combination of the forward velocity and the rotation directions influence on the local velocity at the blade, as a follow-up this can be validated with windtunnel tests.

Another extension to this research might be to look into the difference between the analytical work out and the numerical approximation. The reason is that the analytical work out is relative robust. While the numerical model requires a precise set-up, which is quite sensitive. This might give insight in the reason for the different results and the reason for the numerical sensitivity. The initial idea was to extend the model with more than only a numerical integration method. The implementation of the numerical method took much more time than was expected. This is why the other suggested improvements to the model were never realized. It could be a good idea to compare the methods used and the one proposed to see if it captures the behaviour at the small scale better. These improvements were, to update the momentum check performed to calculate the thrust using non-uniform inflow. Also, the wake contraction can be updated with a new function derived for forward speeds. Finally, the wake for small rotorcraft is also something that can be looked into since there was only little data found describing the effects at this scale.

The rotor calculations can also be used to connect the velocities present in a rotorcraft movement to the velocities seen at the rotorblades. These results can then be used to define boundary layer calculations, for rotating blades. Possible solutions found could in

turn be used to refine the model. Another application is to use the model to calculate an optimal rotorblade. This works by letting the rotor calculations and the user specified distribution of forces to the specific conditions for the aerofoils. Then, using these conditions and a code like 'X-foil' to reverse engineer the aerofoil shape, with or without boundary layer calculations. The final step is to combine the aerofoil shapes and the blade definition to an optimised rotorblade.

Considering the depth of the search, and the number of different approaches followed to solve the problem. The results as are presented here, are the maximum attainable at this time. The conclusion can be drawn that the model developed is more difficult to implement for a steady trim solution for a small rotorcraft than was expected. Looking at the result from the trim calculations it can be shown that the cause of this result can be found in a number of causes. The main cause was found to be the size of the numerical values coming close to the size of the numerical noise. This causes an excessive flapping motion. This flapping motion is caused by the geometric data input and/or the coarse discretization of the blades motion. To be more specific the discretization in rotational and radial direction. The alternative is to use a fine discretization grid, which increases the calculation times significantly. However, this extra calculation time is unwanted and the results can also be obtained by performing windtunnel tests and/or CFD studies. From an engineering point of view the model is only usable as was envisioned for large rotorcraft with the limiting factor being the required calculation time. This is mainly caused by the required numerical discretization for the rotor blades required to obtain a suitable result for an MAV. This means that the calculation time increases even more. For the smaller scale rotorcraft the solving for a trimmed flight situation takes a lot of calculation time, 3 hours. As the goal was to find a method of solving the performance of a small coaxial rotorcraft fast, this model is deemed to take too much time to full fill the set goal. Alternatives such as windtunnel tests are then the only alternative as the CFD calculations are still deemed to be unreliable.

Chapter 6

Bibliography

Benedict, M., Ramasamy, M., & Chopra, I. (2010, JUL-AUG). Improving the aerodynamic performance of micro-air-vehicle-scale cycloidal rotor: An experimental approach [Article]. *JOURNAL OF AIRCRAFT*, *47*(4), 1117-1125. doi: 10.2514/1.45791

Bohorquez, F. (2007). *Rotor hover performance and system design of an efficient coaxial rotary wing micro air vehicle.* Retrieved from http://search.proquest.com/docview/304851836?accountid=27026 (Copyright - Copyright UMI - Dissertations Publishing 2007; Last updated - 2013-06-07; First page - n/a; M3: Ph.D.)

Bohorquez, F., & Pines, D. J. (2003). Hover performance of rotor blades at low reynolds numbers for rotary wing micro air vehicles. *American Institute of Aeronautics and Astronautics*.

Bramwell, A. (2001). *Helicopter dynamics* (2nd ed.). Butterworth Heinemann.

Branlard, E. (2011). *Wind turbine tip-loss corrections.* Unpublished master's thesis, Technical University of Denmark.

Butler, R., Byerley, A., VanTreuren, K., & Baughn, J. (2001, APR). The effect of turbulence intensity and length scale on low-pressure turbine blade aerodynamics [Article]. *INTERNATIONAL JOURNAL OF HEAT AND FLUID FLOW*, *22*(2), 123-133. doi: 10.1016/S0142-727X(00)00081-3

Campfens, J. A. (2008). *Development and analysis of a coaxial helicopter model.* Unpublished master's thesis, Delft University of Technology.

Castles, W. J., & Durham, H. L. J. (1956, Dec). *Distribution of normal component of induced velocity in lateral plan of a lifting rotor* (Technical note No. 3841). National Advisory Comittee for Aeronautics.

Castles, W. J., & Leeuw, J. H. d. (1953a, March). *The normal component of the induced velocity in the vicinity of a lifting rotor and some examples of its application* (TN No. NACA TN 2912). Washington: Georgia Institute of Technology.

Castles, W. J., & Leeuw, J. H. d. (1953b). *The normal component of the induced velocity in the vicinity of a lifting rotor and som examples of its application* (Report No. 1184). National advisory committee for aeronautics.

Choi, C., & Yoo, J. (2000, SEP-OCT). Unsteady blade-row flow calculations using a low-reynolds-number turbulence model [Article]. *JOURNAL OF PROPULSION AND POWER*, *16*(5), 768-776. doi: 10.2514/2.5665

Coleman, C. P. (1997, March). *A survey of theoretical and experimental coaxial rotor aerodynamic research* (Tech. Rep. No. 3675). NASA.

Critzos, C. C., Heyson, H. H., & Boswinkle, R. W. J. (1955, January). *Aerodynamic characteristics of naca 0012 airfoil section at angels of attack from 0° to 180°* (Technical Note No. 3361). National Advisory Committee for Aeronautics. (ADA377080(v).pdf)

Dai, H., Luo, H., & Doyle, J. F. (2012, FEB 25). Dynamic pitching of an elastic rectangular wing in hovering motion. *JOURNAL OF FLUID MECHANICS*, *693*, 473-499. doi: 10.1017/jfm.2011.543

Daniel A. Griffiths, A. G. G. L. M., J. Gordon Leishman. (2002). A study of dual-rotor interference and ground effect using a free-vortex wake model. *American Helicopter Society International circulation*, *2*, 1–21.

Drela, M. (1989). *Xfoil: An analysis and design system for low reynolds number airfoils.* Spring-Verlag. (MIT)

Drela, M. (2015, 02). *Xfoil subsonic airfoil development system.* http://web.mit.edu/drela/Public/web/xfoil/.

DSE, g. (2011). *Guardian angels* (Tech. Rep.). TU-Delft,Faculteit L&R. (Winifred Schwegman, Marijn Hogeweg, Paolo Toffano, Ellen van den Oord, Monica Zeestraten, Tom Lotz, Sam Adriaenssens, Roeland Vester, David Zaccai, Peter Kreuk)

Felipe Bohorquez, J. S. D. P. L. R., Paul Samuel, & Perel, R. (2003, Apr). Design, analysis and hover performance of a rotary wing micro air vehicle. *Journal of the American Helicopter Society*, *48*(2), 80–90. (publisher=AHS International)

Foundation, G. H. H. (2017, January). *Coaxial benefits.* Retrieved from http://www.gyrodynehelicopters.com/coaxial_benefits.htm

Hein, B. R., & Chopra, I. (2007, JUL). Hover performance of a micro air vehicle: Rotors at low reynolds number [Article; Proceedings Paper]. *JOURNAL OF THE AMERICAN HELICOPTER SOCIETY*, *52*(3), 254-262. (International Specialists Meeting on Unmanned Rotorcraft - Design Control and Testing, Chandler, AZ, JAN 18-20, 2005)

Hermann Föttinger Institute, T. B. (2016, 02). *Q-blade.* www.q-blade.org.

H. W. Kim, R. E. B. K. D., A. R. Kenyon. (2009). Interaction aerodynamics and acoustics of a hingeless coaxial helicopter with an auxiliary propeller in forward flight. *The Aeronatical Journal*, *113*(1140), 65–78.

J.Schroeder, E. (2005). *Low reynolds number flow validation using computational fluid dynamics with application to micro air vehicles.* Unpublished master's thesis, University of Maryland.

Kim, J., & Koratkar, N. (2005, JUL-AUG). Effect of unsteady blade pitching motion on aerodynamic performance of microrotorcraf [Article]. *JOURNAL OF AIRCRAFT*, *42*(4), 874-881. doi: 10.2514/1.6732

Koehl, A. b., Rafaralahy, H., Boutayeb, M., & Martinez, B. (2012). Aerodynamic modelling and experimental identification of a coaxial-rotor uav. *Journal of Intelligent and Robotic Systems: Theory and Applications*, *68*(1), 53-68. Retrieved from http://www.scopus.com/inward/record.url?eid=2-s2.0-84865620335&partnerID=40&md5=322b (cited By (since 1996)0) doi: 10.1007/s10846-012-9665-x

Lakshminarayan, V. K., & Baeder, J. D. (2010, MAY-JUN). Computational investigation of microscale coaxial-rotor aerodynamics in hover [Article; Proceedings Paper]. *JOURNAL OF AIRCRAFT*, *47*(3), 940-955. (AIAA 47th Aerospace Sciences Meeting and Exhibit, Orlando, FL, JAN 05-08, 2009) doi: 10.2514/1.46530

Landgrebe, A. J. (1969, October). An analytical method for predicting rotor wake geometry. *Journal of the American Helicopter Society*, 20-32.

Landgrebe, A. J. (1971, June). *An analytical and experimental investigation of helicopter rotor hover performance and wake geometry characteristics.* (Tech. Rep. No. Tech. Rept 71-24). Fort Eustis, VA: USAAMRDL.

Landgrebe, A. J. (1972, October). The wake geometry of a hovering helicopter rotor and its influence on rotor performance. *Journal of American Helicopter Society*.

Landgrebe, A. J., Taylor, R. B., Egolf, T. A., & Bennett, J. C. (1982). Helicopter airflow and wake characteristics for low speed and hovering flight. *Journal of American Helicopter Society*.

Leishman, J. G., Ananthan, S., & Gordon, J. (2006). Aerodynamic optimization of a coaxial proprotor. In *Annual forum proceedings-american helicopter society* (Vol. 62, p. 64).

Liu, Y., Chen, J., & Xiao, Y. (2002). Mems microrotor technology and aerodynamics for a hovering micro air vehicle [Proceedings Paper]. In Jin, GF and McKillop, JS and Hane, KH (Ed.), *Mems/moems technologies and applications* (Vol. 4928, p. 139-147). 1000 20TH ST, PO BOX 10, BELLINGHAM, WA 98227-0010 USA: SPIE-INT SOC OPTICAL ENGINEERING. (Conference on MEMS/MOEMS Technologies and Applications, SHANGHAI, PEOPLES R CHINA, OCT 17-18, 2002) doi: 10 .1117/12.483163

Lopez-Garcia, O., Cuerva, A., & Esteban, S. (2012, MAY). Use of calculus of variations to determine the shape of hovering rotors of minimum power and its application to micro air vehicles [Article]. *PROCEEDINGS OF THE INSTITUTION OF MECHANICAL ENGINEERS PART G-JOURNAL OF AEROSPACE ENGINEERING*, *226*(G5), 574-588. doi: 10.1177/0954410011411636

MathWorks, T. (2015a, 2). *fminunc unconstrained minimization.* http://nl.mathworks.com/help/optim/ug/fminunc-unconstrained-minimization.html.

MathWorks, T. (2015b, 02). *Multi-objective goal attainment optimization.* http://nl.mathworks.com/help/optim/examples/multi-objective-goal-attainment-optimization.html.

MathWorks., T. T. (2015, 02). *Constrained nonlinear optimization algorithms.* http://nl.mathworks.com/help/optim/ug/constrained-nonlinear-optimization-algorithms.html.

Montgomerie, B. (2004, June). *Method for root effects, tip effects and extending the angle of attack range to $\pm 180°$, with application to aerodynamics for blades on wind tturbine and propellers* (Tech. Rep. No. ISSN 1650-1942). Swedisch Defence Research Agency. (FOI-R–1305–SE)

Morkovin MV, H. T., Reshotko E. (1994). Transition in open flow systemsa reassessment. *Bull. Am. Phys. Soc., 39:1882*.

Motazed, B., & Vos, D. (1998). Aerodynamics and flight control design for hovering micro air vehicles [Proceedings Paper]. In *Proceedings of the 1998 american control conference, vols 1-6* (p. 681-683). 345 E 47TH ST, NEW YORK, NY 10017 USA: IEEE. (American Control Conference, PHILADELPHIA, PA, JUN 24-26, 1998)

Nagashima, T. ., & Nakanishi, K. (1981). Optimum performance and wake geometry of coaxial rotor in hover. In *Proceedings of the 7th european rotorcraft and powered lift forum.*

Nagashima, T., & Nakanishi, K. (1983). Optimum performance and wake geometry of a coaxial rotor in hover. *Vertica*, *7*, 225–239.

Pavel, M. D. (2001). *On the necessary degrees of freedom for helicopter and wind turbine.* Unpublished doctoral dissertation, University of Technology Delft.

PETROSYAN, E. (2017, January). *Aerodynamic features of coaxial configuration helicopter.* Retrieved from https://web.archive.org/web/20071220021153/http://www.kamov.ru/market/news/petr11.ht

Prior, S. D. (2010, 03-01). Reviewing and investigating the use of co-axial rotor systems in small uavs. *International Journal of Micro Air Vehicles*, *Volume 2*(1), 1–16. Retrieved from http://multi-science.metapress.com/content/D8R70RV2N73RXNKM doi: 10.1260/1756-8293.2.1.1

Robotics, D. (2015, 08). *Copter — multirotor uav.* Retrieved from copter.ardupilot.com

Schafroth, D., Bermes, C., Bouabdallah, S., & Siegwart, R. (2010). Modeling, system identification and robust control of a coaxial micro helicopter. *Control Engineering Practice*, *18*(7), 700 - 711. Retrieved from http://www.sciencedirect.com/science/article/pii/S0967066110000390 (¡ce:title¿Special Issue on Aerial Robotics¡/ce:title¿) doi: http://dx.doi.org/10.1016/j.conengprac.2010.02.004

Sunada, S., Ohkura, A., Matsue, A., & Kawachi, K. (2004, MAY). Characteristics of rotary wings in hovering mode at an ultra-low reynolds number [Article]. *TRANSACTIONS OF THE JAPAN SOCIETY FOR AERONAUTICAL AND SPACE SCIENCES*, *47*(155), 59-65. doi: 10.2322/tjsass.47.59

Syal, M., & Leishman, J. (2012). Aerodynamic optimization study of a coaxial rotor in hovering flight. *Journal of the American Helicopter Society*, *57*(4), 1–15. Retrieved from http://www.scopus.com/inward/record.url?eid=2-s2.0-84868355184&partnerID=40&md5=c133 (cited By (since 1996)0 publisher=AHS International) doi: 10.4050/JAHS.57.042003

Techwinder. (2016, 02). *Xflr5.* ww.xflr5.com/xflr5.htm.

Timmer, W. A. (2010, June). Aerodynamic characteristics of wind turbine blade airfoils at high angle-of-attack. *The Science of Making Torque from Wind*, 71-78.

Truppel, M., & Rossi, L. (2011, OCT). Exploration of the rotational power consumption of a rigid flapping wing [Article]. *EXPERIMENTS IN FLUIDS*, *51*(4), 1085-1099. doi: 10.1007/s00348-011-1128-9

van Holten, T., & Melkert, J. (2002, November). *Helicopter performance, stability and control.* TU Delft.

Xu, H.-Y., & Ye, Z.-Y. (2010, September). Coaxial rotor helicopter in hover based on unstructured dynamic overset grids. *Journal of Aircraft*, *47*(5), 1820–1824. Retrieved from http://arc.aiaa.org/doi/abs/10.2514/1.C031079 doi: 10.2514/1.C031079

Zimmer, H. (1985). The aerodynamic calculation of counter rotating coaxial rotors. In *Proceedings of the 11th european rotorcraft and powered lift forum.* Sept.

Appendix A

Rotorcraft and Controller Parameters

A.1 Kamov 32A Parameters

```matlab
1  %% Ka—32 Model data
2
3  %% Simulation parameters
4  tau_lambda  = 0.1;                    % Time constant                    [s]
5
6  psitot = 90; %ODE blade simulation ??
7  x0 =[0,0]; %Start point ODE Simulation ??
8
9   coord.psiw = (0:1:360)*(pi/180);      %Discretization rotorwake ...
        calculations [rad]
10 coord.psi = (0:360/20:360)*(pi/180);   %Discretization rotation wise [rad]
11
12 rotor.method = 'Rectangular'; %Intergration method used for the rotorblades
13
14 % Timing enable/disable
15 TimeModel = 0;
16
17 %% General constants
18 g      = 9.80665; % Gravitational acceleration              [m/s^2]
19
20 element.gma = 1.4; %Heat capacity ration of air [—]
21 element.R = 287.058; %Specific gas constant to air [J/kg K]
22
23 element.C = 120; %Sutherland's constant for air [K]
24 element.T0 = 291.15; % reference temperature [K]
25 element.mu0 = 18.27e—6; %reference viscosity at reference temperature ...
      T0 [muPa s]
26
27 rotor.T = 293.15; %Ambiant air temperature in [K]
28 rotor.P = 101325; %Ambiant static pressure in [Pa]
29
30 %% Helicopter rotor data
31 Vtip       = 226;                    % Rotor tip speed [m/s]
32
33 c          = 0.48;                   % Rotor blade chord [m]
34 cc = c;
35 rotor.c = ones(size(coord.rad))*c; %local chord [m]
36
37 theta_tw    = degtorad(—6);          % Rotor blade linear twist [rad]
38 rotor.theta_tw    = degtorad(—6).*(coord.rad./R); %Local twist ...
      definition [rad]
39
```

```matlab
40  R            = 7.95;                    % Main rotor radius [m]
41  rr = 0.1:1/800:1;    %relative radius list tbv discretizaion radial wise [-]
42  coord.rad = R.*rr;   %Discretization radial wise [m]
43
44  I_beta       = 1280;                    % Rotor blade flap mom of inertia ...
        [kg*m^2]
45  Kbeta        = 33032;                   % Equivalent spring constant      ...
        [N*m/rad]
46  Omega        = 28.4277;                 % Angular velocity of rotor [rad/s]
47  Cla          = 5.73;                    % Main rotor liftgradient of NACA ...
        23012  [1/rad]
48  Nb           = 3;                       % Rotor number of blades [-]
49  Cd           = 0.01;                    % Approximated drag coefficient
50  h_nd         = 0.189;                   % Non-dimensional separation ...
        distance [-]
51  h0           = h_nd*R;                  % Separation distance [m]
52
53  % Determining positions of the rotors
54  xhu = 0;        % Hub x-position relative to cg [m]
55  yhu = 0;        % Hub y-position relative to cg [m]
56  zhu = 2.186+h0; % Hub z-position relative to cg [m]
57  rotorhub = 'central flapping hinges with spring'; %Inertia and ...
        mechanical behaviour of the rotorhub
58
59  xhl = 0;        % Hub x-position relative to cg [m]
60  yhl = 0;        % Hub y-position relative to cg [m]
61  zhl = 2.186;    % Hub z-position relative to cg [m]
62
63  % Rotor aerodynamic
64  dataname = 'Naca0012wind'; %Name of file with the aerodynamic data
65  dataadres = 'Airfoils/'; % Folder of the data tables
66  datanames =[dataadres dataname];
67  element.foilname = load(datanames);
68
69  %% Helicopter body
70  CDS     = 4;       % Eq. flat plate area                  [m^2]
71  K_fus   = 0.83;    % Correction coeff in fus pitching moment [-]
72  Vol_fus = 6.11;    % Equivalent volume of circular body      [m^3]
73
74  alpha0_hs = degtorad(-1.5);% Horizontal stabilizer incidence   [rad]
75  x_hs      = 8.92;        % Horizontal stabilizer x-positon rel to cg [m]
76  S_hs      = 1.335;       % Horizontal stabilizer area           [m^2]
77  Cla_hs    = 4;           % Horizontal stabilizer lift gradient     [1/rad]
78
79  beta0_fin = degtorad(-1); % Vertical fin incidence              [rad]
80  x_fin     = 8.563;     % Vertical fin x-position relative to cg [m]
81  z_fin     = 0;         % Vertical fin z-position relative to cg [m]
82  S_fin     = 1.395;     % Vertical fin area                 [m^2]
83  Cla_fin   = 4;         % Vertical fin lift gradient        [1/rad]
84
85  %% General helicopter parameters
86  m = 10000; % Helicopter mass    [kg]
87  W = m*g;   % Helicopter weight  [N]
88
89  Ixx = 9638;  % Helicopter moment of inertia about x-axis [kg*m^2]
90  Iyy = 33240; % Helicopter moment of inertia about y-axis [kg*m^2]
91  Izz = 25889; % Helicopter moment of inertia about z-axis [kg*m^2]
92  Jxz = 2226;  % Heli product of inertia about x & z-axis  [kg*m^2]
```

A.2   Walkera Lama Parameters

```
 1  TimeModel = 0;
 2
 3  %Helicopter data
 4  Vtip        = 56.28683125; %223.3;                    % Rotor tip speed ...
        [m/s] 283.2690
 5  c           = 0.0319;                    % Rotor blade chord [m]
 6  R           = 0.25;                    % Main rotor radius [m]
 7  I_beta      = 7.66e-4; %7.29e-7; -- 7.29e-5              % Rotor ...
        blade flap mom of inertia [kg*m^2]
 8  theta_tw    = degtorad(-6); %theta_tw    = -6*deg2rad;        % Rotor ...
        blade linear twist [rad]
 9  Kbeta       = 52730;                % Equivalent spring constant     ...
        [N*m/rad]
10  Omega       = 225.147325;              % Angular velocity of rotor [rad/s]
11  % 2000-2150 rpm
12  Cla         = 5.73;                % Main rotor liftgradient of NACA ...
        23012  [1/rad]
13  %Helicopter data
14  Nb          = 3;                %3 Rotor number of blades [-]
15
16  Cd          = 0.01;                % Approximated drag coefficient
17  h_nd        = 0.212766;   %80mms          % Non-dimensional ...
        separation distance [-]
18  h0          = h_nd*R;              % Separation distance
19  % Determining positions of the rotors
20  xhu = 0;        % Hub x-position relative to cg [m]
21  yhu = 0;        % Hub y-position relative to cg [m]
22  zhu = 0.105+h0; % Hub z-position relative to cg [m]
23  rotorhub = 'central flapping hinges with spring'; %'central flapping ...
        hinges with spring'; %'central flapping hinges';
24  %Form ka32data
25  xhl = 0;        % Hub x-position relative to cg [m]
26  yhl = 0;        % Hub y-position relative to cg [m]
27  zhl = 0.105;    % Hub z-position relative to cg [m]
28  %Helicopter data
29  CDS     = 0.08307; %0.8307;      % Eq. flat plate area ...
                        [m^2]
30  F0      = 0.83;  %
31  K_fus   = 0.0083;% 0.083;     % Correction coeff in fus pitching moment [-]
32  Vol_fus = 0.001; %0.001;   % Equivalent volume of circular body      [m^3]
33  alpha0_hs = degtorad(0);% Horizontal stabilizer incidence   [rad]
34  x_hs     = 0;       % Horizontal stabilizer x-positon rel to cg [m]
35  S_hs     = 0;      % Horizontal stabilizer area           [m^2]
36  Cla_hs   = 0;          % Horizontal stabilizer lift gradient     [1/rad]
37
38  beta0_fin = degtorad(0); % Vertical fin incidence              [rad]
39  x_fin    = 0;     % Vertical fin x-position relative to cg [m]
40  z_fin    = 0;         % Vertical fin z-position relative to cg [m]
41  S_fin    = 0;     % Vertical fin area                 [m^2]
42  Cla_fin  = 0;         % Vertical fin lift gradient          [1/rad]
```

```matlab
43  g       = 9.80665; % Gravitational acceleration              [m/s^2]
44
45  a = 1; % multipication factor
46  % General helicopter parameters
47  m = 0.800 ; %0.574 0.800; % Helicopter mass    [kg]
48  W = m*g;  % Helicopter weight  [N]
49
50  Ixx = 5.33e-3; %0.004;  % Helicopter moment of inertia about x-axis ...
        [kg*m^2]
51  Iyy = 6.26e-3; %0.004; % Helicopter moment of inertia about y-axis [kg*m^2]
52  Izz = 2.50e-3; %0.003; % Helicopter moment of inertia about z-axis [kg*m^2]
53  Jxz = -7.049e-6*0; %-7.049e-6;  % Heli product of inertia about x & ...
        z-axis  [kg*m^2]
54
55  tau_lambda  = 0.1;                    % Time constant              [s]
56  % tau_lambda = 1;
57
58  psitot = 90; %90 180 360
59  x0 =[0,0];
60  %%
61  cc = c;
62
63  %steps = [5 8 7]; (1)(2)(3)
64  % stepspsiw = 8;
65  stepspsi = 20;
66  stepsR = 20;
67
68   coord.psiw = (0:360/stepspsi:360)*(pi/180); %rotation angle 360 wake ...
         (360/360)
69   % coordinates
70  coord.psi = (0:360/stepspsi:360)*(pi/180); %(0:18:360)*(pi/180); ...
        %rotation angle (360/20)
71  % coord.rad = 0.1:R/800:R; %0:0.3975:R; 0.1:R/800:R (R/800)
72
73  rr = 0.1:1/stepsR:1; %relative radius 800 400 200 100 50 25 20 10
74  coord.rad = R.*rr;
75
76  rotor.c = ones(size(coord.rad))*c; %local chord [m]
77  % rotor.theta_tw = ones(size(coord.rad))*degtorad(-6); % ...
        ones(size(rad))*degtorad(-1); %constant twist
78  rotor.theta_tw   = degtorad(-6).*(coord.rad./R); %linear twist
79
80  rotor.method = 'Rectangular'; %'trapazoidal'; %'Rectangular';
81  rotor.T = 293.15; %temerature in K
82  rotor.P = 101325; %total pressure in Pa
83
84  element.gma = 1.4; %air
85  element.R = 287.058; %specific to air
86
87  element.C = 120; %K
88  element.T0 = 291.15; %K
89  element.mu0 = 18.27e-6; %muPa s
90
91  dataname = 'Naca0012wind'; %'Naca0012CoefWindRefExt'; % ...
        'Naca0012CoefWindRef';
92  dataadres = 'Airfoils/';
93  datanames =[dataadres dataname];
94  element.foilname = load(datanames);
```

A.3 Guardian Angles Parameters

```matlab
1  %% Guardian Angel MAV data
2
3  %% Simulation parameters
4  tau_lambda  = 0.1;                    % Time constant                [s]
5
6  psitot = 90; %ODE blade simulation ??
7  x0 =[0,0]; %Start point ODE Simulation ??
8
9   coord.psiw = (0:1:360)*(pi/180); %Discretization rotorwake ...
       calculations [rad]
10 coord.psi = (0:360/20:360)*(pi/180);  %Discretization rotation wise [rad]
11
12 rotor.method = 'Rectangular'; %Intergration method used for the rotorblades
13
14 % Timing enable/disable
15 TimeModel = 0;
16
17 %% General constants
18 g       = 9.80665; % Gravitational acceleration         [m/s^2]
19
20 element.gma = 1.4; %Heat capacity ration of air [-]
21 element.R = 287.058; %Specific gas constant to air [J/kg K]
22
23 element.C = 120; %Sutherland's constant for air [K]
24 element.T0 = 291.15; % reference temperature [K]
25 element.mu0 = 18.27e-6; %reference viscosity at reference temperature ...
       T0 [muPa s]
26
27 rotor.T = 293.15; %Ambiant air temperature in [K]
28 rotor.P = 101325; %Ambiant static pressure in [Pa]
29
30 %% Helicopter rotor data
31 Vtip        = 223.3;                  % Rotor tip speed [m/s]
32
33 c           = 0.0157;                 % Rotor blade chord [m]
34 cc = c;
35 rotor.c = ones(size(coord.rad))*c; %local chord [m]
36
37 theta_tw    = degtorad(-6); % Rotor blade linear twist [rad]
38 rotor.theta_tw   = degtorad(-6).*(coord.rad./R); %Local twist ...
       definition [rad]
39
40 R           = 0.123;                  % Main rotor radius [m]
41 rr = 0.1:1/800:1; %relative radius list tbv discretizaion radial wise [-]
42 coord.rad = R.*rr; %Discretization radial wise [m]
43
44 I_beta      = 7.29e-7;                % Rotor blade flap mom of ...
       inertia [kg*m^2]
45 Kbeta       = 52730;                  % Equivalent spring constant    ...
       [N*m/rad]
```

```
46  Omega       = 2303.83461;                % Angular velocity of rotor [rad/s]
47  Cla         = 5.73;                       % Main rotor liftgradient of NACA ...
        23012  [1/rad]
48  Nb          = 3;                          %3 Rotor number of blades [−]
49  Cd          = 0.01;                       % Approximated drag coefficient
50  h_nd        = 0.212766;                   % Non−dimensional separation ...
        distance [−]
51  h0          = h_nd*R;                     % Separation distance
52
53  % Determining positions of the rotors
54  xhu = 0;          % Hub x−position relative to cg [m]
55  yhu = 0;          % Hub y−position relative to cg [m]
56  zhu = 0.105+h0;   % Hub z−position relative to cg [m]
57  rotorhub = 'central flapping hinges with spring'; %Inertia and ...
        mechanical behaviour of the rotorhub
58
59  xhl = 0;          % Hub x−position relative to cg [m]
60  yhl = 0;          % Hub y−position relative to cg [m]
61  zhl = 0.105;      % Hub z−position relative to cg [m]
62
63  % Rotor aerodynamic
64  dataname = 'Naca0012wind'; %Name of file with the aerodynamic data
65  dataadres = 'Airfoils/'; % Folder of the data tables
66  datanames =[dataadres dataname];
67  element.foilname = load(datanames);
68
69  %% Helicopter body
70  CDS     = 0.8307;   % Eq. flat plate area                        [m^2]
71  K_fus   = 0.083;    % Correction coeff in fus pitching moment [−]
72  Vol_fus = 0.001;    % Equivalent volume of circular body      [m^3]
73
74  alpha0_hs = degtorad(0);   % Horizontal stabilizer incidence   [rad]
75  x_hs     = 0;             % Horizontal stabilizer x−positon rel to cg [m]
76  S_hs     = 0;             % Horizontal stabilizer area                ...
        [m^2]
77  Cla_hs   = 0;             % Horizontal stabilizer lift gradient    ...
        [1/rad]
78
79  beta0_fin = degtorad(0); % Vertical fin incidence                  [rad]
80  x_fin    = 0;            % Vertical fin x−position relative to cg [m]
81  z_fin    = 0;            % Vertical fin z−position relative to cg [m]
82  S_fin    = 0;            % Vertical fin area                      [m^2]
83  Cla_fin  = 0;            % Vertical fin lift gradient             [1/rad]
84
85  %% General helicopter parameters
86  m = 0.574; % Helicopter mass   [kg]
87  W = m*g;   % Helicopter weight  [N]
88
89  Ixx = 0.004;    % Helicopter moment of inertia about x−axis [kg*m^2]
90  Iyy = 0.004;    % Helicopter moment of inertia about y−axis [kg*m^2]
91  Izz = 0.003;    % Helicopter moment of inertia about z−axis [kg*m^2]
92  Jxz = −7.049e−6; % Heli product of inertia about x & z−axis  [kg*m^2]
```

Appendix B

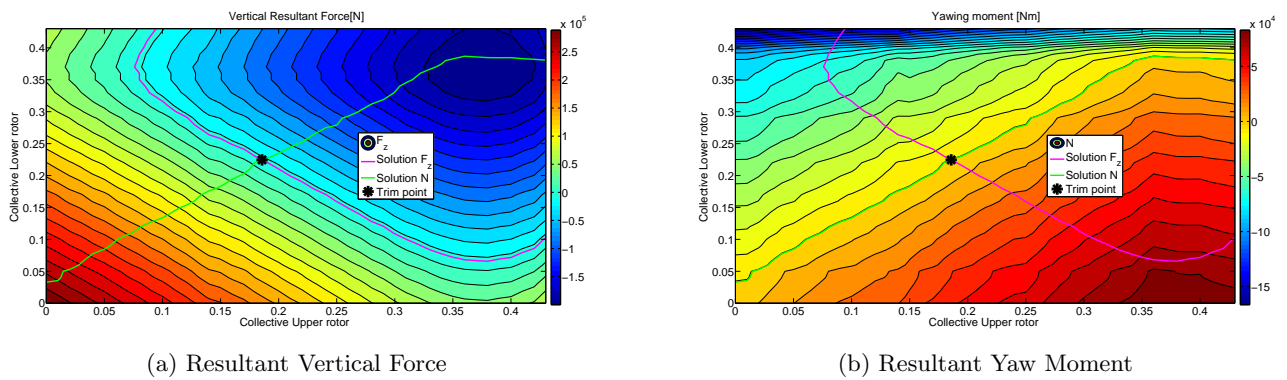# Remainder Results

B.1 Sweep Calculation Results Kamov 32A

(a) Resultant Vertical Force

(b) Resultant Yaw Moment

Figure B.1: Response to Collective changes

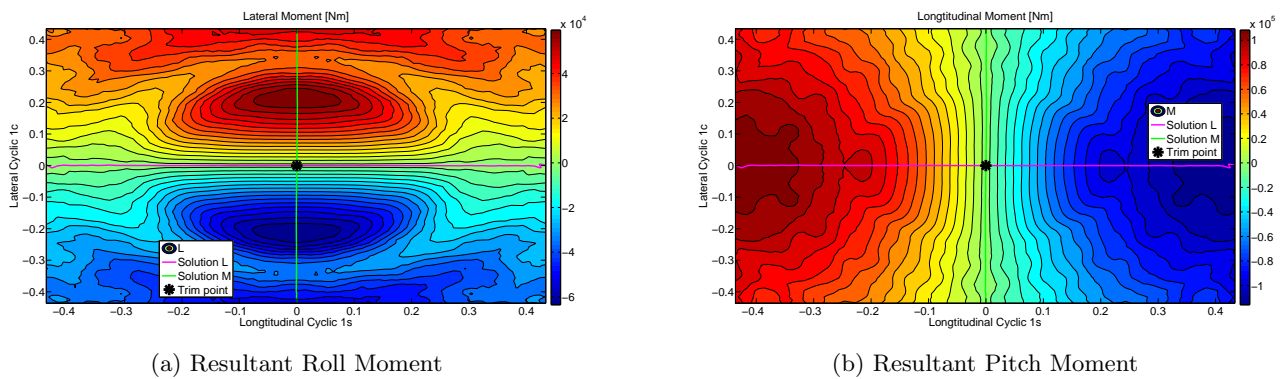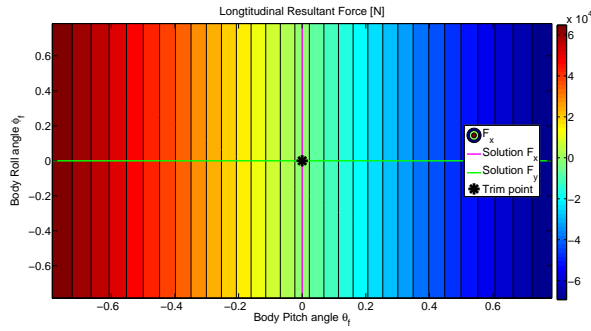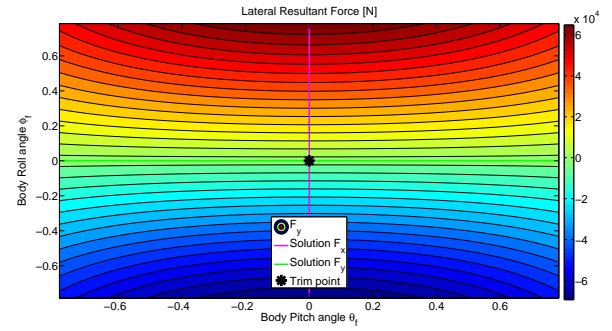(a) Resultant Roll Moment

(b) Resultant Pitch Moment
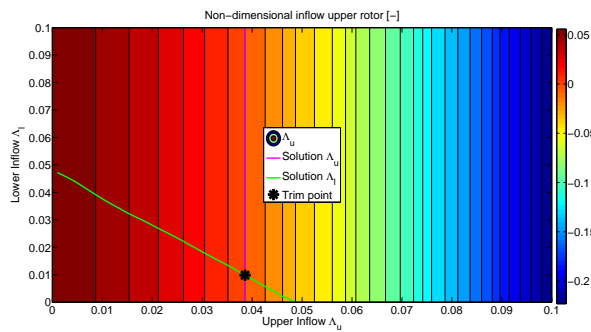
Figure B.2: Response to Cyclic changes
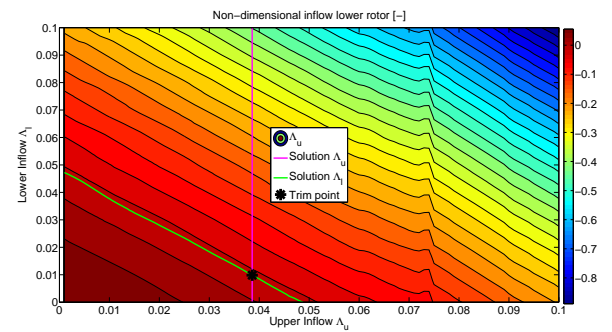
(a) Resultant Longtitudinal Force
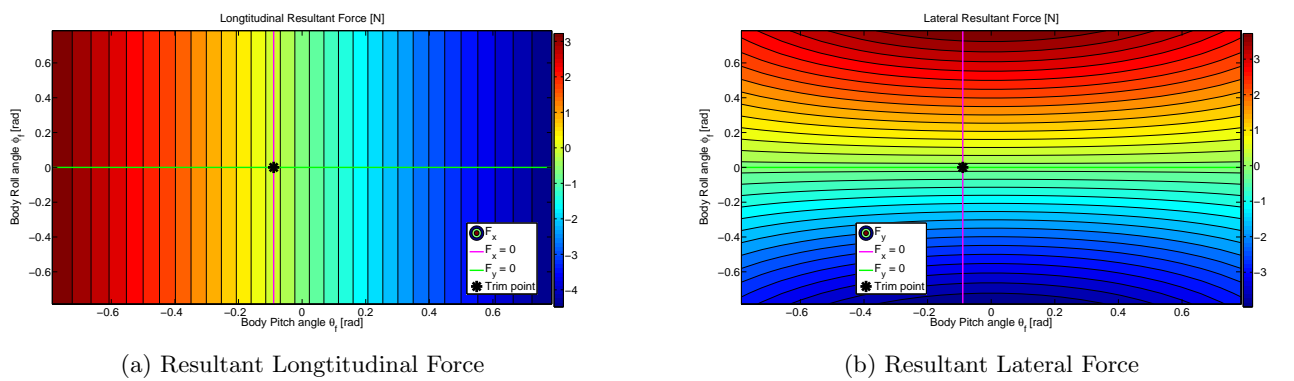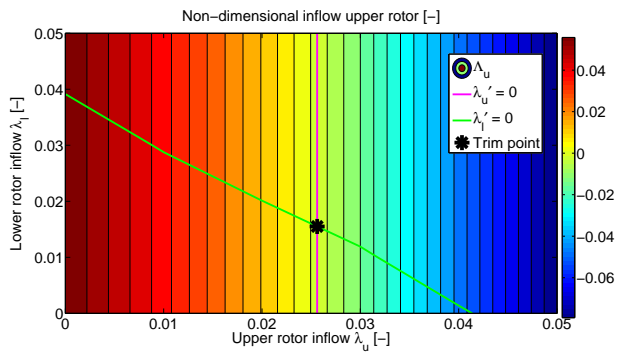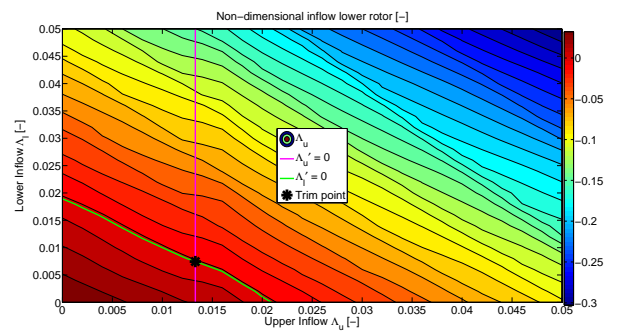
(b) Resultant Lateral Force

Figure B.3: Response to Body rotation changes

(a) Upper rotor induced velocity change

(b) Lower rotor induced velocity change

Figure B.4: Response to induced velocity changes

B.2   Sweep Calculation Results Guardian Angle MAV with increased blade moment of inertia

(a) Resultant Vertical Force

(b) Resultant Yaw Moment
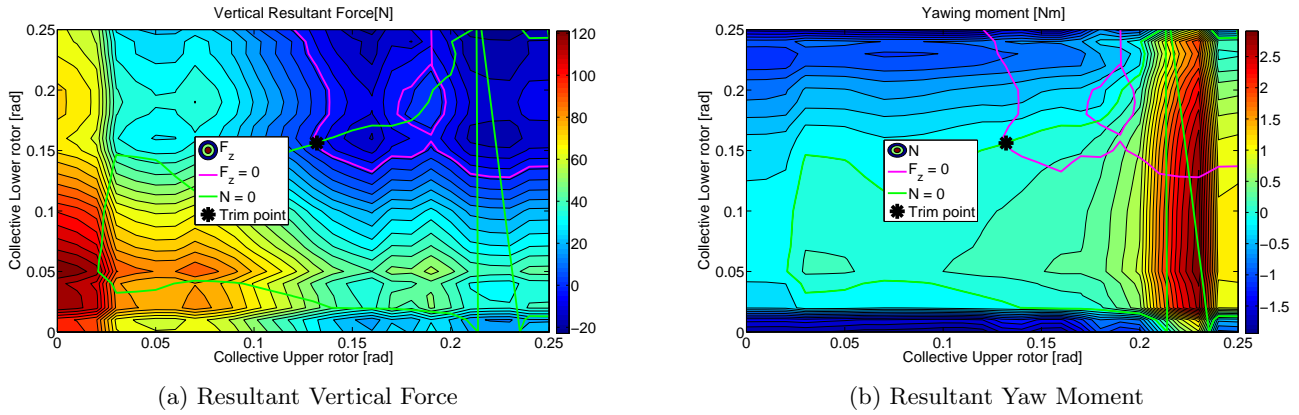
Figure B.5: Response to Collective changes

(a) Resultant Roll Moment

(b) Resultant Pitch Moment
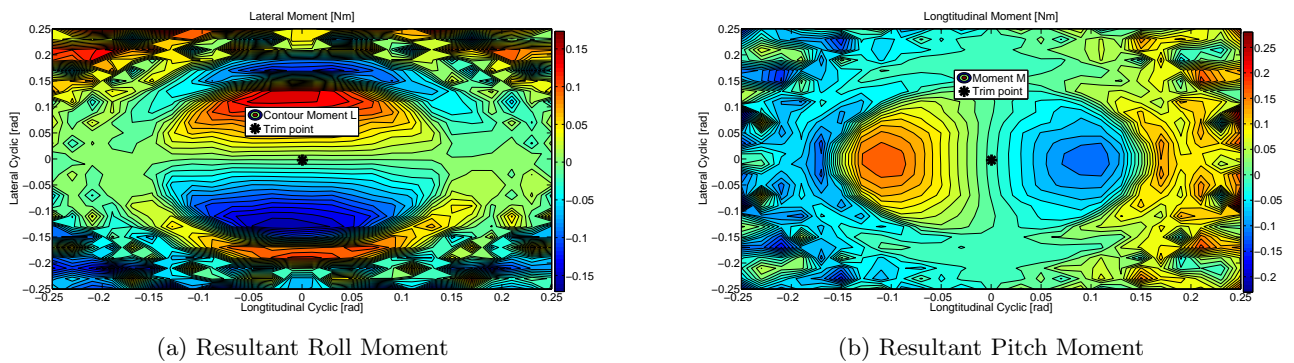
Figure B.6: Response to Cyclic changes

(a) Resultant Longtitudinal Force

(b) Resultant Lateral Force

Figure B.7: Response to Body rotation changes

(a) Upper rotor induced velocity change   (b) Lower rotor induced velocity change

Figure B.8: Response to induced velocity changes

Appendix C

Description of Code Modules

C.1 Start Up

This module starts with making an inventory of the state vector and the control inputs. These values are then assigned to there individual variables to be used by other parts of the model. First the individual states are made from the state vector, then the control angles are assigned. This process is repeated with every call to the model, to ensure the updating of these variables.

First the state and controls are separated from each other. The states are the first fourteen and the controls are the last four of the input vector. Then the variables are assigned from the values in this vector.

The non-dimensional induced velocity changes that were experimented with have a large influence on the size of the state vector. In the initial case there is one value for the entire rotor disk the induced velocities are found in position 13 and 14. Defining the induced velocity in rings using the standard discretization leads to a induced velocity vector of 21 numbers. This leads to the expansion of the state vector to 56. The last step was to also make the induced velocity depended on the azimuth angle of the blade. This means, using the standard discretization, that the induced velocity increases to a 21x21 matrix. The size of the state vector increases to 895 positions. The increasing length of the state vector had much more detrimental effects on the calculation time than the assumed benefits of getting a faster solution for the momentum calculations.

The database for the aerodynamics data although not part of the start up routine is described here. This is due to the database being part of the data management. The airfoil database is made up of a grid defined by three values. These are the angle of attack α, the Reynolds number Re and the Mach number M. A spacial representation of this look-up table can be found in figure C.1. The lift and drag for that specific condition are stored at each corresponding location. The database can be made from windtunnel test with the limits inherent to testing as well as results from calculation methods with its own limitations. Most calculation methods found use some form of linear airfoil theory for the calculation of lift and drag at large angles of attack, with (Montgomerie, 2004) as an example.

Next the general variables are calculated for use in the model. These are the normalized velocities in there respective direction x, y and z as are shown in equation C.3. The velocities are normalized with the tip speed which is calculated by multiplying the rotation
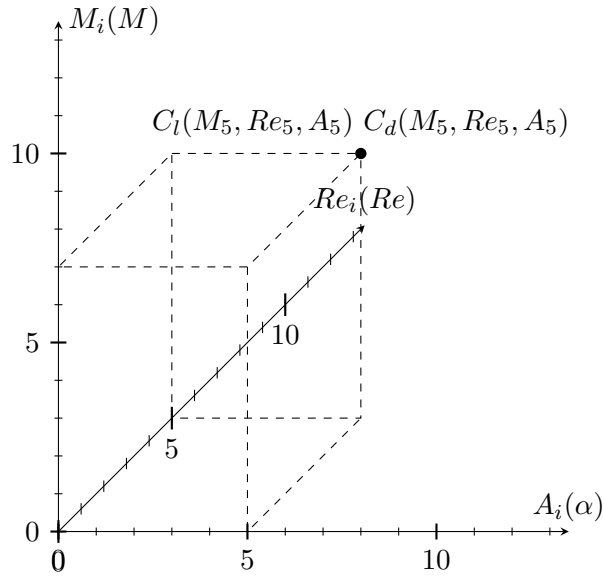
Figure C.1: Look-up table set up

rate with the radius of the rotor as can be seen in equation C.4.

$$\mu_x = \frac{u}{V_{tip}} \tag{C.1}$$

$$\mu_y = \frac{v}{V_{tip}} \tag{C.2}$$

$$\mu_z = \frac{w}{V_{tip}} \tag{C.3}$$

$$V_{tip} = \Omega \cdot R \tag{C.4}$$

The air density is calculated using the ideal gas equation and is shown in C.5. The blade lock number is calculated to be used in the flapping motion equations. It is an important parameter showing the relation between the aerodynamic forces and the inertia. The function used to define this number is shown in equation C.6 The angle of attack of the control plane is also of general importance as the control plane is one of the reference frames used in the rotor calculations. It is calculated as the sum of the control angle and the angle of the incoming flow as is shown in equation C.7. The advance ratio of the rotor is another parameter calculated to show in which part of the flight spectrum the rotorcraft is flying. It relates the forward motion of the rotorcraft to the percentage of reversed flow on the retreating side. The calculation is done by dividing the forward velocity by the tip speed of the rotor as is shown in equation C.8.

$$\rho = \frac{p}{R \cdot T} \tag{C.5}$$

$$\gamma = \frac{\rho \cdot c_{l\alpha} \cdot c \cdot R^2}{I_\beta} \tag{C.6}$$

$$\alpha_{cp} = -\arctan(\frac{u}{w}) + \theta_{1s} \tag{C.7}$$

$$\mu = \frac{V}{V_{tip}} \tag{C.8}$$

For the flapping motion the non-rotating blade flapping natural frequency has to be calculated also the non-dimensional rotating flapping frequency has to be calculated which uses the non-rotating natural frequency. Both equations used to calculate these natural frequencies are shown in equations C.9 and C.10.

$$\omega_b = \sqrt{\frac{\frac{k_\beta}{I_\beta}}{\Omega}} \tag{C.9}$$

$$\upsilon_b = \sqrt{1 + \omega_b^2} \tag{C.10}$$

Finally a general factor is defined that is used to make forces dimensionless. The forces are made non dimensional by calculating the dynamic pressure at a reference velocity here assigned as the tip speed multiplied by an reference area as is shown in equation C.11

$$dimless = \rho \cdot V_{tip}^2 \cdot \pi \cdot R^2 \tag{C.11}$$

The last step is to check if the flight regime and the known limits are not violated and if so display a warning. The two most notable are the tip Mach tip number of the advancing blade and the minimum value for the advance ratio. The warnings for maximum forward velocity is displayed at $M_{tip} = 0.85$ and the lower limit warning is displayed when $\mu = 0.4$ or lower as described in (van Holten & Melkert, 2002).

C.2   Helicopter forces

In this part the calculations are explained for the non-rotor forces. These are separated into three parts: The fuselage forces, the forces on the horizontal tail or stabilizer and the forces on the vertical tail or Fin. These forces are calculated using functions derived from empirical data.

The drag force produced by the fuselage is calculated using an estimated drag area $C_D S$ defined in the input of the model. The drag force can then be calculated using the standard function and the dynamic pressure as is shown in equation C.13. For the equations of

motion it is important to know the x, y and z components of this force as well as the moment it generates. For this the angle of attack at the fuselage is required, this is calculated using equation C.12. Than using Trigonometry the force in x and z direction can be calculated as is shown in equations C.14 and C.15. The moment generated is then calculated using the fuselage volume, which is estimated, leading to equation C.16 for the resulting moment.

$$\alpha_{fus} = \arctan(\frac{u}{w}) \tag{C.12}$$

$$D_{fus} = \frac{1}{2}\rho V^2 \cdot C_D S \tag{C.13}$$

$$X_{fus} = -D_{fus} \cdot \cos(\alpha_{fus}) \tag{C.14}$$

$$Z_{fus} = -D_{fus} \cdot \sin(\alpha_{fus}) \tag{C.15}$$

$$M_{fus} = \rho \cdot V^2 k_{fus} \cdot Vol_{fus} \cdot \alpha_{fus} \tag{C.16}$$

The forces of the horizontal stabilizer are calculated using the local angle of attack α_{hs} and velocity V_{hs} at the tail as well as the surface area S_{hs} and lift curve slope $C_{l\alpha_{hs}}$ of the tail surface. The angle of attack for the horizontal tail is calculated by adding the fixed angle for the surface to the one from the incoming flow were the vertical part of the velocity is extended by the tail arm and rotation rate of the rotorcraft, which leads to equation C.17. The same principle is applied to the velocity calculation in C.18. The tail force can then be calculated using C.19 and the moment is this force times the tail arm as is shown in equation C.20.

$$\alpha_{hs} = \alpha_{0hs} + \arctan(\frac{u}{w + q \cdot x_{hs}}) \tag{C.17}$$

$$V_{hs} = \sqrt{u^2 + (w + q \cdot x_{hs})^2} \tag{C.18}$$

$$Z_{hs} = \frac{1}{2}\rho V_{hs}^2 \cdot 0.65 \cdot S_{hs} \cdot C_{l\alpha_{hs}} \cdot \alpha_{hs} \tag{C.19}$$

$$M_{hs} = Z_{hs} \cdot x_{hs} \tag{C.20}$$

The last surface to be calculated is the vertical tail. The same reasoning is applied for the side slip angle and velocity as for the horizontal tails angle of attack C.17 and velocity C.18. This leads to a side slip angle as expressed in C.21 and a velocity calculated by C.22. The force on the fin can then be calculated as shown in equation C.23 using the surface area of the fin S_{fin} and the lift curve slope as defined. The moments can then be calculated using this force and the respective arms to the centre of gravity as shown in equations C.24 and C.25.

$$\beta_{fin} = \beta_{0fin} + \arctan(\frac{u}{v - r \cdot x_{fin} + p \cdot z_{fin}}) \tag{C.21}$$

$$V_{fin} = \sqrt{u^2 + (v - r \cdot x_{fin} + p \cdot z_{fin})^2} \tag{C.22}$$

$$Y_{fin} = \frac{1}{2}\rho \cdot V_{fin}^2 \cdot S_{fin} \cdot C_{l\alpha fin} \cdot \beta_{fin} \tag{C.23}$$

$$L_{fin} = z_{fin} \cdot Y_{fin} \tag{C.24}$$

$$N_{fin} = -x_{fin} \cdot Y_{fin} \tag{C.25}$$

C.3 Equations of Motion

The equations of motion are calculated by summing all forces and moments and then using Newtons law $F = m \cdot a$ to calculate the rate change of the velocities, rotational as well as translational to be able and calculate the situation for the next time step.

The first thing that is done is summing the forces calculated for the upper and lower rotor in 2.2.3 and the body forces in C.2. For the x-direction this means summing the results of 2.78 for the upper and lower rotor as well as the result C.14 for the fuselage force. In the y-direction the sum is for the results of 2.79 and the fin C.23. The vertical direction has two additional forces next to the rotors 2.80. These are the fuselage force C.15 and the horizontal tail C.19.

$$X = X_u + X_l + X_{fus} \tag{C.26}$$

$$Y = Y_u + Y_l + Y_{fin} \tag{C.27}$$

$$Z = Z_u + Z_l + Z_{fus} + Z_{hs} \tag{C.28}$$

To be able to calculate the accelerations all forces have to be added. The force of gravity still has to be added to the forces generated by the body as shown in equation C.26 to C.28. The gravity force is incorporated into the forces in the body reference frame according to (Pavel, 2001). This leads to the forces in X,Y and Z direction as shown in equations C.29 to C.31 respectively. The result of equation C.32 is the weight component in Z direction and is calculated to compare the lift and weight.

$$F_x = -W \cdot \cos(\theta) + X \tag{C.29}$$

$$F_y = W \cdot \cos(\theta) \cdot \sin(\phi) + Y \tag{C.30}$$

$$F_z = W \cdot \cos(\theta) \cdot \cos(\phi) + Z \tag{C.31}$$

$$W_e = W \cdot \cos(\theta) \cdot \cos(\phi) \tag{C.32}$$

The moments generated by the various parts of the rotorcraft are then summed just like the forces were done in C.26 to C.28. This leads to C.33 for the moment around the

Z-axis which includes the results of the rotordisk 2.81 and the fin C.24. The moment around the y-axis is made up of the results from the rotor disk 2.82, C.16 for the fuselage and C.20 for the horizontal tail. The result is C.34. The moment around the x-axis has only rotor disk contributions 2.83 and is shown in C.35.

$$L = L_u + L_l + L_{fin} \tag{C.33}$$
$$M = M_u + M_l + M_{fus} + M_{hs} \tag{C.34}$$
$$N = N_u + N_l \tag{C.35}$$

Now using the resulting forces calculated in equations C.29 to C.31 and the mass of the rotorcraft the accelerations in x C.36, y C.37 and z C.38 direction can be calculated according to (van Holten & Melkert, 2002). The extra terms of the velocities u, v, w times the rotation rates p, q, r are the resulting accelerations in the direction perpendicular to those two motions.

$$\dot{u} = \frac{F_x}{m} - (q \cdot w + r \cdot v) \tag{C.36}$$

$$\dot{v} = \frac{F_y}{m} - (r \cdot u + p \cdot w) \tag{C.37}$$

$$\dot{w} = \frac{F_y}{m} - (p \cdot v + q \cdot u) \tag{C.38}$$

The rotational accelerations can be described by the sum of the angular momentum and the Moments(torque) divided by the mass moment of inertia as taken for the correct reference axes as seen in (Pavel, 2001). This results in C.39 to C.41.

$$\dot{p} = \frac{(I_{yy} \cdot I_{zz} - I_{zz}^2 - J_{xz}^2) \cdot r \cdot q + (I_{xx} - I_{yy} + I_{zz}) \cdot J_{xz} \cdot p \cdot q + I_{zz} \cdot L + J_{xz} \cdot N}{I_{xx} \cdot I_{zz} - J_{xz}^2} \tag{C.39}$$

$$\dot{q} = \frac{M + (I_{zz} - I_{xx}) \cdot p \cdot r \cdot J_{xz} \cdot (r^2 - p^2)}{I_{yy}} \tag{C.40}$$

$$\dot{r} = \frac{(I_{xx}^2 - I_{xx} \cdot I_{yy} + J_{xz}^2) \cdot p \cdot q - (I_{xx} - I_{yy} + I_{zz}) \cdot J_{xz} \cdot q \cdot r + J_{xz} \cdot L + I_{xx} \cdot N}{(I_{xx} \cdot I_{zz} - J_{xz}^2)} \tag{C.41}$$

The change rate of the Euler 'body' angles can then be composed from the rotation rates in the body reference frame and those same Euler angles. The resulting equations C.42 to C.44 are taken from (Pavel, 2001; Campfens, 2008).

$$\dot{\psi} = \frac{q \cdot \sin(\phi) + r \cdot \cos(\phi)}{\cos(\theta)} \tag{C.42}$$

$$\dot{\theta} = q \cdot \cos(\phi) - r \cdot \sin(\phi) \tag{C.43}$$

$$\dot{\phi} = p + \dot{\psi} \cdot \sin(\theta) \tag{C.44}$$

The velocities of the rotorcraft in the earth fixed reference frame can also be calculated using the velocities in the body reference frame and the Euler angles. Also these transformations were taken from (Campfens, 2008; Pavel, 2001) and are shown in equations C.45 to C.47.

$$\dot{x} = (u\cos(\theta) + (v \cdot \sin(\phi) + w \cdot \cos(\phi)) \cdot \sin(\theta)) \cdot \cos(\psi) - (v \cdot \cos(\phi) - w \cdot \sin(\phi)) \cdot \sin(\psi) \tag{C.45}$$

$$\dot{y} = (u \cdot \cos(\theta) + (v \cdot (\phi) + w \cdot \cos(\phi)) \cdot \sin(\theta)) \cdot \sin(\psi) + (v \cdot \cos(\phi) - w \cdot \sin(\phi)) \cdot \cos(\psi) \tag{C.46}$$

$$\dot{z} = -u \cdot \sin(\theta) + (v \cdot \sin(\phi) + w \cdot \cos(\phi)) \cdot \cos(\theta) \tag{C.47}$$

The non dimensional induced velocity Λ_0 is as already stated in the C.1 a state variable. The change of these state variables is the reason for these two equations. They calculate the quasi-dynamic inflow as stated in (Pavel, 2001)/(van Holten & Melkert, 2002) and can be seen in C.48 for the upper rotor and C.49 for the lower rotor. The change rate can be tuned using a chosen time constant τ.

$$\dot{\Lambda}_{0up} = \frac{C_{Tu} - C_{tglu}}{\tau_\lambda} \tag{C.48}$$

$$\dot{\Lambda}_{0low} = \frac{C_{Tl} - C_{tgll}}{\tau_\lambda} \tag{C.49}$$

C.4 Matlab Methods

C.4.1 Unconstrained Minimization

The *Find minimum of unconstrained multi variable function* is the first of three used matlab optimizers from the optimization toolbox. This function uses a non-linear solver to find the minimum specified by C.50.

$$\overset{min}{x} f(x) \tag{C.50}$$

The function $f(x)$ should return a scalar value while the input x can be a vector or a matrix. More information can be found in the Matlab documentation (MathWorks, 2015a).

The general steps taken to obtain a solution using this solver are the definition of the objective function. This is implemented by using the defined function as described in 2.4.2. Some variations on the input were tried. This includes the chosen the optimization algorithm both the *quasi-newton* and *thrust-region* were used. Also the termination tolerances on for the function value and the input values was reduced from the standard $1e^{-6}$ to 0.1.

C.4.2   Constrained Non-linear Optimization Algorithms

For the constrained minimization the problem can be specified just like in the uncon-strained case in C.4.1 with the addition of the definition of the constrains on the allowable input x. The constrains that can be used vary from a non-linear constrain function C.51 to a simple imposed boundary like C.55.

$$c(x) \leq 0 \tag{C.51}$$
$$ceq(x) = 0 \tag{C.52}$$
$$A \cdot x \leq b \tag{C.53}$$
$$Aeq \cdot x = beq \tag{C.54}$$
$$lb \leq x \leq ub \tag{C.55}$$

More information about this method can be found in the matlab documentation (Math-Works., 2015).

The algorithms algorithms that were used were *thrust-region-reflective*,*active-set* and *interior-point*. The constrains applied here are in essence box constrains on the input values, by means of an upper and lower bound on the x vector. The tolerances were also here increased to a value of 0.1.

C.4.3   Multi-Objective Goal Attainment Optimization

The multi-objective goal attainment optimization solves a problem specified by C.56.

$$\underset{x,y}{minimize}\, \gamma \tag{C.56}$$

To be able to use γ the relation to the objective function needs to be specified. This can be seen in C.57.

$$F(x) - weight \cdot \gamma \leq goal \tag{C.57}$$

This is next to the in C.4.2 defined constrains.

The first solve is a matlab solver called fgoalattain for this a lower and upper bound is required to be defined. The goal to attain is set on a zero vector, all with equal weight.

To help the solver find a solution the tolerances on the function value as well as the input was relaxed from $1e^{-6}$ to 0.1. A comlete description can be found in the Matlab description (MathWorks, 2015b).

Verification of the Code Modules

The general input for the model is the state of the rotorcraft it self(control angles, weights/inertia, geometry) and the environment(motion of the rotorcraft with respect to the environment, temperature, pressure). The model is made with the top down method in mind. Make a general model, of a coaxial rotorcraft then apply it to different situations.

This starts with the assumption that the numerical model can be made using the same functions as were used for the analytical model. Thus calculating the solution numerically using as little simplifications as possible, while still using the same base functions used by the analytical model.

The analytical model uses a single lift curve slope and zero lift drag to calculate the rotor forces.

For the numerical modelling the assumptions concerning the changed parts are tried to be the same as for the analytical version. The calculations for the rotor-blades are made using a discretized mesh(r, ψ) to look-up the lift and drag coefficients at these points. The forces can then be integrated over the rotor-blade to get the force on the blade at that rotational station. For the trim calculation this is then integrated over one rotation and averaged.

There are also changes to the attenuation calculations. The wake is still being prescribed using the same function by (Castles & Leeuw, 1953a) and (Landgrebe, 1971) but instead of using one value inside the wake and one outside the wake, the attenuation is calculated for each point in the discretized mesh for the rotor.

The model can be divided into a specified number of sections.

Start-up General calculation and definition of constants and values to be used by the model.

Flapping Motion ODE Calculation of the flapping motion using the differential equation.

Flapping Motion Analytical Calculation of the flapping motion using the analytical method used in (Campfens, 2008).

Rotor Forces Calculation of the forces on the Rotor blades using a look-up table and the current state.

Wake Calculation or definition of the outline of the rotor wake influence area. Base to use a prescribed wake as described in (Landgrebe, 1971).

Attenuation The Calculation of the attenuation matrix at a specific distance from the upper rotor. This is done using the functions described by (Castles & Leeuw, 1953a).

Body Forces Calculation of the body forces, this includes the forces generated by the vertical and horizontal tail of the helicopter if present.

Equation of Motion The definition of the equation of motion to describe the motion based on the previously calculated forces.

D.1   Initial limits and Deficiencies

Developing the model(parts) as described in 2 and C made it clear that the assumption to use an airfoil database to determine the aerodynamic forces, would lead to additional difficulties. The special conditions for the airfoil data are that it has to include values at high angles of attack α which is difficult to find. The data that was found on this subject came from the field of wind turbines. And as is shown in (Timmer, 2010) not very accurate as the results for the NACA0012 airfoil leads to a number of solutions.

One of the goals was to scale the rotorcraft down. This lead to the problem of obtaining a suitable database at low Reynolds number flow, which is even more difficult.

Due to the difficulties of obtaining a test based database the possibility to calculate the database was explored. The search lead to codes like 'Xfoil'(Drela, 1989) and 'XFLR5' (Techwinder, 2016), to calculate the lift, drag and moment coefficient for the 2d airfoils. The limits of the codes are known although the results were deemed to be better than the average coefficients(especially at higher angles of attack). The initial though was that angles of attack up to 45° would be large enough. Running the model turned out that for a few cases ,especially the inboard rotor, the angles of attack could increase beyond the vertical.

The data provided by wintunnel tests and/or calculations codes like X-foil can be extended to be used for a full 180° as is shown in (Montgomerie, 2004).

Two methods came out for extrapolation the results. These are the 'Montgomery' and 'Viterna-Corrigan' post stall models as used by the windtunnel industry. Both methods are incorporated in the Qblade code (Hermann Föttinger Institute, 2016) for calculating windtunnel rotorblades.

D.1.1   Airfoil database

Generally it was difficult to find airfoil data that was usable to model the aerodynamics with the applied limits of increased angles of attack and low Reynolds numbers. The other requirement is that for the results the Mach - and Reynolds number have to be known as well as the angel of attack, which is not always the case.

The alternative that has been explored is: to use numerical codes to provide the data. This was difficult as the codes available from the 'simple' Xfoil to the extensive CFD codes, either take long times to calculate or are not accurate enough. Initially a database was made using Xfoil to start testing the basic connections within the model as well as

being able to calculate the range of Mach and Reynolds numbers seen by the rotorblades. Used to determine the range for the look-up tables.

D.1.2 Lift and Drag data at the extremes

The result of the range for the look-up tables was that the aerodynamic data that was desired was to have data in the full range of angles of attack(360°) at low Reynolds numbers (10,000) and up to a high Mach number(0.8). The main problem with this range was the ability to 'predict' the stall behaviour which is a whole subject on its own (J.Schroeder, 2005). Also it was found that effects like the lift hysteresis as shown in figure D.1 are well documented (Bohorquez & Pines, 2003) ,but it is difficult to be found in databases if found at all.

(a) Angle of attack (b) Reynolds number
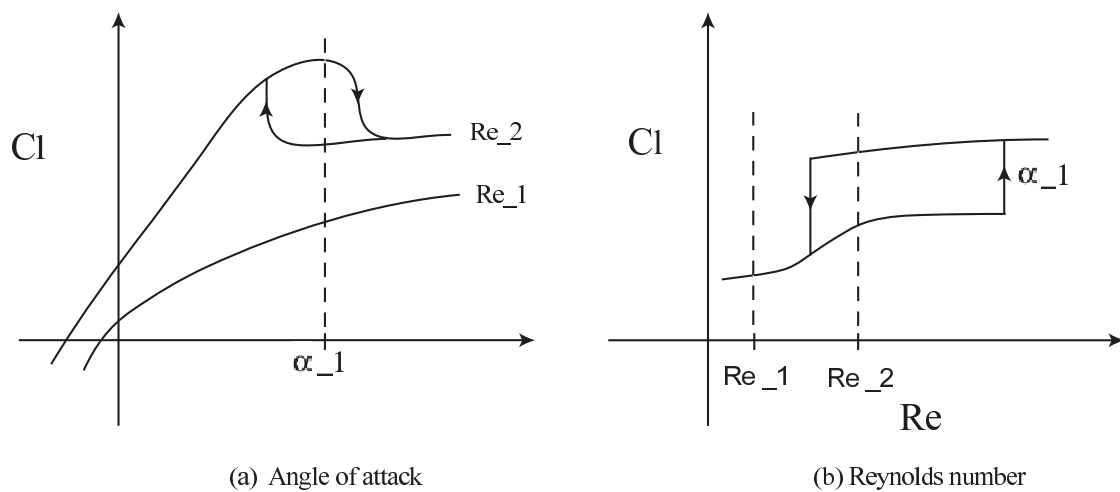
Figure D.1: Hysteresis effect

This meant that setting up the look-up table for the complete range of values described above was very harder. The final database set-up consist of three set ups. The first is a NACA0012 windtunnel database for the which the angle of attack range was 0 to 180° and test were performed at different Reynolds numbers.At Reynolds numbers lower they would be rounded up and at Reynolds numbers larger they would be rounded down. The velocity(Mach number) was neglected in the construction of the the look-up table as no velocity data was available. The pressure coefficient from the test could be corrected using the compressibility correction as stated by:

1. Prandtl-Glauert

2. Karman-Tsien

3. Laitone

The second option is to use the data calculated by codes like x-foil/XFLR with its limits. These are the angle of attack and Mach number combination the code is able to solve.

The last set used is the extended data from either the windtunnel tests or the codes using one of the extension methods.

D.2   Parts Testing

The flapping motion was modelled using two different methods. The first is to model it using a analytical method developed by M. D. Pavel as can be seen in (Pavel, 2001). This is further explained in section 2.2.1. The second method is to solve the ODE equation of motion obtained from the forces calculated on the blades. This process is explained in section 2.2.1.

Again the input values are the saved values from the reference model. The values to be compared are the three most important Fourier coefficients for the flapping motion. These are the coning angle ($a0$), the longitudinal tilt ($a1$) and the lateral tilt ($b1$). The non-dimensional inflow velocity (Λ_0) is also checked to see if the input values are correctly read in.

D.2.1   Flapping Motion

Analytical

The analytical solution for the flapping equation is based on a few combined parameters. These are shown in D.6.

$$\gamma \tag{D.1}$$

$$\mu, \mu_x, \mu_y and \mu_z, \Lambda_0 \tag{D.2}$$

$$\Omega \tag{D.3}$$

$$\theta_0, \theta_1 c, \theta_1 s, \theta_{tw} \tag{D.4}$$

$$p, r, q \tag{D.5}$$

$$\nu_b \tag{D.6}$$

When these parameters are exactly the same the result should also be the same.

The Hovering case with a velocity of 0 m/s this error is zero with respect to version V2 as can be seen in D.2a. This is exactly the same code as the original but modular. For some reason the solution as presented in the reference case is different from the copied version to be used as reference.

If the forward velocity is increased to 10 m/s the error observed for versions V7 and V8 increase as can be observed in figure D.2b. This is probably the case because of the tip losses which are present in these versions. The effect is that the induced velocity at the tips is much smaller than the *ideal* case.

Increasing the forward velocity further leads to the effect that the values are below the reference for V5 and V6 and above the value for V7 and V8. This can be observed in figure D.2c and D.2d.
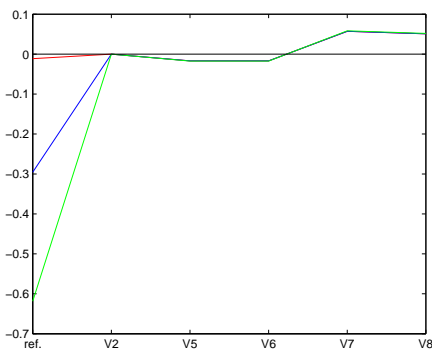
At a velocity of 70 m/s there is a transition as the error for versions V7 and V8 decrease which can be observed comparing figures D.2e and D.2d. The decrease is caused by the angle which can be explained by the induced velocity v_i.
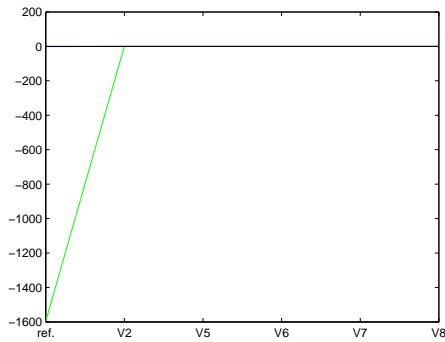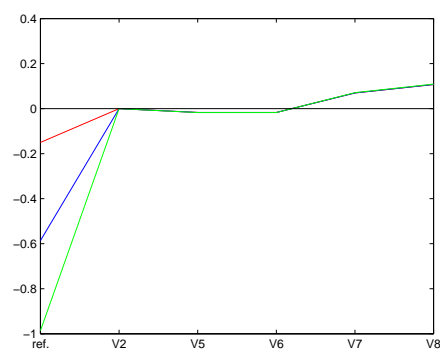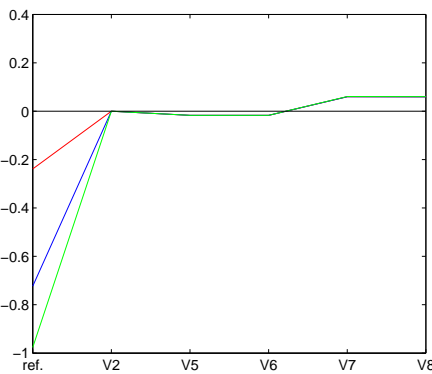
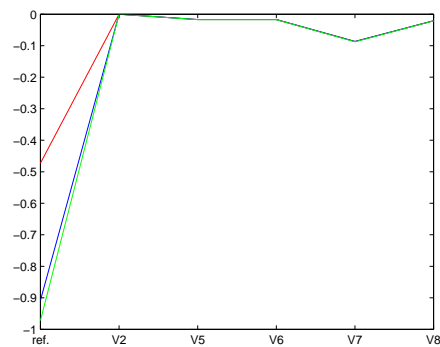(a) Errors at $V = 0m/s$
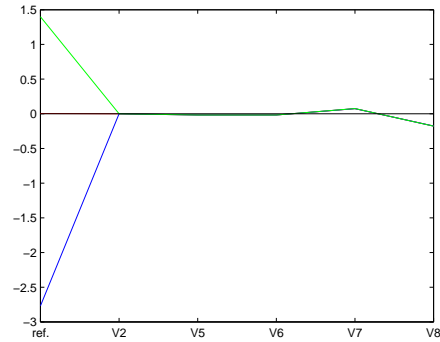
(b) Errors at $V = 10m/s$

(c) Errors at $V = 20m/s$

(d) Errors at $V = 60m/s$

(e) Errors at $V = 70m/s$

(f) Errors at $V = 100m/s$

Figure D.2: Upper Flapping Comparison

Increasing the velocity beyond this point leads to the error in the flapping coefficients to be negative for all new versions as shown in figure D.2f. Although the error is with in 10% for all version except the reference.

As can be seen in table D.1 the induced velocity is exactly the same, thus expecting to get the same result for the rest of the calculation this is however not the case. Initially the

Velocity	$a0_{ref}$	$a0$	$a1_{ref}$	$a1$	$b1_{ref}$	$b1$	$\Lambda_{0,ref}$	Λ_0
0	0.0012	0.0012	$9.0058e^{-13}$	$-1.56e^{-9}$	$1.4412e^{-9}$	$2.39e^{-10}$	0.0396	$3.96e^{-2}$
10	0.0015	0.0015	$1.1920e^{-4}$	$-3.48e^{-5}$	$3.1769e^{-4}$	$1.60e^{-4}$	0.0359	$3.59e^{-2}$
20	0.0017	0.0017	$3.0507e^{-4}$	$4.17e^{-4}$	$7.7353e^{-5}$	$1.84e^{-4}$	0.0249	$2.49e^{-2}$
30	0.0018	0.0019	$5.1741e^{-4}$	$8.13e^{-4}$	$-1.1834e^{-5}$	$2.55e^{-4}$	0.0191	$1.91e^{-2}$
40	0.0019	0.0020	$6.6217e^{-4}$	$1.10e^{-3}$	$-4.4773e^{-6}$	$3.84e^{-4}$	0.0150	$1.50e^{-2}$
50	0.0019	0.0021	$7.3942e^{-4}$	$1.40e^{-3}$	$4.0156e^{-6}$	$5.64e^{-4}$	0.0121	$1.21e^{-2}$
60	0.0018	0.0022	$7.6069e^{-4}$	$1.70e^{-3}$	$1.2814e^{-5}$	$8.21e^{-4}$	0.0100	$1.00e^{-2}$
70	0.0018	0.0023	$6.4235e^{-4}$	$2.10e^{-3}$	$3.3608e^{-5}$	$1.20e^{-3}$	0.0084	$8.40e^{-3}$
80	0.0018	0.0025	$6.5962e^{-4}$	$2.50e^{-3}$	$3.6590e^{-5}$	$1.50e^{-3}$	0.0074	$7.40e^{-3}$
90	0.0017	0.0025	$1.3906e^{-4}$	$2.60e^{-3}$	$5.1330e^{-4}$	$2.30e^{-3}$	0.0063	$6.30e^{-3}$
100	0.0017	0.0029	$3.8267e^{-4}$	$3.40e^{-3}$	$7.6004e^{-5}$	$2.20e^{-3}$	0.0059	$5.90e^{-3}$

Table D.1: Analytic Flapping Motion Values for Upper Rotor

values for the flapping coefficient are about the same as the reference, then from about 30 m/s the values provided by the new model start to deviate. For $a0$ it looks like the original model hits a asymptote while the new model continues to grow ending at larger values. For the other two flapping coefficients the new model also has much larger values, the values them selves being small.

When the data used to check the model is manually entered into the reference model the results correspond with those in the new model. Apparently the data needed is changed or incomplete compared to the reference model. An explanation for this is not yet found because of the data being copied from the reference model. The back check should result in the results being equal for the same values loaded.

(a) Values for $a0$　　　　　　(b) Values for $a1$　　　　　　(c) Values for $b1$
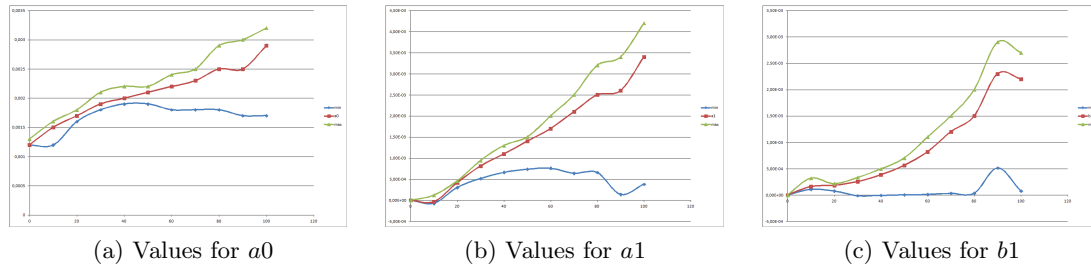
Figure D.3: Minimum, Mean and Maximum values from the Calculations

The data obtained during these calculations is processed to obtain a figure showing the minimum, mean and maximum values obtained during calculation. This is sorted by forward speed and shown in figure D.3

What can be observed is that as the velocity increases the values calculated for the flapping motion deviate more and more. This can be observed in all three coefficients and is shown in figure D.3.

Other observations are that the shape of the curve of the coning angle $a0$ looks OK increasing with forward speed and running up to a certain value.

The longitudinal tilt $a1$ is increasing still which also is logical since the forward velocity requires the Thrust produced by the rotor to tilt forward. This also means that the thrust

should increase to keep altitude.

The lateral tilt $b1$ leaves some mystery since at trimmed flight it should remain around 0. This is however not the case as can be observed in figure D.3c. This was the reason to look at the input variables used to obtain the results.

Lower Rotor

Also the flapping motion of the lower rotor is compared. This is done in the same way as for the upper rotor. For the lower rotor however there is an extra input which is the attenuation matrix which describes the shape and amount of effect of the upper rotors wake.

The hovering case is similar to the results from the upper rotor. This can be observed in figure D.4a.

Increasing the forward velocity results in the large deviation of $a0$(red) and $a1$(blue) for V6. The effects are also seen in V7 and V8, but here they are smaller. There is no real explanation to why this is the case, but it is reasonable that it is cause by the wake projection. This is because the wake introduces non-uniform inflow on the rotor, thus it is feasible that the flapping motion might react to this. These effect continue and can be observed until a forward velocity of 20 m/s as can be seen in figure D.4b.
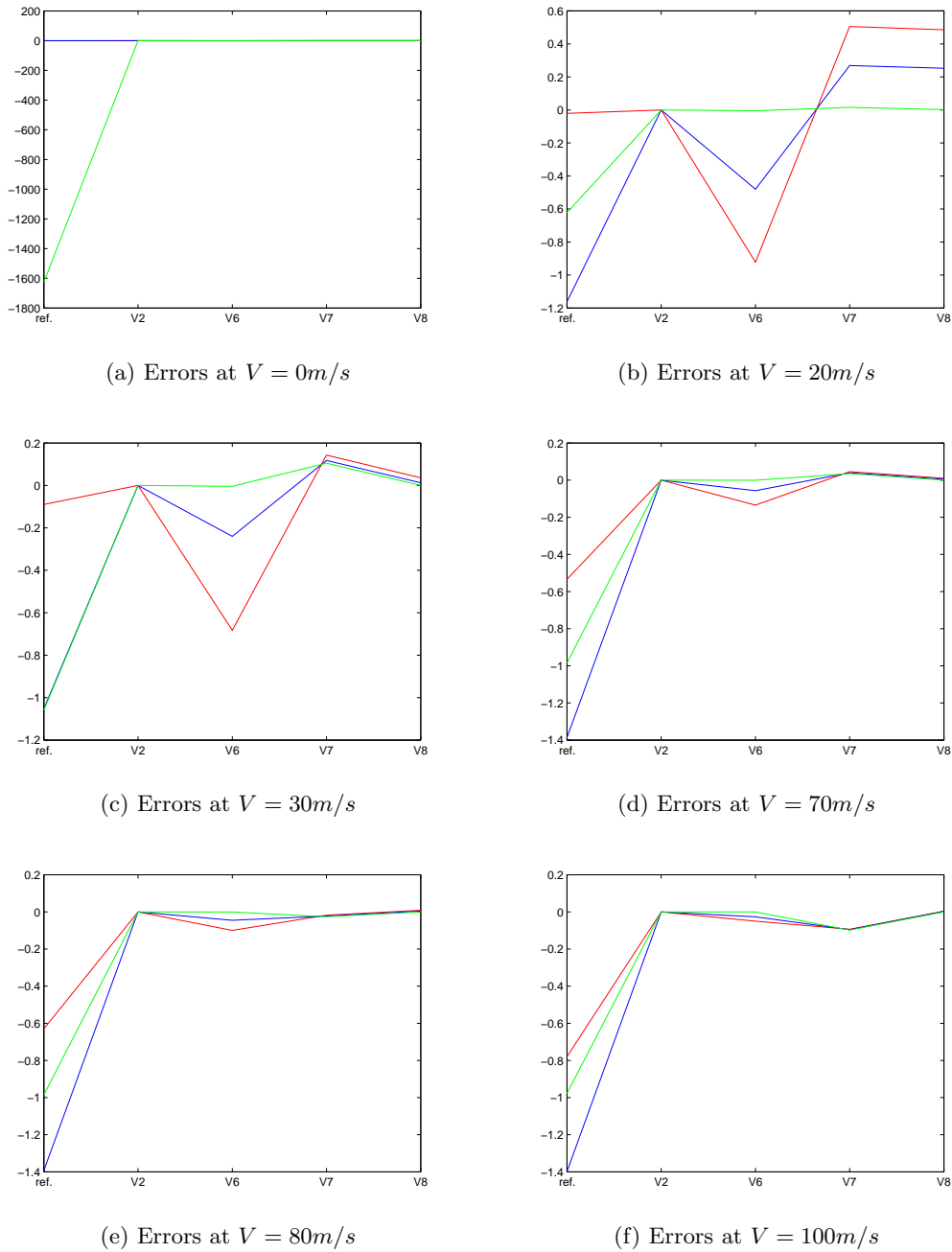
Increasing the velocity further results in an decreasing magnitude of the error for all version. In figures D.4c and D.4d the decreasing size of the error can be observed. This continues until the end at 100 m/s.

An interesting observation is that between the velocities 70 and 90 m/s the error changes sign. The observed error plot changes its shape as can be observed going from positive in figure D.4d to neutral in D.4e and then to negative in figure D.4f. The error still get smaller than described earlier.

Velocity	$a0_{ref}$	$a0$	$a1_{ref}$	$a1$	$b1_{ref}$	$b1$	$\Lambda_{0,ref}$	Λ_0
0	$9.7048^e{-}4$	0.0011	$9.0058e^{-13}$	$-1.1116e^{-9}$	$1.4412e^{-9}$	$2.8755e^{-10}$	0.0489	0.035
10	$6.9362e^{-4}$	$6.4396e^{-4}$	$1.6078e^{-5}$	$-1.2909e^{-4}$	$3.1669e^{-4}$	$1.6400e^{-4}$	0.0338	0.027
20	$3.9954e^{-4}$	$4.1189e^{-4}$	$-1.7392e^{-5}$	$8.3692e^{-5}$	$7.4301e^{-5}$	$1.7244e^{-4}$	0.0182	0.013
30	$4.5805e^{-4}$	$4.4345e^{-4}$	$-1.5482e^{-5}$	$2.2787e^{-4}$	$-1.6822e^{-5}$	$2.3037e^{-4}$	0.0104	0.009
40	$4.1384e^{-4}$	$4.5734e^{-4}$	$-8.1882e^{-5}$	$2.8960e^{-4}$	$-1.1532e^{-5}$	$3.4888e^{-4}$	0.0073	0.006
50	$4.1041e^{-4}$	$5.3182e^{-4}$	$-1.7106e^{-4}$	$4.0067e^{-4}$	$-4.7116e^{-6}$	$5.2642e^{-4}$	0.0058	0.005
60	$4.2155e^{-4}$	$6.5254e^{-4}$	$-2.8250e^{-4}$	$5.6546e^{-4}$	$2.7368e^{-6}$	$7.5476e^{-4}$	0.0050	0.004
70	$4.7170e^{-4}$	$8.8839e^{-4}$	$-4.6052e^{-4}$	$8.6150e^{-4}$	$2.2884e^{-5}$	0.0011	0.0047	0.004
80	$4.4130e^{-4}$	0.0010	$-5.9675e^{-4}$	0.0011	$2.4365e^{-5}$	0.0014	0.0040	0.003
90	$5.5976e^{-4}$	0.0015	-0.0011	0.0014	$5.0152e^{-4}$	0.0023	0.0042	0.004
100	$4.1606e^{-4}$	0.0015	-0.0011	0.0019	$6.3087e^{-5}$	0.0021	0.0034	0.003

Table D.2: Analytic Flapping Motion Values for Lower Rotor

One thing that is seen in table D.2 is that the coning angle in the reference case remains almost constant while in the extended version the value steadily increases with one exception the hovering case. The cause is logically to be the wake going outside the influence area. This doesn't explain the same effect for the upper rotor.

(a) Errors at $V = 0m/s$

(b) Errors at $V = 20m/s$

(c) Errors at $V = 30m/s$

(d) Errors at $V = 70m/s$

(e) Errors at $V = 80m/s$

(f) Errors at $V = 100m/s$

Figure D.4: Lower Flapping Comparison

Also it has to be noted that the longitudinal tilt becomes negative in the reference case while in the new version the tilt has exactly the opposite sign and keeps growing.

The reference values of the non-dimensional inflow are not the same as can be observed in table D.2. The difference might be due to the different inflow, using the complete attenuation matrix instead of an idealized wake with four coefficients. The new values are initially higher than the reference value but when the forward velocity is increase the difference becomes smaller and smaller and finally the inflow in the new version is smaller

than the reference. Herein lies the change in the error as seen in figure D.4, the flapping value are following the trend shown by the inflow.

The results as are presented here were back checked by doing the checking in the opposite direction. So instead of using the reference values in the new model, the values from the new model were used in the reference model. The results were that using the values from the new model in the reference code yielded the same results as the new model. Somehow the input data before calculation is changed(in either reference or new model) or some system variables in the reference model(global) might effect the results. If the data set as used by the controls is re-entered into the reference model the result for the flapping coefficients $a0$, $a1$ and $b1$ are exactly the same as shown in appendix B.

Differential equation(of Motion)

The differential equation describing the flapping motion was another method to solve the flapping motion. The calculation took a significant amount of time longer than the analytical alternative. While the results were not even close to the reference values calculated by either the reference model or the analytical alternatives.

For the differential equations there are no error plots. This due to the long time it took to calculate the results and the number of required calculations to obtain these plots.

Velocity Input	$a0_{ref}$	$a0$	$a1_{ref}$	$a1$	$b1_{ref}$	$b1$
0	0.0012	0.0386	$9.0058e-13$	$5.86e-4$	$1.4412e-9$	$1.18e-5$
10	0.0015	0.0456	$1.1920e-4$	0.0102	$3.1769e-4$	0.0045
20	0.0017	0.0634	$3.0507e-4$	0.0178	$7.7353e-5$	-0.0171
30	0.0018	0.0727	$5.1741e-4$	0.0258	$-1.1834e-5$	-0.0318
40	0.0019	0.0763	$6.6217e-4$	0.0346	$-4.4773e-6$	-0.041
50	0.0019	0.0783	$7.3942e-4$	0.0439	$4.0156e-6$	-0.051
60	0.0018	0.0785	$7.6069e-4$	0.0518	$1.2814e-5$	-0.0586
70	0.0018	0.0778	$6.4235e-4$	0.0616	$3.3608e-5$	-0.67
80	0.0018	0.0793	$6.5962e-4$	0.066	$3.6590e-5$	-0.076
90	0.0017	0.0744	$1.3906e-4$	0.0819	$5.1330e-4$	-0.0754
100	0.0017	0.0803	$3.8267e-4$	0.078	$7.6004e-5$	-0.0924

Table D.3: Equation of Motion Flapping Motion Values for Upper Rotor

In table D.3 the values calculated by solving the equation of motion for the blade can be observed, the results are giving completely different values.

For the coning angle the difference is large (0.0012 - 0.0386) and becomes even larger (0.0017 - 0.0803). Despite this large difference the trend of the solved equations of motion is the same as the one calculated by the analytical function in the updated model, which uses the same calculation method for the forces.

For the longitudinal tilt the behaviour is also the same as can be observed by comparing figures D.3 and D.5. Again the absolute value is completely different.

For the lateral tilt shows a negative value in the solved equation of motion while the analytical method comes up with positive numbers. The two 'wiggles' that can be observed

at $\pm 10\ m/s$ and $\pm 80\ m/s$ are also observed in both methods. These wiggles are probably the places were the majority of the rotor changes it angle of attack/tangential velocity, which causes the forces that are looked up to be different. Similar effects are seen in the reference model (Campfens, 2008).
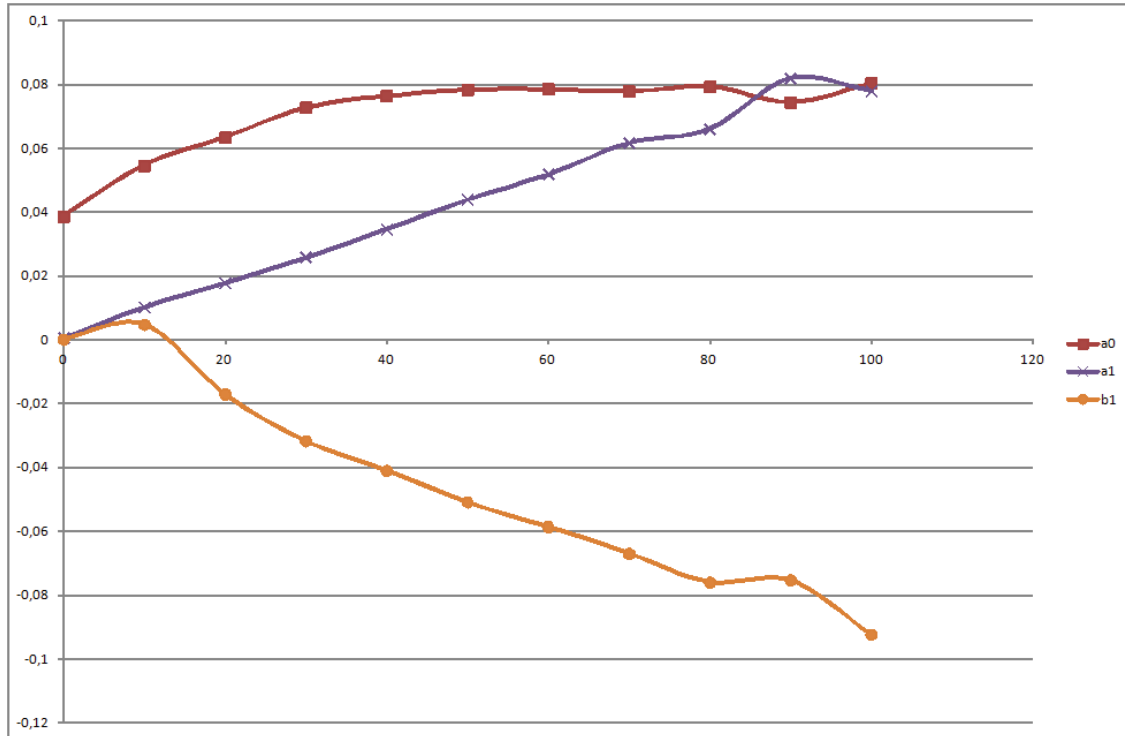

Figure D.5: Flapping coefficients vs Velocity

The flapping angle and there change when increasing the forward velocity is shown in figure D.5. It can be observed that the shape of the coning angle($a0$) corresponds with those of the reference model, albeit larger. This effect is flatting out.

The forward tilts($a1$) change is also reasonable since increasing the forward velocity the rotor will tilt forward. which is a logical response to the movement as is also explained in (van Holten & Melkert, 2002).

The lateral tilt($b1$) is difficult to explain, but the most obvious would be the asymmetric lift generation due to the rotation of the upper-rotor. This effect should shown up on a force plot, however the effect is normally cancelled out by the flapping motion.

D.2.2   Wake & Attenuation Calculation

The Wake and Attenuation calculations are done in two separate modules. One is the calculation of the wake contraction ratio using the equations as presented by Landgrebe in (Landgrebe, 1969), (Landgrebe, 1971), (Landgrebe, 1972) and (Landgrebe, Taylor, Egolf, & Bennett, 1982) and described in section 2.3.1.

The next is the calculation of the attenuation matrix modified to incorporate the contraction ratio calculated in section 2.3.2 using the equations as presented by Castles in

(Castles & Leeuw, 1953a) and (Castles & Durham, 1956).

The main input is again the reference values as are used in the reference model. With the exception of the attenuation matrix, for which the corresponding code to calculate this matrix was copied to obtain the whole matrix instead of the four coefficients used by the reference model. This was done to improve the comparability of the results of the attenuation matrix.

Wake

As the wake calculations are done using analytical function. Using the same input values should result in the same output values. The results for the wake calculations show that the error is exactly zero for all forward velocities as was expected.

(a) Errors at $V = 0m/s$ (b) Errors at $V = 100m/s$
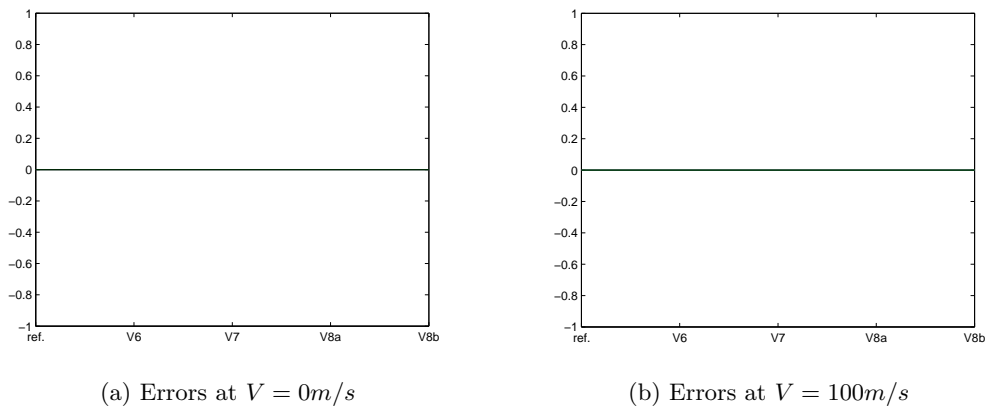
Figure D.6: Wake Comparison

As can be observed in figure D.6 there is no real difference, error is zero. This is shown for the hovering case in D.6a and for a forward velocity of $100m/s$ in D.6b. The main reason is that the method to calculate the wake contraction is analytical and this means that the error should be zero as there are no real sources of difference in the calculation method as is shown in section 2.3.1.

The first variable coefficient,$k1$, is based on the rotor solidity σ, the twist angle θ_{tw} both are geometric inputs) and the thrust coefficient of the rotor from which the wake contracts C_t. The value increasing until at 50 m/s, then the value wiggles around an almost constant. The reason for this is most likely the changes in the thrust coefficient used as input, since the rotor geometry to calculate σ is constant.

The coefficient $k2$ is calculated using the twist angle and the thrust coefficient. Because the twist angle was set to a fixed value the only variable input is again the thrust coefficient.

As seen with coefficient $k2$ increasing values until 50 m/s then the value wiggles around and comes slightly down just as $k1$.

The contraction ratio is calculated from constant coefficients an the thrust coefficient as a function of the vertical position from the respective rotor. This means that the

Velocity Input	$k1$	$k2$	wcc
0	0.0136	0.0558	0.8502
10	0.0178	0.0639	0.8500
20	0.0199	0.0676	0.8496
30	0.0224	0.0716	0.8489
40	0.0232	0.0729	0.8487
50	0.0233	0.0731	0.8486
60	0.0232	0.0729	0.8487
70	0.0226	0.0719	0.8489
80	0.0229	0.0723	0.8488
90	0.0220	0.0709	0.8490
100	0.0227	0.0722	0.8488

Table D.4: Wake Output Values

contraction ratio initially comes down, which is logical since the thrust coefficient is also decreasing due to the increased lift generated by the forward velocity.This is then also the reason why it is expected that at even higher velocities the wake contraction would increase again, this is however not the case and the value remains around 0.8489. The most likely reason for this is the wake calculations switch between the first rotation and the subsequent. Or the thrust coefficient remaining constant. Thus leaving the results the way they can be observed in table D.4.

The initial goal was to change the wake shape for the low Reynoldsnumber calculations the reference for this was found in a paper (Hein & Chopra, 2007), but in essence the variation would lie in the adaptation of the coefficients to match the shape as shown in figure D.7. Due to the trim calculation difficulties and time constrains this was never executed.

Attenuation Matrix

The results show that the errors are small. This despite the matrix being size(21x21). The only significant difference is in V7 and V8 of the new model and this can be explained by the difference in calculation of the wake contraction ratio. This is further explained in subsection 2.3.1 the wake contraction and the tip loss function as shown in subsection 2.2.3.

Despite this the error is still about 18%.

Knowing the contraction ratio, based on the thrust coefficient, and the forward velocity. The skew angle can be calculated for the positions were the wake boundary coincides with rotor boundaries/positions. These are the back of the rotor wake and the back of the rotor at $38.44°$. The front of the wake and the centre of the rotor at $77.46°$. And the front of the wake and the back of the rotor at $84.17°$. These transitions are calculated using the method from the reference model and the method implemented in the new model, both based on the functions as described by Castles (Castles & Leeuw, 1953b). These calculation are then plotted together with the *method* the attenuation coefficients are used in the reference model.
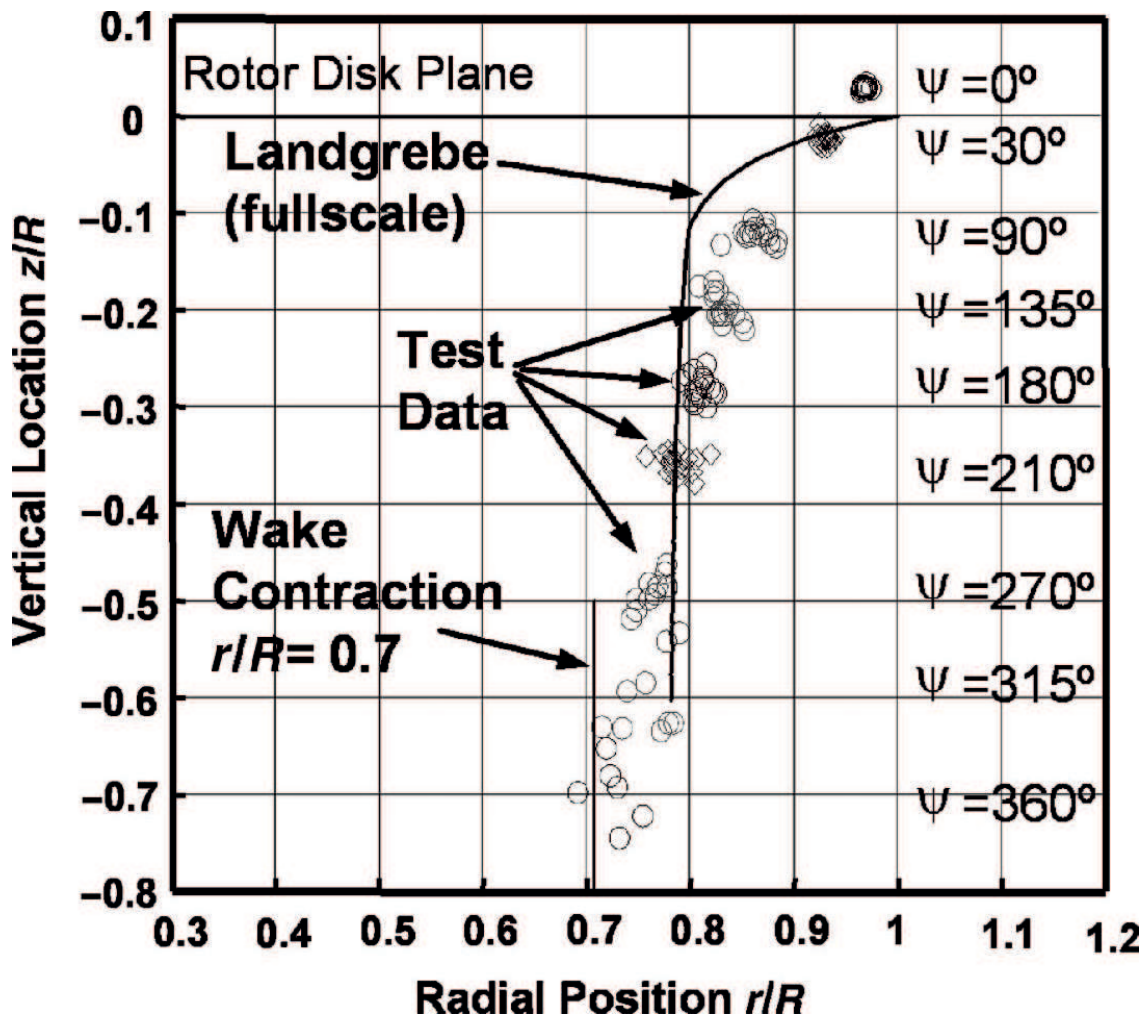
Figure D.7: Low Reynoldsnumber Wake shape

The difference that can be observed in the *contraction* ratio are clear, this while the value of the contraction ratio is exactly the same. This difference is due to the different ways the attenuation with a wake contraction was implemented.

The observation can be made that the *position* were the back of the wake should correspond with the back of the rotordisk, the calculated reference shows that this is not the case will the new method does. The absolute values are shown to correspond with the original calculations by Castles shown in figure D.10.

An other interesting thing to observer is that the reference assumes that when the wake leaves the rotordisk the influence is 'gone', in the calculation methods from Castles this is not the case and the influence on the back rim of the rotordisk is 'large' 2, the standard accelerated induced velocity.

Comparing the result for hover to the results from figure D.10a the attenuation coefficient look to correspond. The high value at the back of the rotor are also present in the calculations by Castles shown in D.10b.
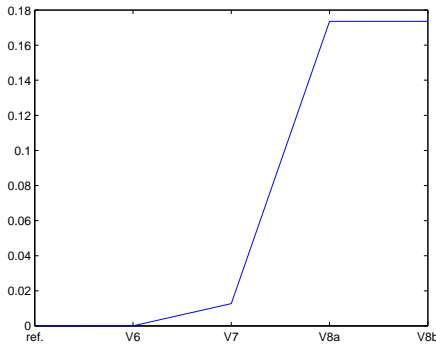
(a) Errors at $V = 0m/s$
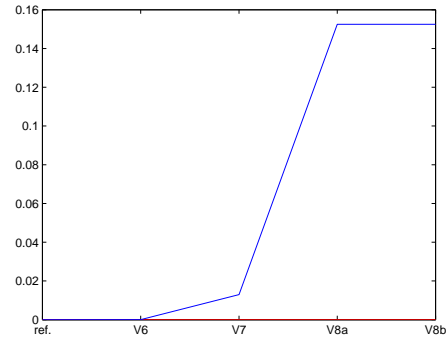
(b) Errors at $V = 30m/s$
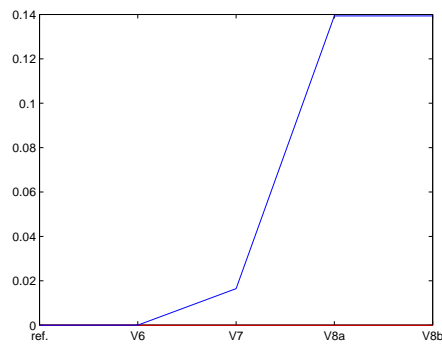
(c) Errors at $V = 70m/s$
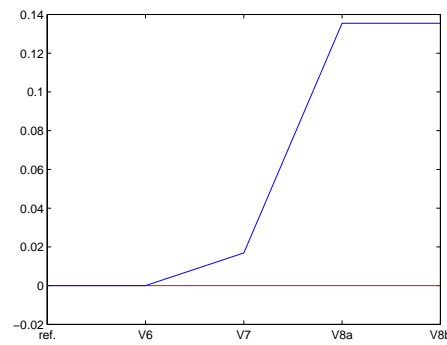
(d) Errors at $V = 100m/s$

Figure D.8: Attenuation Comparison

D.2.3   Rotor Forces

The forces on the rotor are compared using the calculated variables to be called by the equations of motion. The thrust coefficients (C_t) is compared because it is important in the inflow determination. It is used to solve the trim calculations. Also the thrust T, lateral S and longitudinal H forces are compared. Also derived forces can be compared, this includes the torque Q and X,Y and Z forces. These forces in combination with the derived moments L, M, N can be used to spot the cause of errors.

Upper Rotor

The rotordisk calculations are again based on the values from the reference. This leads to values of about 98 % of the original value. Given the fact that the analytical calculations are based on averaged values and the numerical method calculates with a variation based on radial station and azimuth angle. This is a good result.

Starting with the hovering case the largest error is found in *V6* due to the absence of any refinement in the rotor forces modelling. Then when the forward velocity is increased the largest error occurs in *V2* this is probably due to the same data input error as seen in other parts. The strange thing is that V2 is an exact copy of the reference model, only

(a) 38.44   (b) 77.46   (c) 84.17

(d) 38.44   (e) 77.46   (f) 84.17

(g) 38.44   (h) 77.46   (i) 84.17
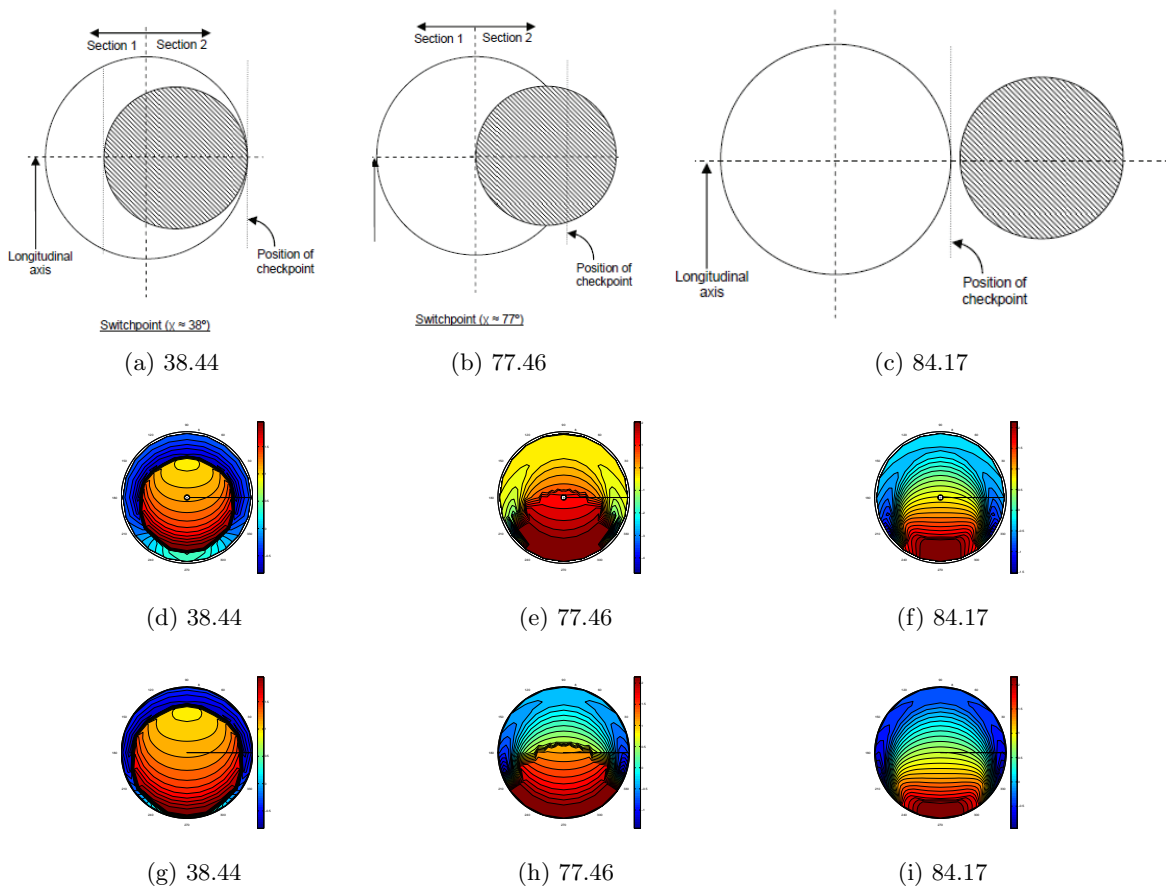
Figure D.9: The transitions of the Upper rotor wake on the lower rotor

set-up as a separate module. Giving the data used by the new module into the reference module gives exactly the same values as V2. The error in the thrust coefficient decreases with increasing forward velocity until around 30 to 40 m/s then the error increases. This is only the case for the blade element method, the thrust coefficient calculated using the momentum method has only an error in V7 and V8, and this can be explained by the decrease in induced velocity due to the implementation of the root and tip loss methods. The thrust using the BEM increases with increasing forward speed, which is logical since the thrust vector tilts. This increasing thrust is however larger in the method using the look-up tables than it is in the analytical method, this can also be observed in figure D.11 were the values are plotted for the various velocities as are shown in table D.5. The main cause lies in the method using the look-up table.

1. The tables are rough, refinement might solve the difference

2. Also no degradation is implemented, the degradation to the rotor thrust has to be velocity depended. This indicates toward compressibility degradation.

The main innovation of the model is the use of the look-up tables which can make it difficult to have an successful implementation.
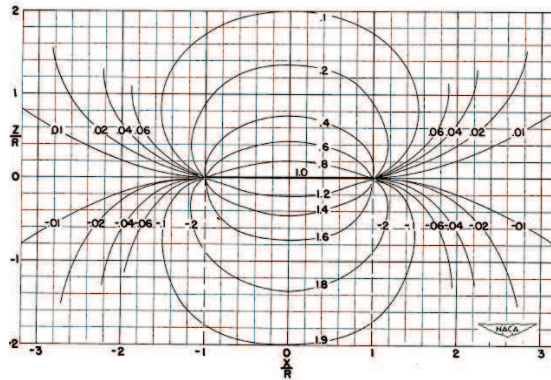
(a) Attenuation Coefficients in Hover
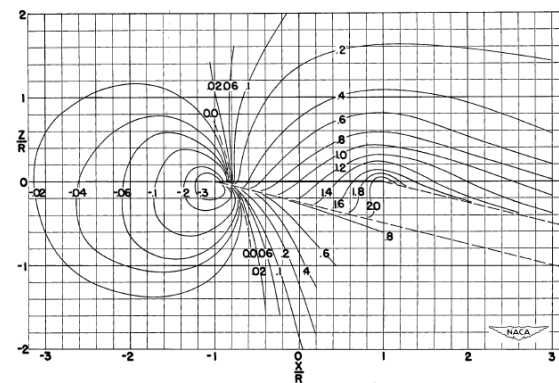
(b) Attenuation Coefficients at a skew angel
of 75.97 degrees

Figure D.10: Attenuation coefficient on the longitudinal centreline according to Castles

| Velocity Input	C_{t-gl_ref}	C_{t-gl}	C_{t-be}	C_{t-be_ref}
0	0.0136	0.0558	0.0558	0.8502
10	0.0178	0.0639	0.0558	0.8500
20	0.0199	0.0676	0.0558	0.8496
30	0.0224	0.0716	0.0558	0.8489
40	0.0232	0.0729	0.0558	0.8487
50	0.0233	0.0731	0.0558	0.8486
60	0.0232	0.0729	0.0558	0.8487
70	0.0226	0.0719	0.0558	0.8489
80	0.0229	0.0723	0.0558	0.8488
90	0.0220	0.0709	0.0558	0.8490
100	0.0227	0.0722	0.0558	0.8488

Table D.5: Upper Rotor Thrust coefficients Output Values

Lower Rotor

The calculations of flapping motion and rotordisk(forces) are the same for both the upper
and the lower rotor. The results for the upper rotor are close to the reference values with
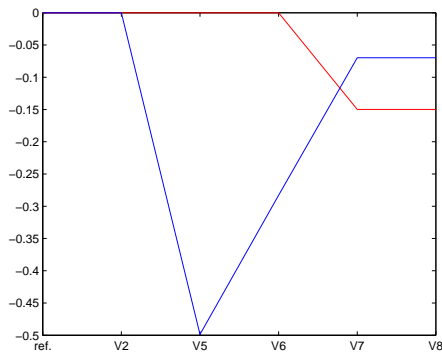
(a) Errors at $V = 0m/s$
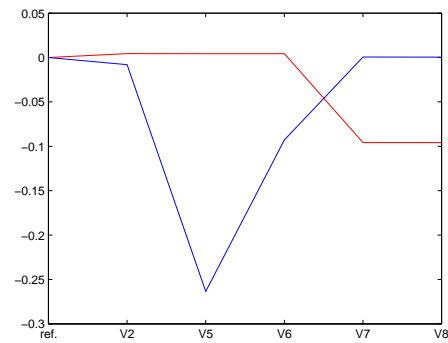
(b) Errors at $V = 10m/s$
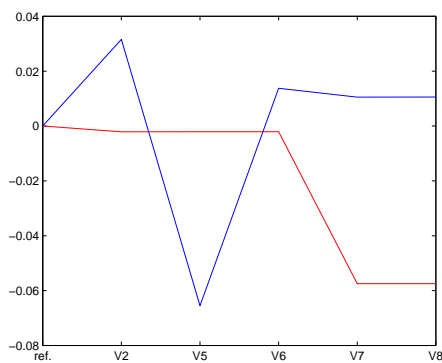
(c) Errors at $V = 30m/s$
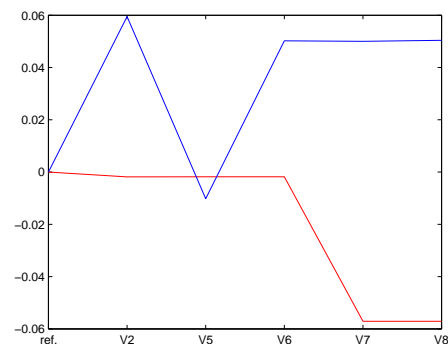
(d) Errors at $V = 40m/s$
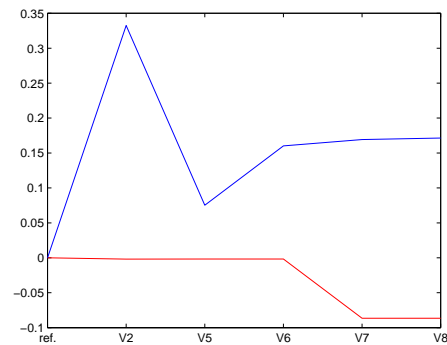
(e) Errors at $V = 70m/s$
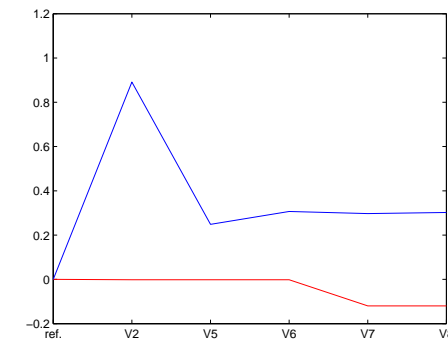
(f) Errors at $V = 100m/s$

Figure D.11: Upper Rotor thrust coefficient Comparison

little to no changes to the results from the numerical code. The results for the lower rotor based on the inflow influence from the upper rotor, deviate significant however. This can be partially explained by the simplification in the analytical method for the attenuation *matrix* compressed into four values. As is explained fully in the definition in (Campfens, 2008). Changing the numerical method to use only these four values leads to a more consistent result but still thrust values are only 70 % of the reference.
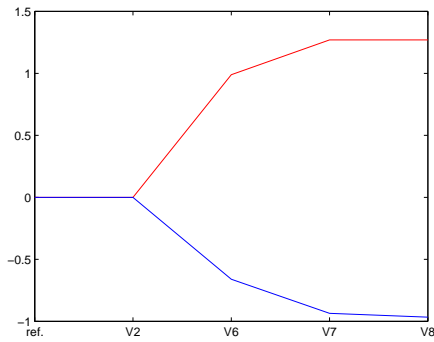
(a) Errors at $V = 0m/s$
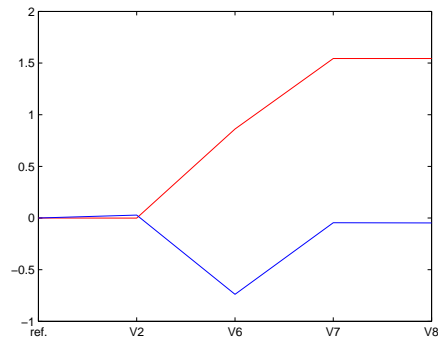
(b) Errors at $V = 20m/s$
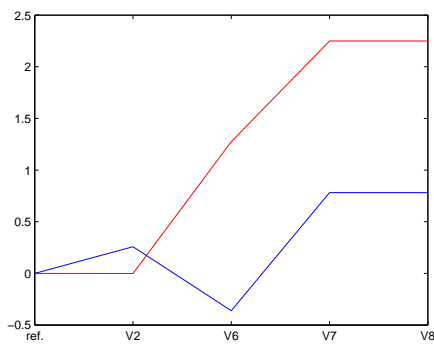
(c) Errors at $V = 40m/s$
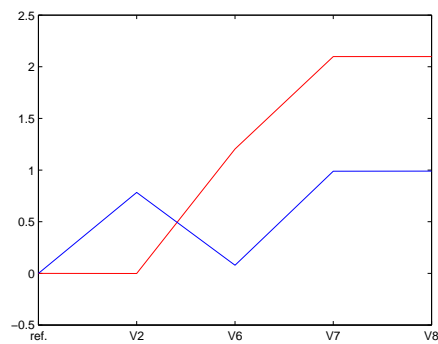
(d) Errors at $V = 60m/s$
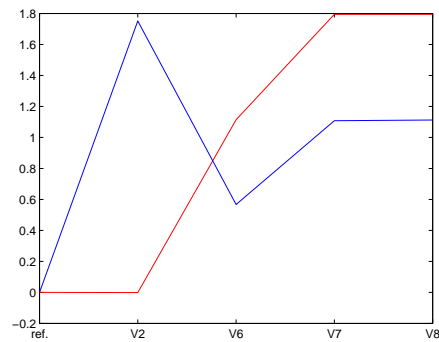
(e) Errors at $V = 80m/s$
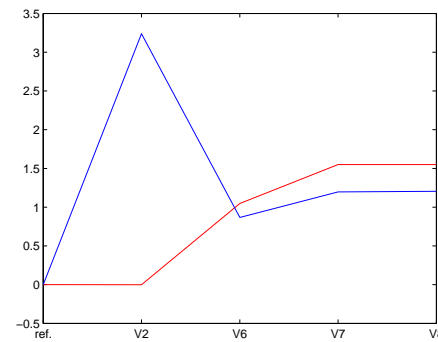
(f) Errors at $V = 100m/s$

Figure D.12: Lower Rotor thrust coefficient Comparison

In hover V2 is equal to the reference value. The thrust coefficient according to the momentum method(red) is higher, while the element method comes up with a lower value. The cause of both these phenomenon is most likely the attenuation coefficient leading to an increased down-flow resulting in a higher momentum thrust, due to mass-flow, this results in a lower angle of attack for the for the element method, thus resulting in a lower thrust value.

Both the thrust coefficients increase faster with increasing velocity than the reference

values. The attenuation effect on the momentum thrust can be observed for all new versions.

Looking at the reference functions there is an attenuation of only four coefficients present. These are for the forward and the rear side of the rotordisk with respect to the flow a coefficient in the wake and one outside of the wake.

The blade element method even deviates in version 2, which is exactly the same code as the reference. The input given to these modules results in different results. The input data for the test was manually used with the reference code, which resulted in the values calculated by version 2.

Another observation was that the rotor twist had a larger effect on the lower rotor results than for the upper rotor. Also the wake effect which was observed has a substantial effect on the forces on the lower rotor. This is most likely due to the large influence it has on the calculation methods, and thus the deviations observed. This was even the case in the updated calculation methods.

Velocity Input	$C_{t-gl_{ref}}$	C_{t-gl}	C_{t-be}	$C_{t-be_{ref}}$
0	0.0136	0.0558	0.0558	0.8502
10	0.0178	0.0639	0.0558	0.8500
20	0.0199	0.0676	0.0558	0.8496
30	0.0224	0.0716	0.0558	0.8489
40	0.0232	0.0729	0.0558	0.8487
50	0.0233	0.0731	0.0558	0.8486
60	0.0232	0.0729	0.0558	0.8487
70	0.0226	0.0719	0.0558	0.8489
80	0.0229	0.0723	0.0558	0.8488
90	0.0220	0.0709	0.0558	0.8490
100	0.0227	0.0722	0.0558	0.8488

Table D.6: Lower Rotor Thrust coefficients Output Values

D.2.4   Body Forces

The body forces, including the vertical and horizontal tail, are exactly the values as are calculated in the reference.

The errors plotted for two forward speeds, hover(0 m/s) and the maximum calculated forward speed (100 m/s). This done for the vertical tail surface as is shown in figure D.13, the fuselage shown in figure D.14 and the horizontal tail shown in figure D.15. As can be observed the error is zero. This was to be expected since the functions used are analytical and the input values are exactly the same since the influence of the rotorblades on the tail surfaces and fuselage were neglected. This means that the general deviation in the model does not come from the forces generated by the body and tail.
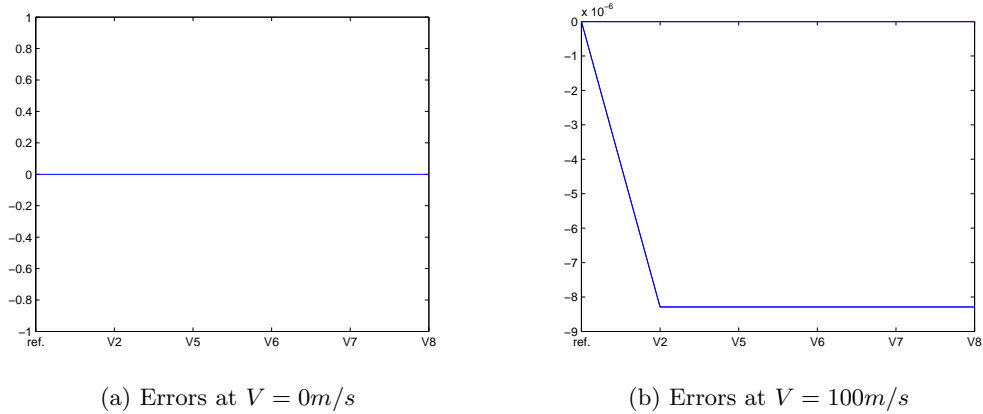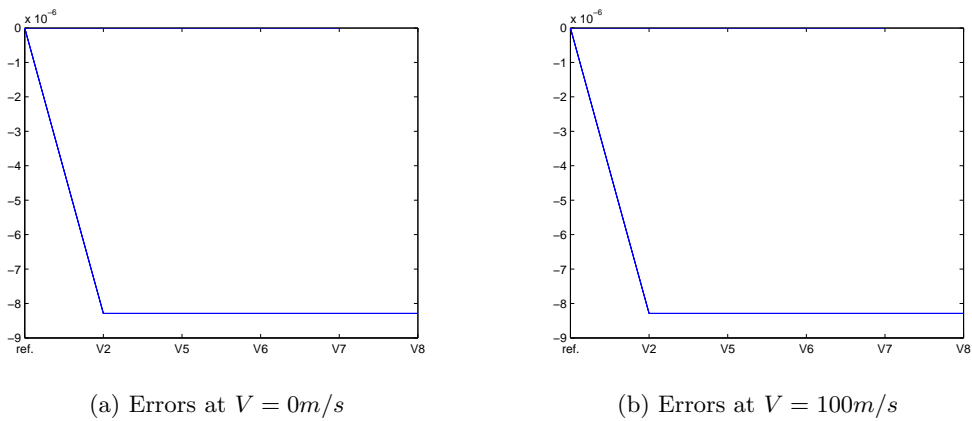
(a) Errors at $V = 0m/s$ (b) Errors at $V = 100m/s$

Figure D.13: Body Fin Comparison

(a) Errors at $V = 0m/s$ (b) Errors at $V = 100m/s$

Figure D.14: Body Fuselage Comparison

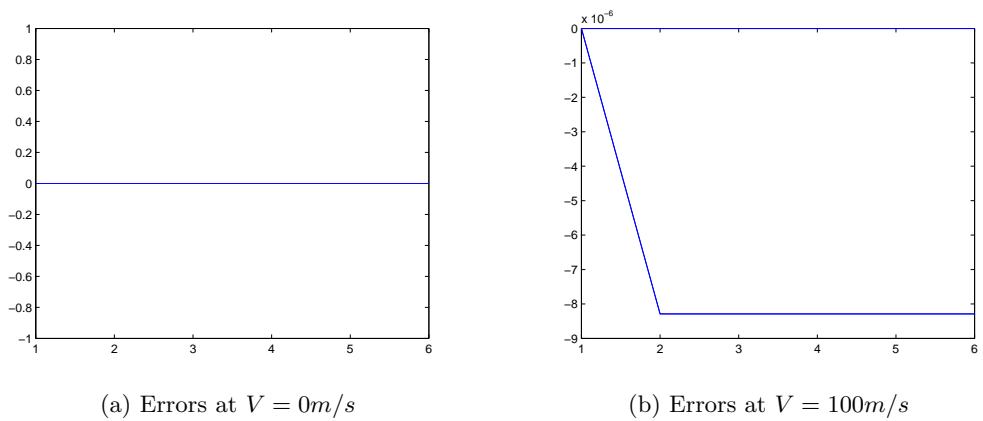(a) Errors at $V = 0m/s$ (b) Errors at $V = 100m/s$

Figure D.15: Body Horizontal Tail Comparison

D.2.5   Equations of Motion

The equations of motion are modelled using the same method as the reference model. The base is to use Newton $F = m \cdot a$ as is further elaborated in section C.3. This means that

given the same forces and moments the sum of these forces and moment should also be the same. The forces were chosen to be compared because the accelerations are calculated using the mass and the inertia, both of which are assumed to be constant with respect to the forces.

(a) Errors at $V = 0m/s$ (b) Errors at $V = 100m/s$
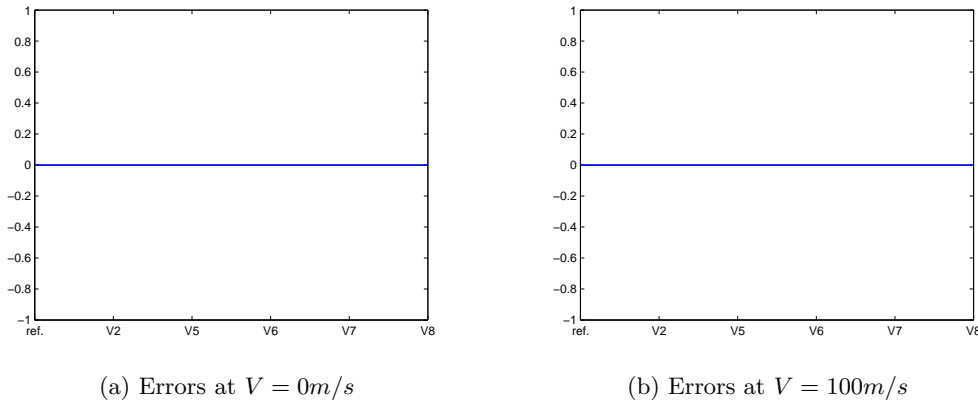
Figure D.16: Equation of Motion Forces Comparison

The error in the forces calculated in x, y and z direction are shown in figure D.16, as can be observed the error is zero. The shown figures are in hover and at maximum velocity the error in the forces is for both cases 0, this is also the case for all other evaluated velocities.

(a) Errors at $V = 0m/s$ (b) Errors at $V = 100m/s$
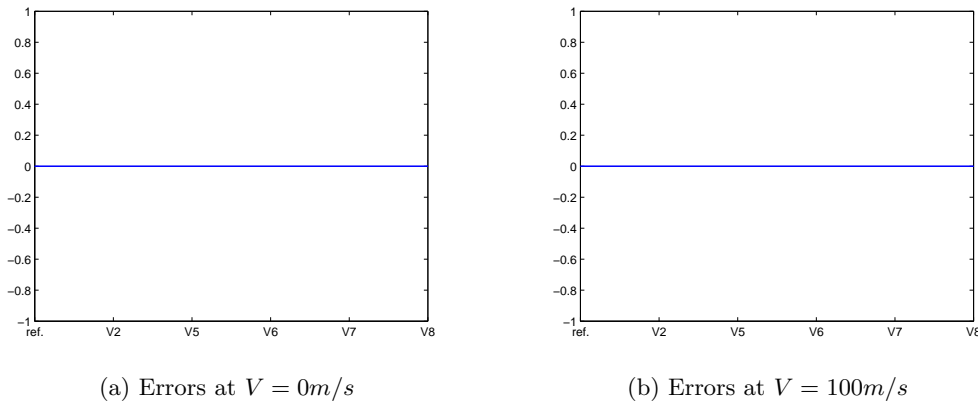
Figure D.17: Equation of Motion Moment Comparison

As is the case with the forces also the moments were calculated and the figure shown in D.17 are the result for the case hovering and the maximum velocity $100m/s$. Thus the errors in the main model are not coming from the implementation of the equations of motion.